UNIVERSITY OF CAPE TOWN
IYUNIVESITHI YASEKAPA • UNIVERSITEIT VAN KAAPSTAD


Department of Civil Engineering

Computational Continuum Mechanics Group

Polar Engineering Research Group


# Modelling of Brine Transport Mechanisms in Antarctic Sea Ice

A research project in partial fulfillment of the requirements for a Master of Sciences degree in the field of Civil Engineering

**Prepared for**: University of Cape Town


**Author:**
Ms. Andrea Cook

**Supervisor:**
A/Prof. Sebastian Skatulla

**Co. Supervisor:**
Dr. Keith Machutchon



*The financial assistance of the National Research Foundation (NRF) towards this research is hereby acknowledged. Opinions expressed and conclusions arrived at, are those of the author and are not necessarily to be attributed to the NRF.*


July 24, 2020

# Plagiarism Declaration

I know the meaning of plagiarism and declare that all the work in the document, save for that which is properly acknowledged, is my own. This thesis/dissertation has been submitted to the Turnitin module (or equivalent similarity and originality checking software) and I confirm that my supervisor has seen my report and any concerns revealed by such have been resolved with my supervisor.

| Name | Student number | Date | Signed |
|---|---|---|---|
| Andrea Cook | CKXAND008 | 24th July 2020 | Signed by candidate |

# Acknowledgements

Firstly, I would like to that my thesis supervisor, A/Prof. Sebastian Skatulla and Co. supervisor Dr Keith Machutchon for their guidance throughout this study. I would also like to thank them for always providing motivation to do my utmost best and never give up when running into challenges. I'd lastly like to thank them for their patience and enthusiasm when explaining concepts and providing assistance.

Secondly I'd like to thank my parents, Garth and Antoinette for funding and supporting me through all levels of my education and setting an exceptional example about what hard work really means. I'd also like to thanks my brother, Nathan for always encouraging me to do my best and for always being proud of me.

I'd also like to give thanks to all members of the Polar Engineering Research Group (PERG) for their ongoing support and guidance through this thesis.

The funding received from both the National Research Foundation (NRF) and the Postgraduate Civil Fund was greatly appreciated and allowed me to complete this research.

# Abstract

It is evident that the sea ice cycle, from its formation to its melt, is governed by a complex interaction of the ocean, atmosphere and surrounding continents. Once sea water begins to freeze, physical, biological and chemical processes have implications on the evolution of the sea ice morphology [38]. The distinguishing factor between fresh and sea water ice is brine inclusions that get trapped within the ice pores during freezing. Salt inclusions within frozen ice influence the salinity as well as the physical properties of the sea ice [23]. These brine inclusions form part of a dynamic process within the ice characterized by the movement of brine and phase transition which are the foundation of many of its physical properties [23]. Brine removal subsequently begins to occur due to vertical gravity drainage into the underlying ocean water. This study introduces the application of a biphasic model based on the Theory of Porous Media (TPM) which considers a solid phase for the pore structure of the ice matrix as well as a liquid phase for the brine inclusions, respectively. This work explores the use of the TPM framework towards advancing the description and study of the various desalination mechanisms that are significant in aiding the salt flux into the Southern Ocean. This will foster understanding of brine rejection and how it is linked to the porous microstructure of Antarctic sea ice.

# Table of Contents

# List of Figures

# List of Tables

# Chapter 1

# Introduction

## 1.1 Background to study

Sea ice benefits our planet in a number of ways. Sea ice cover reduces heat flux between the atmosphere and underlying ocean as it acts as a thermal insulator [29]. Along with this it provides a unique biological habitat, limits gas exchange between air and sea gas and aids in the planets surface albedo all while existing in an environment governed by varying temperature, salinity, nutrient gradients as well as radiation from the sun [2].

Scientific interest in the Antarctic region is on the rise as studies investigating the various factors from the ocean, land and atmosphere affecting the formation, growth and melt of Antarctic sea ice increase. Among the physical, biological and chemical processes that occur during the formation of sea ice is the entrapment of brine within the ice pores which is a distinguishing factor between sea ice and fresh water ice [38]. Phase transitions and brine movement within the ice form the foundation of the sea ices physical properties [23].

With the advent of the digital computer began the development of finite element methods as solutions to physical problems [3]. The process of modelling a physical problem entails the development of a mathematical model that is governed by differential equations and various assumptions relating to the physical problem. The principles of continuum mechanics are applied to aid as a source of insight into the behaviour of a problem thereby increasing the understanding of the problem at hand.

Frank *et al.*,[36] discusses the history of sea ice research and polar exploration with the current interest being in new oil/gas fields, wind, wave and tidal energy converters as well as climate change and climate modelling. The University of Cape Town's Polar Engineering Research Group (PERG) formed in 2016 to study both dynamics and thermodynamics within the Antarctic Marginal Ice Zone (MIZ). PERG is working towards gathering physical and mechanical properties of sea ice within the MIZ in order to verify existing computational models as well as create new ones to add to this body of knowledge. The study and modelling of brine transport mechanisms within Antarctic sea ice will is an important aspect in understanding the behaviour of the seasonal Antarctic sea ice.

The structure of sea ice varies due to dynamic changes in physical processes, chemical properties and biological movement [38]. Hunke *et al.*,[23] outlines that declining amounts of sea ice will decrease the earth's surface albedo resulting in heat absorption from the ocean's waters. Similarly, increasing amounts of sea ice could result the cooling of the underlying ocean. The melt and break-up of sea ice will cause it to drift and move pollutants trapped within

which in turn may have negative effects on surrounding habitats [23]. It is not yet clear what implications this change will have on the earth's climate, its ecosystems and mankind [38].

## 1.2 Problem identification

While the growth process of sea ice has been studied extensively and is fairly well understood as described in subsection 2.1.2, the movement of concentrated brine and sea water through the ice during its life is not completely understood [28]. Sampling and processing ice cores in situ is difficult as they exist in climates that are not easily accessible and inhospitable[19]. Griewank and Notz [19] mention the drawbacks of ice core sampling namely, brine loss, low temporal resolution, and the inability to repeat sampling as ice core extraction is destructive. It is known that the bulk salinity of sea ice is much less than that of sea water [24]. Measurement of brine movement in sea ice is lacking and the majority of the current knowledge about this results from salinity measurements taken from ice samples as well as studies of growing multiphase materials [19].

Sea ice forms the membrane between the ocean and the overlying atmosphere through which moisture, heat and momentum are transported [37]. It is strongly influenced by and influences climate [37, 38]. It is known that brine movement within sea ice influences mechanical, electromagnetic and biological transport properties which in turn effect the ecology and buoyancy forcing in the underlying oceans [28, 42]. Understanding the brine transport mechanisms in Antarctic sea ice will aid in better understanding variations in these properties. Salinity is a vital parameter in understanding the behaviour of sea ice and is thought to be highly variable due to the inhomogeneous distribution of brine but this is not easily quantifiable [15].

The evolution of bulk salinity needs to be understood as it governs salt flux into the ocean as well as the distribution of the ice's freshwater-crystals and its entrapped brine [29].

## 1.3 Multiphase sea ice modelling

### 1.3.1 Theory of Porous Media

Sea ice presents itself as a multiphase material of liquid brine existing in a solid ice matrix and so multiphase modelling is required. The Theory of Porous Media (TPM), discussed in Chapter 3, will be used to investigate the aforementioned problems. For the initial development of the TPM sea ice model, it is to be an idealised biphasic model considering pure fresh water and neglecting gas inclusion. The idealization of the problem will be discussed further in Chapter 4.

## 1.4 Aims and objectives

This research project aims at developing a biphasic TPM sea ice model to aid in the understanding of the brine transport mechanisms in Antarctic sea ice. The afore-mentioned model will more specifically focus three multi-dimensional analysis.

More specifically, the objectives of the biphasic approach are as follows:

1. Describe the multi-dimensional nature of brine transport mechanisms in Antarctic sea ice mathematically while applying the relevant assumptions and boundary conditions based on a TPM-based continuum mechanics framework;
2. Asses the various brine removal mechanisms known to influence the transport of brine in sea ice by making use of the developed biphasic computational model; and
3. Assess the feasibility of using imagining analysis and processing as input for the developed computational model to investigate brine transport in Antarctic sea ice.

## 1.5 Scope and limitations

It is proposed that the brine transport model applicable to Antarctic sea ice be developed within TPM in order to study the multiphase characteristics of a sea ice problem. The model is to take into account liquid brine movement in a solid ice matrix at a short time interval and thus will not account for temperature variations in this time as this lies outside the scope of the project. This therefore neglects all potential effects of phase change. This study will also investigate sea ice composed on two phases namely solid ice and liquid brine. Additional constituents that may be present in sea ice lie outside the scope of this study. Salt is included in the composition of liquid brine however, salt transport is not explicitly considered but rather captured in the material properties of the liquid used in the TPM model.

## 1.6 Layout of document

Proceeding this introductory chapter, Chapter 2 discusses all theory regarding the formation, growth and structure of Antarctic sea ice. It also includes various brine transport mechanisms and the relevance of salinity profiles in sea ice. Chapter 3 introduces the Theory of Porous Media outlining key concepts, describing the kinematics and introduces that balance laws used in TPM. The next chapter, Chapter 4 deals with a more in-depth description of a biphasic TPM model specific to the sea ice problem at hand. It states all assumptions and derives the weak forms of the balance equations. This chapter also discusses a benchmark problem used to verify the model. The description and results of various sea ice problem simulations are discussed in Chapter 5 and the conclusions and future work of these problems is presented in Chapter 6.

# Chapter 2

# Properties and cycle of sea ice

## 2.1 The formation, growth and structure of sea ice

The following section provides an overview into the formation, growth and structure of sea ice. The structure of sea ice concerns the porous nature of sea ice and influencing factors that change the porous microstructure.

### 2.1.1 Formation of sea ice

Surface cooling as a result of seasonal variations begins to reduce the temperature of sea water. Sea water's salinity of 34 practical saline units PSU[1] results in a freezing temperature of -1.86°C [38] thus the addition of salt ions within sea water changes the physical properties of fresh water as it reduces it's freezing point [17]. The depth to which the ice freezes is largely dependent on the density of the ocean as the upper ocean's density gradient limits the depth to which low temperatures, required for freezing, can occur [27].

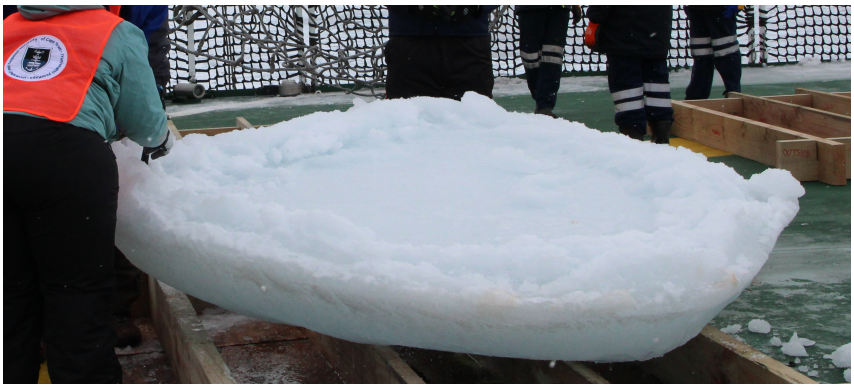

**Figure 2.1.** Image of ice pancake on deck taken on the 2019 SCALE winter cruise showing ridging along the outer perimeter of the pancake.

Frazil ice, resembling ice platelets and needles [17] of a three to four millimetre diameter, forming from surface sea water in turbulent conditions [2, 4] make up the first phase of the sea ice formation process. The turbulent conditions in which frazil grows typically aggregates

[1] ratio of grams of salt per kilograms of water [39]

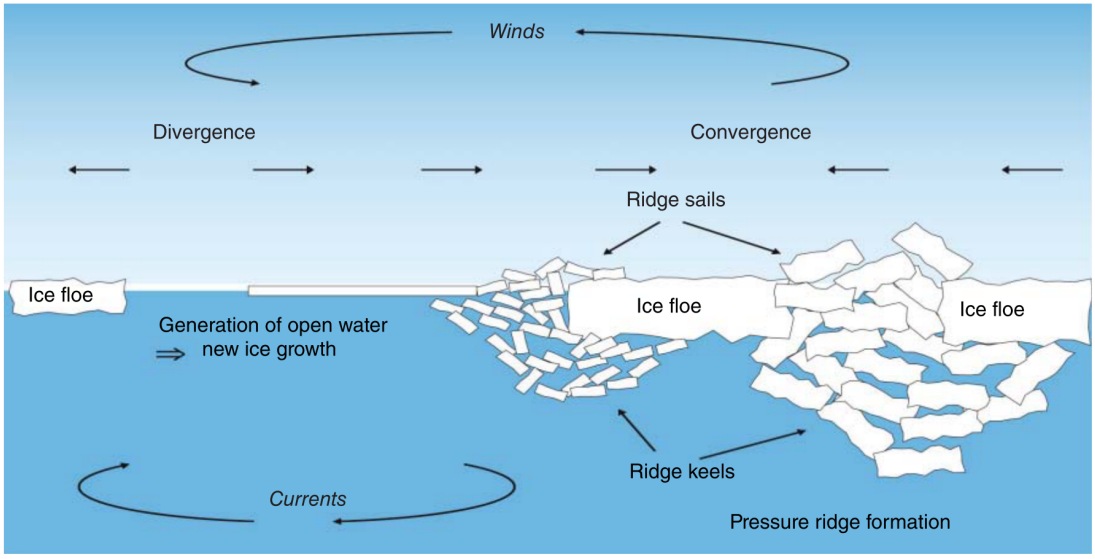


**Figure 2.2.** Schematic depicting the dynamic processes of young sea ice [20].

the ice into clusters and crystals [38]. Particulates and micro-organisms tend to get caught in these clusters of frazil ice bringing them to the surface.

As cooling continues to penetrate a greater depth of the ocean, salt ions are rejected from the ice matrix and are expelled into the ocean below [15, 22]. This occurs because salt cannot be incorporated in the pure ice crystal lattice [22]. This results in a decreased salt concentration within frazil ice [38]. The amount of frazil continues to increase resulting in a slushy upper layer on ocean. The Antarctic region favours the formation of frazil ice as a result of its higher wind speeds, larger spanning ocean swells and larger number of opening in an ice pack [38]. The growth of frazil ice in this region leads to the formation of pancake ice.

The ocean conditions are a large contributor to the process of ice formation. During calm conditions, a thin solid sheet of ice, known as grease [2], forms at the ocean-atmosphere interface [38]. This sheet is dark and becomes whiter as it thickens. As this sheet begins to thicken, wind or ocean currents may cause them to slide into or over each other. This process is known as rafting.

Wind action and/or currents may disturb the growth of a continuous ice sheet. The hindering growth of a continuous ice sheet results in the formation of smaller circular discs of ice known as pancake ice. Pancake ice is comprised of semi-consolidated frazil ice and pancakes are able to freeze together again to form a continuous ice sheet or larger ice floes[17]. Ice pancakes begin bumping into and grinding against each other due to movement from the ocean waves causing raised edges along the outside of the pancake as seen in Figure 2.1. Analysis of large floes or continuous ice sheets are composed of a *rough* surface of the sheet which is characteristic of the dynamic formation process of the ice and consists of multiple pancakes that have merged together often tilted or stacked together[38]. The dynamic processes of sea ice development can be seen in Figure 2.2.

### 2.1.2 Growth of sea ice

As stated in the afore-mentioned process, there is a microscopic exclusion of salt ions from the ice matrix as the sea ice begins to form. This does not affect the bulk salinity of the sea ice however results in an increased local brine salinity [38]. This continues as the ice grows resulting in an increased concentration of solute of a few millimetres thick at the ice-water interface [38]. As a result of the salt concentration gradient, the diffusion of salt begins to occur away from the ice-water interface into the ocean which is less saline [38]. Gow and Tucker [17] found that once a solid ice surface layer has formed, ice crystals lose a degree of freedom and begin to form columnar shaped crystal growth. The formation of the columnar shaped structure below the surface sheet of ice is known as congelation growth. As congelation

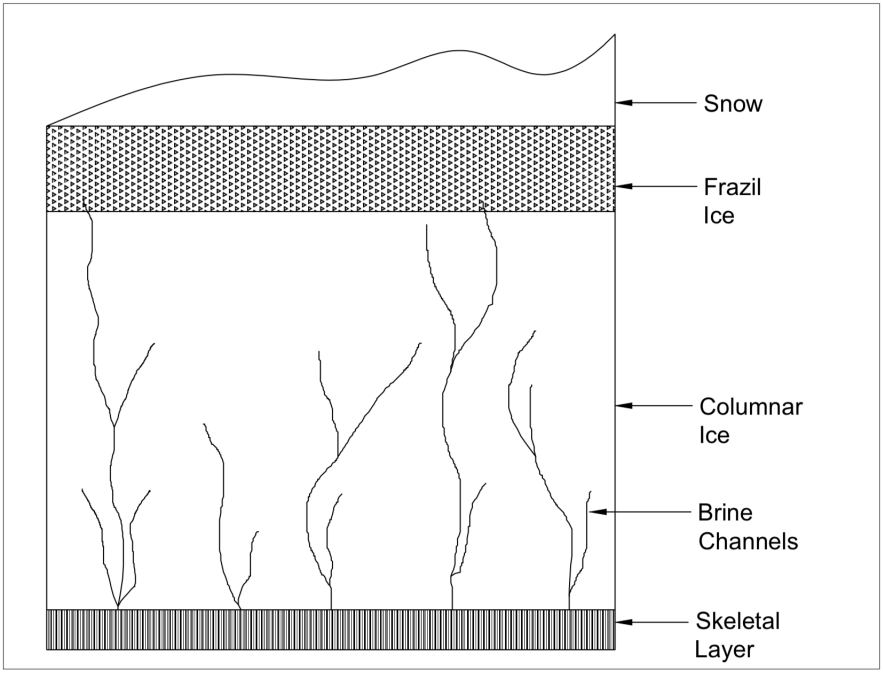


**Figure 2.3.** Schematic showing physical features of an typical ice pack. [2, reproduced].

growth continues to occur below the surface, the highly concentrated brine becomes trapped between the ice blades thus increasing the salinity of the ice [17]. The temperature at the lower boundary of the sea ice is just below that of the freezing point of sea water. This results in a highly porous, columnar ice layer known as the skeletal layer (Figure 2.3) [2]. The skeletal layer is typically highly permeable and forms a biological habitat for many micro organisms [42].

### 2.1.3 Porosity of sea ice

Porosity refers to the measure of void space within a material. In the case of sea ice, these voids include both air and brine [17]. The size and connectivity of these inclusions seen in Figure 2.4 vary with both salinity and temperature [26, 33]. The formation, consolidation and

melt processes of sea ice result in a fluid exchange between the sea ice and the underlying ocean [24]. The fraction of brine remaining within the ice pores largely influences the ices mechanical, thermal and electrical properties [5]. A small-scale marine environment exists within the ice pours and at the ice-water interface[33] and, as mentioned in subsection 2.1.2 is known as the skeletal layer. Knowledge of how brine inclusions change under varying sea ice conditions fosters a greater understanding as to how sea ice inclusions influence the small-scale marine environment that exists in the Southern Ocean. Temperature, salinity and time govern the size and connectivity of brine inclusions therefore influencing the overall porosity of the sea ice [26].

Gow and Tucker [17] describes how changes occurring in the distribution of brine as well as the concentration of salt within the sea ice are largely controlled by phase equilibrium as follows:

- Temperature changes within the ice may result in the freezing/melting of brine pocket walls. This in turn results in a reduction/enlargement in the size of the brine pockets which ultimately cause a decrease/increase in the volume of brine present in the sea ice.
- During warmer periods as a result of seasonal variations, brine inclusions will continue to enlarge and begin to join.
- Further warming may result in the the channelization of brine inclusions that cause brine drainage into the underlying ocean.

It is the distribution and inter-connectivity of sea ice pores that allows for brine transportation through sea ice. The permeability of the sea ice is largely dependent on the inter-connectivity of the sea ice pores hence changes within the microstructure of the ice pores as a result of varying temperatures from seasonal variations will result in changes to the permeability of the sea ice. The changes in the ice properties can be explained as a function of ice thickness [9]. It is challenging to analyse thin sections of ice samples in an attempt to quantitatively determine the pore structure of sea ice as the ice pores exist in three dimensions and need to be observed in such a way to account for the true structure [9]. Magnetic Resonance Imaging (MRI) is a three dimensional imaging technique that has been used to observe the pore structure of sea ice. An ice sample is scanned and two dimensional *slices* such as that in Figure 2.4 are generated which depict the internal pore structure of the ice. These two dimensional images can be merged together to recreate the three dimensional representation of the ice sample.

## 2.2 Salinity profiles

As stated in subsection 2.1.1, the ocean has a salinity of approximately 34PSU. The sea ice however has an approximate salinity of 5PSU [22] indicating that brine transport mechanisms are apparent within sea ice. It has been found that Antarctic sea ice has a salinity that is 0.5-1.0% higher than that of Arctic sea ice [16]. Eicken [7] shows how salinity profiles of Antarctic

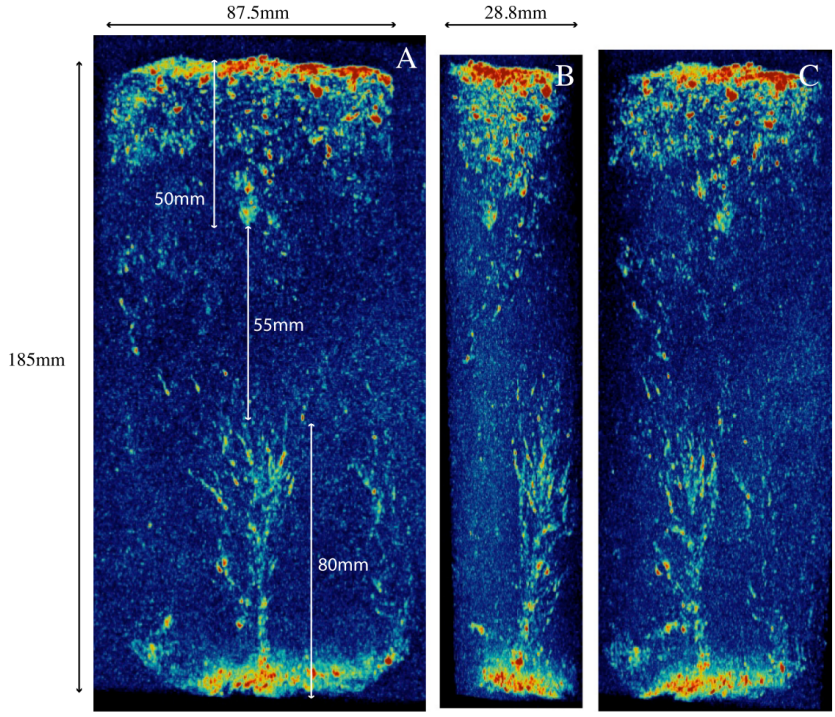


**Figure 2.4.** Magnetic resonance images (MRI) in a 3-dimensional sea ice core with a depth of 186 mm and a diameter of 87.5 mm. The brighter colours of this image shows the small brine entrapments in the pores at the top and bottom of the ice core as well as larger, channel like brine inclusions in the center [13].

sea ice differ more in shape than those of Arctic sea ice and attributes this difference to ice rafting, surface flooding and snow ice formation all of which occur frequently in the Antarctic.

Understanding the vertical *C-shaped* salinity profile and the weakening of this profile is done through understanding the roles of temperature and salinity with respect to the sea ice pores and its microstructure [38]. Figure 2.5 indicates the idealized salinity profile of Arctic sea ice. Profiles of young ice represent a high salinity at both the top and bottom of the ice causing a strong *C-shaped* curve [42]. An increase in age of the ice (thus resulting in an increase in thickness) results in a weakening of the c-shaped curve. This depicts the downwards movement of internal brine [17]. As brine removal from first-year ice continues and the ice becomes multi-year ice, there is a virtual desalination of the upper ice levels. This is due to the repetition of the brine transport mechanisms discussed in section 2.3 that occurs throughout each season as the ice's age increases.

Figure 2.7 provides a comprehensive summary to the properties of first sea ice with an increase in depth. It is evident that the highest salinity can be found within the consolidated frazil ice layer due to the entrapment of brine during the formation of sea ice as well as at the ice/ocean interface due to the expulsion of brine at this interface during ice formation discussed in subsection 2.1.1. The lower salinity present within the mixed columnar/granular and the columnar ice section is due to desalination mechanisms discussed in section 2.3.

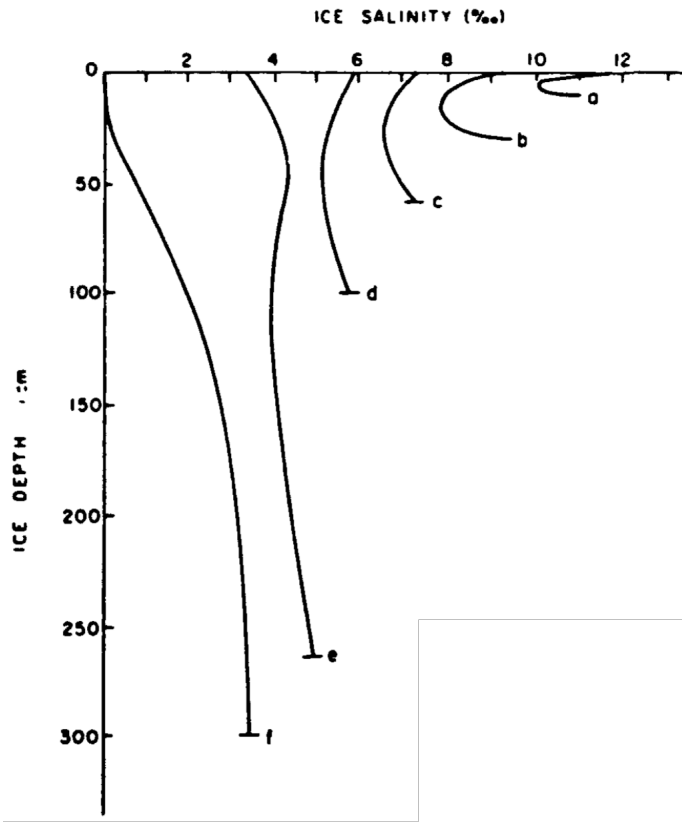


**Figure 2.5.** Idealized salinity profiles of Arctic sea ice. Profiles a-d represent the salinity observed in first year sea ice of varying thickness. The remaining curves (e and f) represent that of multiyear ice [17].

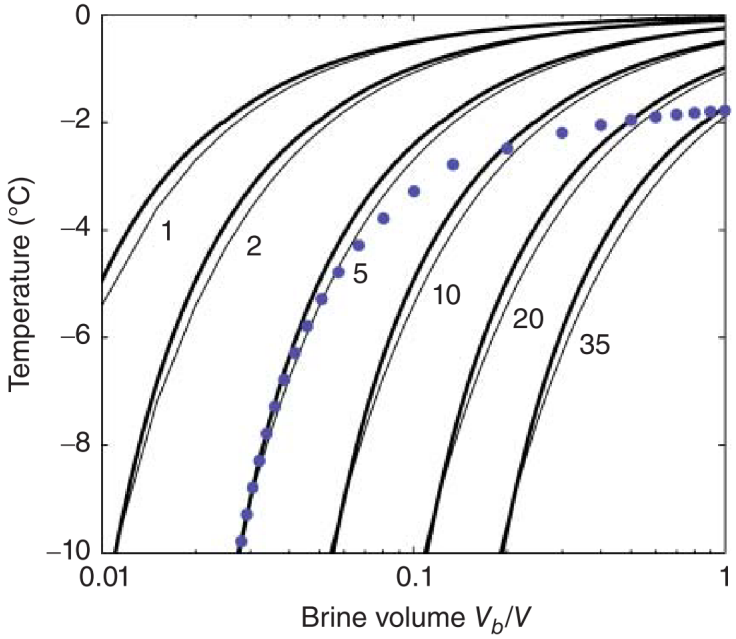


**Figure 2.6.** The relationship between liquid brine volume fraction and temperature for different values of sea ice bulk salinity [32].

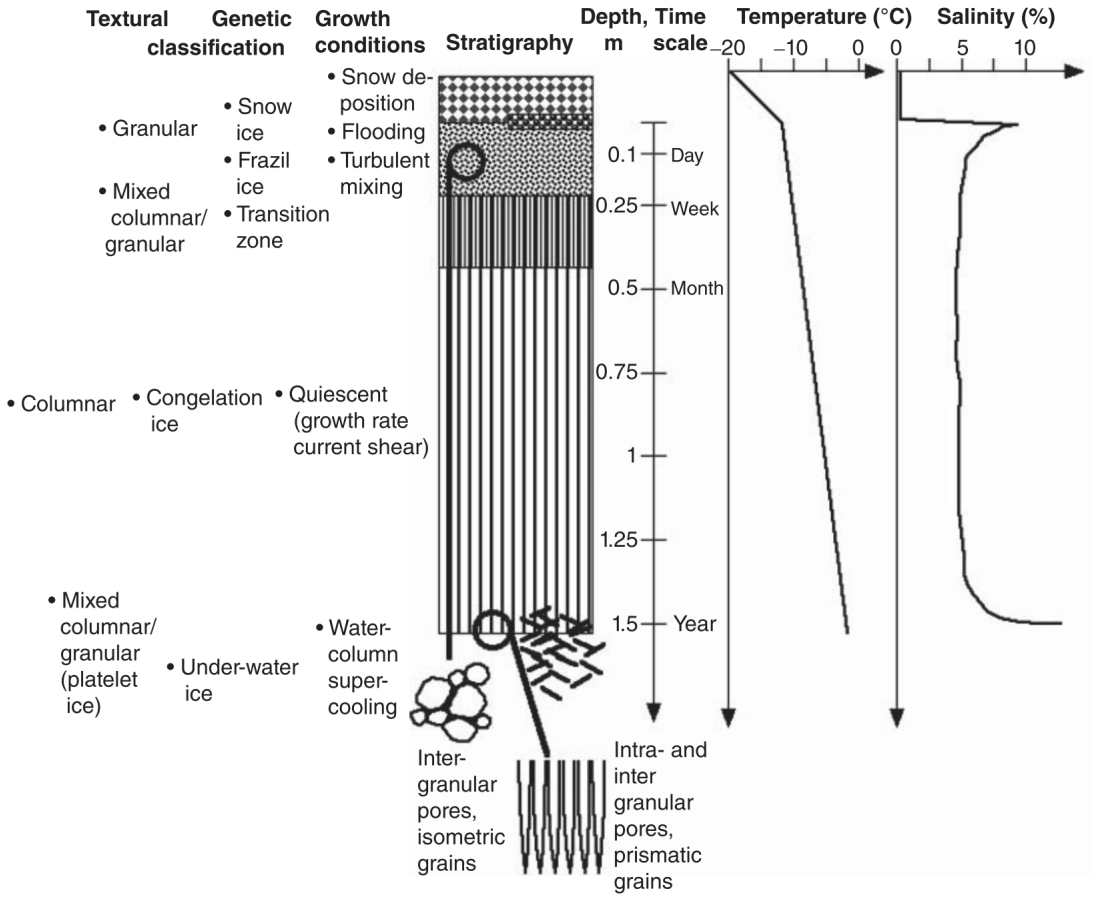


**Figure 2.7.** Schematic showing ice textures, depth and winter temperature-salinity profile of first-year ice [32].

## 2.3 Brine transport mechanisms

It is known that the conservation of mass dictates the volume of brine leaving and entering sea ice [38]. This leads to advective flux which not only results in the flux of brine but also, the flux of nutrients [22].

In addition to the initial salt rejection that occurs during sea ice formation, Gow and Tucker [17] introduce four means in which brine is said to be removed from sea ice:

- Salt diffusion
- Brine expulsion
- Gravity drainage and
- Flushing

During the cool winter months, gravity drainage is the most prominent means of brine removal and during the warmer summer months, flushing due to surface melt-water is the main cause

of desalination [42]. Both these pore prominent forms of brine transport through the sea ice depend on the ice's permeability [22].

It is also known that an inward flow of ocean water results in a reduced local and bulk salinity as well as the overall porosity of the ice [38].

Mushy layer theory is often used to described porous materials that have interstitial melt that moves through the porous solid [22] and is used in various models. Models such as those of Feltham *et al.*, [12], Vancoppenolle *et al.*, [41] and Notz *et al.*, [30] make use of mushy layer theory to describe the multiphase structure of sea ice. This consists of a pure ice solid matrix and impurity rich liquid brine [12]. The mushy layer theory makes use of volume averaged simulations [22].

### 2.3.1 Salt diffusion

The migration of brine pockets within the ice floes is governed by phase equilibrium as a result of temperature and salinity variations. As the temperature within the ice continues to decrease, liquid brine trapped within the ice pores begins to freeze, expelling salt ions into the surrounding brine. This process results in a continuously increasing salt concentration in the remaining brine-filled pore volume. Similarly, as the ice begins to warm, the surrounding brine inclusions melt and the salt concentration of the trapped brine decreases. From the aforementioned process, it is evident that brine pockets will migrate towards warmer areas within the ice. If the brine pockets located around edges of the ice are exposed to warming temperatures, their walls will melt thereby allowing the brine to escape from the ice floe. This means of desalination will inevitably contribute to small amounts of brine loss but will however contribute largely to the distribution of brine within the ice [17].

Notz *et al.*, [30] made use of their 1-D model based on *Mushy layer* theory to determine that salt diffusions contribution to desalination in both, brine pockets and interconnected brine channels is negligible. Untersteiner *et al.*,[40] found that the small amounts of downward migration of brine are compensated by the upward migration and thus found the effects of this to be negligible.

### 2.3.2 Brine expulsions

Brine expulsion accounts for a minor portion of the total desalination of first-year ice. As the temperature of the ice decreases and brine inclusions begin to freeze, a pressure build-up within the brine pockets occur. This pressure build-up is the result of the specific volume of ice being greater than that of water [24] and will drive brine either upward or downward [30]. The brine will then be expelled downward into the ocean below or upward towards the surface. The expulsion of brine to the sea ice surface is mostly evident in thin ice undergoing rapid cooling [17].

Griewank *et al.*,[18] study brine expulsion using a 1-D thermodynamic sea ice model SAMSIM (semiadaptive multiphase sea-ice model) by accounting for the volume of brine expelled. This is done by summing the volume of liquid brine and solid ice in the layer at each time step

and determining if it exceeds the total volume of the layer. If it exceeds the volume of the layer, it is said that the brine has moved to the layer below. However it does not account for the upward movement of brine as it is assumed that upward movement of brine is less likely than the downward movement. Notz *et al.*, [30] on the other hand determined that the growth rate of the ice at the ice-ocean interface is always greater than that of the brine velocity of brine expulsion and so brine expulsion of growing sea ice cannot allow brine to leave the ice. Downward brine expulsion during growth can only cause a redistribution of brine within the ice. The upward movement of brine can however result in a thin layer of highly concentrated brine forming on the sea ice surface [22].

### 2.3.3 Gravity drainage

Brine drainage otherwise know as brine drainage is the process whereby the brine drains out of the ice sheet into the underlying ocean [24]. The temperature gradient as a result of surface cooling in the ice is accompanied by a salinity gradient to maintain phase equilibrium. As the ice continues to cool, the higher brine densities present at the top of the ice result in an unstable density gradient [30]. This can cause convective overturning whereby the brine drains out of the channels into the underlying ocean and is replaced with fresher sea water [29].

This process is governed by isostatic equilibrium of the ice [17] as the ice rises above the ocean surface as it thickens. This process results in a pressure head forming within the brine inclusions which in turns drives the brine out of the channels into the underlying ocean. Gow and Tucker[17] record that this drainage process occurs in brine channels of 5mm diameter or greater. The discharge of brine can cause hollow "tubes" within the ice commonly known as *ice stalactites* [24].

Griewank *et al.*, [18] study gravity drainage using SAMSIM to determine how gravity drainage affects the thermodynamic properties of the sea ice. 1-D models, unlike 2-D and 3-D models are not able to resolve a convective process and so gravity drainage can only be parametrized [18]. SANSIM makes use of two parametrizations of gravity drainage: *convective* parametrization to simulate the movement of brine to attempt to produce a salinity evolution at low computational cost [18].

Additionally, the downward flow of brine increases the local salinity of the sea ice. An increase in the inclusion's local salinity causes dissolution within the ice matrix forming brine channels [32]. With continuing salt rejection the downwards moving brine experiences an increase of salinity which causes super-heating (i.e. the increase in salinity decreases the brines freezing point). As a result of the super-heated brine, the surrounding ice melts to maintain thermodynamic equilibrium [31] causing brine plumes/streamers.

Mushy layer theory accounts for the desalination of sea ice through convective overturning, the process whereby brine within the ice is replaced with underlying sea water [30]. This process is governed by the Rayleigh number. Once it has exceeded a threshold, convection occurs and the brine is *lost* to the underlying ocean [22].

### 2.3.4 Flushing

Flushing, although similar to gravity drainage, occurs during the spring/summer seasons. The surface ice begins to melt causing a meltpond to form at the top of the ice. The relatively fresh water that lies on the ice surface percolates the sea ice pores resulting in the *washing out* of the salty brine that exists within the ice pores. [22, 30] This mechanism of brine transportation is more prominent in the Arctic region. Weeks and Ackley [1] explain that the temperature change during with spring/summer seasons in the Arctic correspond to the period where salinity changes within the ice occur.

Modelling of flushing requires both the horizontal and vertical permeability of sea ice which is constantly changing [18] thus making this multidimensional process difficult to model [8] as changing permeability is difficult to determine experimentally.

The use of 1-D simulations are common in sea ice simulations. This is done for computational efficiency and because of the primarily vertical nature of first-order thermodynamic conduction [22]. These 1-D models can therefore not fully describe the multidimensional nature of flushing.

Notz *et al.*, [29] account for only the vertical movement of brine due to flushing in their 1-D enthalpy model. Notz *et al.*, [30], based on this 1-D enthalpy model also make use of a 1-D model to examine the evolution of the bulk salinity within sea ice. Jeffery *et al.*, [25] developed the *IceT* model to describe only vertical brine transport of liquid brine. The SIMSAM model discussed in Griewank *et al.*, [18] accounts for permeability in sea ice by defining it as an empirical function of the fluid volume fraction. Gough *et al.*, [15] states that desalination processes of sea ice are largely unaffected by the sea ice structure and by defining permeability as an empirical function of the fluid volume, it neglects the ice structure [18]. The use of a multidimensional model will enhance the accuracy or brine movement due to flushing as recognised as by Notz *et al.*, [30] who state that the lack of a horizontal component in their 1-D model will not capture all aspects of flushing desalination.

## 2.4 Discussion

Sea ice models are formed from continuum mechanics expressions of local balance equations of mass, momentum and heat. These balance equations are affected by dynamic, thermodynamic and chemical processes. In numerical simulations of brine transport processes in sea ice it is common to treat thermal changes as well as motion and deformation as one-dimensional problems [12].

Sea ice is a porous solid that is saturated with liquid brine from the underlying ocean as well as gases from the surrounding atmosphere (Figure 2.8). Along with these two major components within the solid matrix are constituents such as solid salts, trace elements, microalgae and other impurities [22, 23, 39]. These multiple components interact with one another to form multiphasic sea ice. The growth direction of the pure ice crystal plates varies and the location of brine inclusions dependent on temperature and salinity.

Numerical modellers often assume sea ice to be impermeable to gas exchange to aid in the development of numerical models by simplifying its composition to only solid ice and liquid brine [25]. For the purpose of this study, idealised, gas free samples of sea ice are investigated as in other models such as Feltham *et al.*[12] Notz *et al.*[30], Jeffery *et al.*[25] and Wells *et al.*[42].

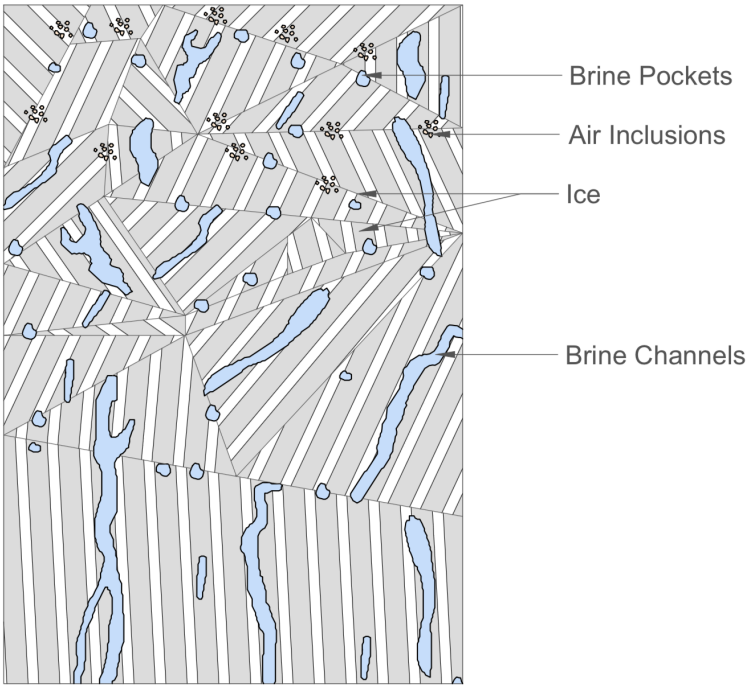


**Figure 2.8.** Schematic depicting the multiphase composition of sea ice made up of a porous solid (ice), liquid (brine) and gas (air).

It can be noted from the above literature that models have been used to investigate the brine movement within sea ice however, the need for a multidimensional sea ice model has been identified to capture both horizontal and vertical brine movement [18].

# Chapter 3

# Porous media theory

## 3.1 Introduction to Porous Media Theory

In order to accurately predict the responses and reactions of materials undergoing external and internal loading, these materials need to be described precisely. The composition of the material body in question is essential to understanding its behaviour. Solid materials often have many pores. Examples of these materials include ceramics, soil and sea ice. Often, these pores are filled with fluid. The solid and fluid constituents have different material properties and undergo different motions which often results in an interaction between the solid and fluid constituents. Continuum mechanics problems such as this one cannot be uniquely classified within the well-known disciplines like *"fluid mechanics"* and *"solid mechanics"* [6] and thus must be classified as multiphase problems.

The Theory of Porous Media can be used to describe the thermomechanical behaviour of porous solids. These porous solids can be partly/fully saturated, or empty. In the case of sea ice, the TPM framework will be applied to a solid porous skeleton that is fully saturated with fluid (both liquid and gas). The following introduces TPM's mathematical framework.

## 3.2 Volume fraction concept

When considering the volume fraction concept, it is assumed that the solid porous skeleton is the control space and that liquids and/or gases contained in the pores of the solid can leave the control space. It is also challenging to describe the exact location and properties of the pores within the solid and so it is assumed that they are statistically distributed across an arbitrary volume element composed of the volume elements of the real constituents $\kappa$. The constituents, are assumed to be "smeared" over the control space (Figure 3.1). This means that constituent occupies the total volume of the space simultaneously with all other constituents. The true structure consists of solid $\mathrm{dv}^{\mathrm{S}}$ and fluid $\mathrm{dv}^{\mathrm{F}}$ volume elements. The volume fraction of solid and fluid are $\mathrm{n}^{\mathrm{S}}$ and $\mathrm{n}^{\mathrm{F}}$ respectively. The solid and fluid constituents are then "smeared" over the control space.

Consider a porous material composed of $\kappa$ constituents. These constituents $\varphi^{\alpha}$ are of a solid phase that is saturated by fluid phases. It is assumed that each individual constituent $\varphi^{\alpha}$ occupies the control space $\mathcal{B}_S$ simultaneously. The boundary of the control space $\partial\mathcal{B}_S$ encloses the constituents $\varphi^{\alpha}$ of real volumes $\mathrm{v}^{\alpha}$ where $\alpha \,\epsilon\, \{\mathrm{S}, \mathrm{F}\}$.

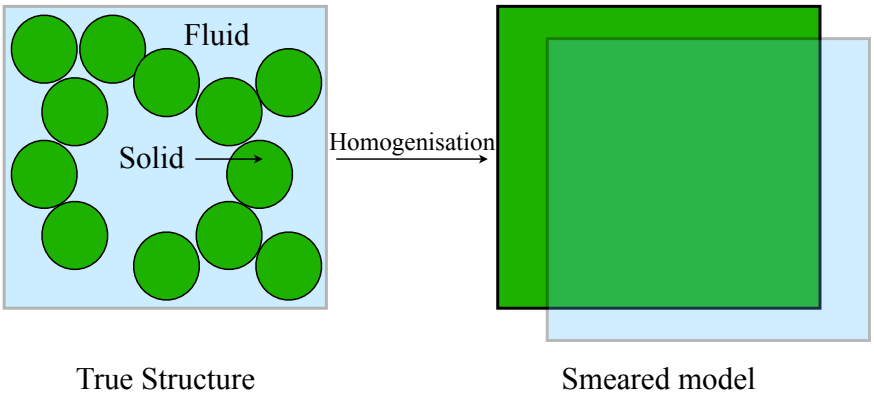


**Figure 3.1.** Schematic showing the true structure of a porous solid and its smeared idealized representation within a volume element.

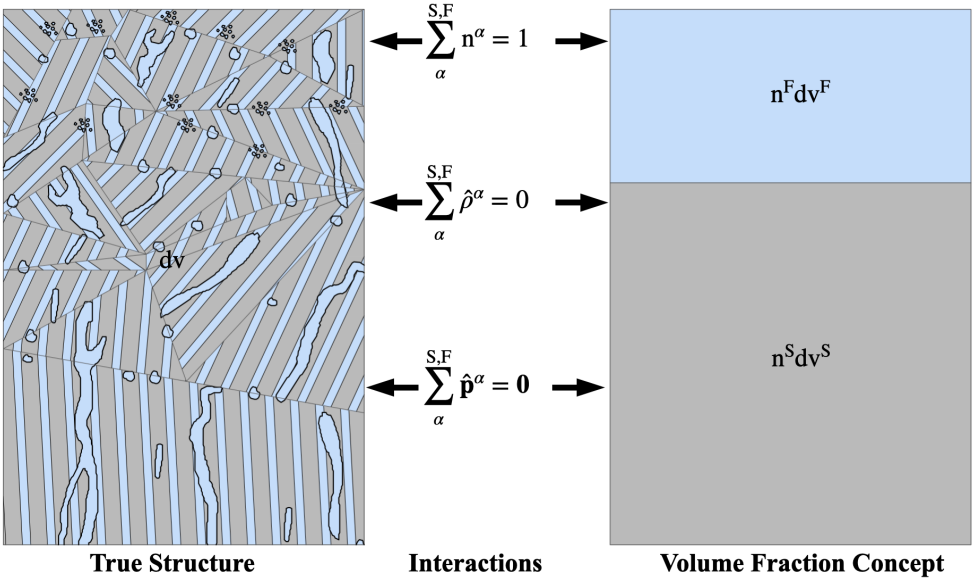


**Figure 3.2.** Volume fraction concept

Volume fraction concept showing the true structure of sea ice and its smeared idealized representation within a volume element. The true structure consists of solid $dv^S$ and fluid $dv^F$ volume elements. The volume fraction of solid and fluid are $n^S$ and $n^F$ respectively. These elements are related via the mass supply, $\hat{\rho}^{\alpha} = 0$ and interaction forces $\hat{\mathbf{p}}^{\alpha} = \mathbf{0}$

In the reference configuration at material point $X_\alpha$ at position $\mathbf{X}_\alpha$ where time $t = t_0$, the reference volume fraction is described as

$$n^{\alpha}_{0\alpha} = n^{\alpha}_{0\alpha}, (\mathbf{X}_\alpha, t = t_0) \tag{3.1}$$

and links the partial volume element $dV_{0\alpha}$ to the real volume element $dV^{\alpha}_{0\alpha}$ of the constituents $\varphi^{\alpha}$ at position $\mathbf{X}_\alpha$ . The partial volume $dV_{0\alpha}$ is described as

$$V^{\alpha}_{0} = \int_{\mathcal{B}_{0S}} n^{\alpha}_{0\alpha} dV_{0\alpha} = \int_{\mathcal{B}_{0S}} dV^{\alpha}_{0\alpha}. \tag{3.2}$$

The total volume of the control space is defined as

$$\mathrm{V}_0 = \int_{\mathcal{B}_{0\mathrm{S}}} \mathrm{dV}_{0\alpha} = \sum_{\alpha=1}^{\kappa} \mathrm{V}_0^{\alpha} = \int_{\mathcal{B}_{0\mathrm{S}}} \sum_{\alpha=1}^{\kappa} \mathrm{dV}_{0\alpha}^{\alpha} = \int_{\mathcal{B}_{0\mathrm{S}}} \sum_{\alpha=1}^{\kappa} \mathrm{n}_{0\alpha}^{\alpha}. \tag{3.3}$$

The saturation condition

$$\sum_{\alpha=1}^{\kappa} \mathrm{n}_{0\alpha}^{\alpha} = 1, \tag{3.4}$$

must be fulfilled at every point in the control space $\mathcal{B}_{0S}$.

The volume fraction $\mathrm{n}^{\alpha}$ is the ratio between the partial volume element of each constituent $\mathrm{dv}^{\alpha}$ to that of the bulk total volume dv of the material with

$$\mathrm{n}^{\alpha}(\mathrm{x},\mathrm{t}) = \frac{\mathrm{dv}^{\alpha}}{\mathrm{dv}}, \qquad \sum_{\alpha}^{\mathrm{S,F}} \mathrm{n}^{\alpha}(\mathrm{x},\mathrm{t}) = \sum_{\alpha}^{\mathrm{S,F}} \frac{\rho^{\alpha}}{\rho^{\alpha\mathrm{R}}} = 1, \tag{3.5}$$

where $\mathrm{n}^{\alpha}$ is specified for a constituent $\varphi^{\alpha}$ in the actual configuration and where t is the time.

The volume fractions defined in $(3.5)_1$ satisfies the saturation condition in $(3.5)_2$ where the partial density $\rho^{\alpha} = \mathrm{n}^{\alpha}\rho^{\alpha\mathrm{R}}$ of constituents $\varphi^{\alpha}$ to the real density $\rho^{\alpha\mathrm{R}}$.

The total mass of all $\kappa$ constituents in the porous body in the reference configuration is

$$\mathrm{M}_0 = \sum_{\alpha=1}^{\kappa} \mathrm{M}_0^{\alpha} = \int_{\mathcal{B}_{0\mathrm{S}}} \sum_{\alpha=1}^{\kappa} \rho_{0\alpha}^{\alpha} \mathrm{dV}_{0\alpha} \tag{3.6}$$

and in the actual configuration is

$$\mathrm{M} = \sum_{\alpha=1}^{\kappa} \mathrm{M}^{\alpha} = \int_{\mathcal{B}_{\mathrm{S}}} \sum_{\alpha=1}^{\kappa} \rho^{\alpha} \mathrm{dv}. \tag{3.7}$$

The partial densities in the reference and actual configuration are as follows

$$\rho_{0\alpha}^{\alpha} = \rho_{0\alpha}^{\alpha}(\mathbf{X}_{\alpha}, \mathrm{t} = \mathrm{t}_0) \tag{3.8}$$

and

$$\rho^{\alpha} = \rho^{\alpha}(\mathbf{x}, \mathrm{t}) \tag{3.9}$$

respectively.

The real density in the reference configuration is described as

$$\rho_{0\alpha}^{\alpha\mathrm{R}} = \rho_{0\alpha}^{\alpha\mathrm{R}}(\mathbf{X}_{\alpha}, \mathrm{t} = \mathrm{t}_0) \tag{3.10}$$

relating to the partial volume element $\mathrm{dV}_{0\alpha}^{\alpha}$ for the actual configuration with

$$\rho^{\alpha\mathrm{R}} = \rho^{\alpha\mathrm{R}}(\mathbf{x}, \mathrm{t}) \tag{3.11}$$

relating to the partial volume element dv.

The partial mass of the constituents $\varphi^\alpha$ is

$$\mathrm{M}_0^\alpha = \int_{\mathcal{B}_{0\mathrm{S}}} \rho_{0\alpha}^\alpha \mathrm{dV}_{0\alpha} = \int_{\mathcal{B}_{0\mathrm{S}}} \rho_{0\alpha}^{\alpha\mathrm{R}} \mathrm{dV}_{0\alpha}^\alpha \tag{3.12}$$

or

$$\mathrm{M}^\alpha = \int_{\mathcal{B}_\mathrm{S}} \rho^\alpha \mathrm{dv} = \int_{\mathcal{B}_\mathrm{S}} \rho^{\alpha\mathrm{R}} \mathrm{dv}^\alpha. \tag{3.13}$$

The partial and real densities

$$\rho_{0\alpha}^\alpha = \mathrm{n}_{0\alpha}^\alpha \rho_{0\alpha}^{\alpha\mathrm{R}} \tag{3.14}$$

or

$$\rho^\alpha = \mathrm{n}^\alpha \rho^{\alpha\mathrm{R}}. \tag{3.15}$$

The real densities are the true densities of the constituents on a macro-level. This differs from mixture theory as describing compressible and incompressible material phases in porous media can be done using the volume fraction concept.

## 3.3 Kinematics

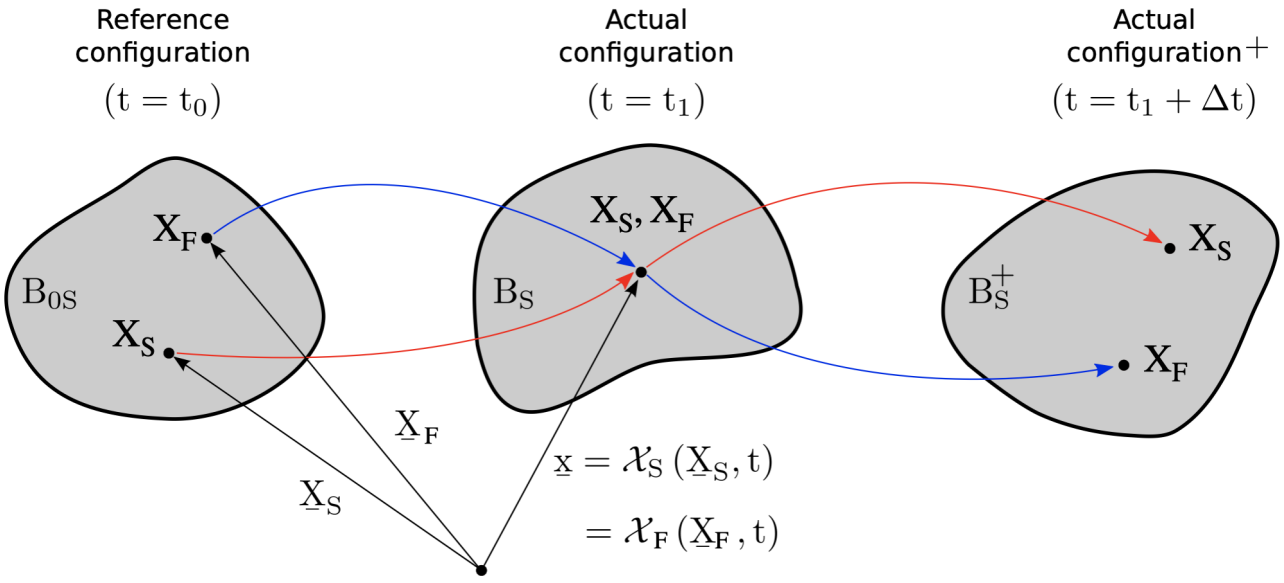


**Figure 3.3.** An illustration of motion in a porous solid saturated by a fluid [34, reproduced].

Consider a saturated, non-homogeneous (immiscible) mixture of all constituents $\varphi^\alpha$ with particles $\mathrm{X}_\alpha$. The particle bodies are in the ideal state of disorder i.e. the particles are statistically distributed over a control space. At any time t, each spatial point $\mathbf{x}$ of the actual placement

must simultaneously be occupied by material points $\mathrm{X}_\alpha$ of all $\kappa$ constituents $\varphi^\alpha$. Each individual constituent has an independent motion and therefore, material points $\mathrm{X}_\alpha$ must have been located at different reference positions at $\mathrm{t} = \mathrm{t}_0$. The motion function is defined as

$$\mathbf{x} = \mathcal{X}_\alpha(\mathbf{X}_\alpha, \mathrm{t}) \qquad \mathbf{x} \in \mathcal{B}_\mathrm{s} \tag{3.16}$$

and is unique and continuous. The motion of a porous solid saturated by a fluid can be seen in Figure 3.3. The velocity and acceleration in the Lagrangian configuration are

$$\mathbf{x}_\alpha^{'} = \frac{\partial \mathcal{X}_\alpha(\mathbf{X}_\alpha, \mathrm{t})}{\partial \mathrm{t}} \qquad \text{and} \qquad \mathbf{x}_\alpha^{''} = \frac{\partial^2 \mathcal{X}_\alpha(\mathbf{X}_\alpha, \mathrm{t})}{\partial \mathrm{t}^2}. \tag{3.17}$$

Inverting (3.16) gives the Eularian description of motion

$$\mathbf{X}_\alpha = \mathcal{X}_\alpha^{-1}(\mathbf{x}, \mathrm{t}). \tag{3.18}$$

An alternative expression of velocity and acceleration is

$$\mathbf{x}_\alpha^{'} = \mathbf{x}_\alpha^{'}(\mathbf{x}, \mathrm{t}) = \mathbf{x}_\alpha^{'}[\mathcal{X}_\alpha^{-1}(\mathbf{x}, \mathrm{t}), \mathrm{t}] \qquad \text{and} \qquad \mathbf{x}_\alpha^{''} = \mathbf{x}_\alpha^{''}(\mathbf{x}, \mathrm{t}) = \mathbf{x}_\alpha^{''}[\mathcal{X}_\alpha^{-1}(\mathbf{x}, \mathrm{t}), \mathrm{t}]. \tag{3.19}$$

The Eularian description of motion (3.18) implies a non-singular Jacobian

$$\mathrm{J}_\alpha = \mathrm{det}\mathbf{F}_\alpha \neq 0 \tag{3.20}$$

where $\mathbf{F}_\alpha$ denotes the deformation gradient of the constituents $\varphi^\alpha$ which, in the Lagrangian description, is

$$\mathbf{F}_\alpha = \frac{\partial \mathcal{X}_\alpha(\mathbf{X}_\alpha, \mathrm{t})}{\partial \mathbf{x}_\alpha} = \mathrm{Grad}_\alpha \mathcal{X}_\alpha. \tag{3.21}$$

The inverse of the deformation gradient yields the Eulerian description for the deformation gradient

$$\mathbf{F}_\alpha^{-1} = \frac{\partial \mathcal{X}_\alpha^{-1}(\mathbf{X}_\alpha, \mathrm{t})}{\partial \mathbf{x}_\alpha} = \frac{\partial \mathbf{X}_\alpha}{\partial \mathbf{x}} = \mathrm{grad}\mathbf{X}_\alpha. \tag{3.22}$$

The material and spatial velocity gradients are

$$(\mathbf{F}_\alpha)_\alpha^{'} = \frac{\partial \mathbf{x}_\alpha^{'}}{\partial \mathbf{X}_\alpha} = \mathrm{Grad}\mathbf{x}_\alpha^{'} \qquad \text{and} \qquad \mathbf{L}_\alpha = (\mathrm{Grad}\mathbf{x}_\alpha^{'})\mathbf{F}_\alpha^{-1} = \mathrm{grad}\mathbf{x}_\alpha^{'} \tag{3.23}$$

respectively. The decomposition of the spatial velocity gradient

$$\mathbf{L}_\alpha = \mathbf{D}_\alpha + \mathbf{W}_\alpha, \tag{3.24}$$

yields the symmetric $\mathbf{D}_\alpha$ and skew-symmetric $\mathbf{W}_\alpha$ spin tensor

$$\mathbf{D}_\alpha = \frac{1}{2}(\mathbf{L}_\alpha + \mathbf{L}_\alpha^T) \qquad \text{and} \qquad \mathbf{W}_\alpha = \frac{1}{2}(\mathbf{L}_\alpha - \mathbf{L}_\alpha^T). \tag{3.25}$$

Due to the fact that the constituents have different motions, they therefore have different material time derivatives which for an arbitrary scalar-valued function $\mathit{\Gamma}(\mathbf{x}, \mathrm{t})$ is given by

$$\mathit{\Gamma}_\alpha^{'} = \frac{\partial \mathit{\Gamma}}{\partial t} + [\mathrm{grad}\Gamma] \cdot \mathbf{x}_\alpha^{'}. \tag{3.26}$$

## 3.4 Balance equations

The balance equations are established for each individual constituent $\varphi^\alpha$ and the interaction between the constituents must be considered. The summation of the balance equations of all $\kappa$ constituents results in the balance equation of a one-component material when they become superimposed. This is the third metaphysical principle of Truesdell. Furthermore, the sum of the interaction effects must be equal to zero.

### 3.4.1 Balance of mass

The balance of mass for constituents $\varphi^\alpha$ is such that the rate of mass is equal to the mass supply

$$(\mathrm{M}^\alpha)'_\alpha = \int_{\mathcal{B}_\alpha} \hat{\rho}^\alpha \mathrm{dv} = \hat{\mathrm{M}}^\alpha \tag{3.27}$$

where the mass of the constituents $\varphi^\alpha$ is defined as

$$\mathrm{M}^\alpha = \int_{\mathcal{B}_\alpha} \rho^\alpha \mathrm{dv} \tag{3.28}$$

and $\hat{\rho}^\alpha$ corresponds to the local mass supply.

The mass supply $\hat{\rho}^\alpha$ results from the mass exchange between constituents $\varphi^\alpha$ and the remainder of the constituents $(\kappa - 1)$ present at $\mathbf{x}$ at time t. Mass exchange can for example be a result of chemical reactions of phase transitions. Using the transport theorem,

$$(\mathrm{dv})'_\alpha = \mathrm{div}\mathbf{x}'_\alpha \mathrm{dv} \tag{3.29}$$

and with the rate of mass exchange $(\mathrm{M}^\alpha)'_\alpha$ (3.27) the global balance of mass is

$$\int_{\mathcal{B}_\alpha} [(\rho^\alpha)'_\alpha + \rho^\alpha \mathrm{div}\mathbf{x}'_\alpha]\mathrm{dv} = \int_{\mathcal{B}_\alpha} \hat{\rho}^\alpha \mathrm{dv} \tag{3.30}$$

and the local balance of mass

$$(\rho^\alpha)'_\alpha + \rho^\alpha \mathrm{div}\mathbf{x}'_\alpha = \hat{\rho}^\alpha \tag{3.31}$$

The summation of (3.31) yields

$$\sum_{\alpha=1}^{\kappa} [(\rho^\alpha)'_\alpha + \rho^\alpha \mathrm{div}\mathbf{x}'_\alpha] = \sum_{\alpha=1}^{\kappa} \hat{\rho}^\alpha \stackrel{!}{=} 0 \tag{3.32}$$

which can only be true if

$$\sum_{\alpha=1}^{\kappa} \hat{\rho}^\alpha \stackrel{!}{=} 0. \tag{3.33}$$

With the absence of mass exchange between the constituents $\varphi^\alpha$ the following can be obtained from 3.31

$$\rho^\alpha = \rho^\alpha_{0\alpha} (\det \mathbf{F}_\alpha)^{-1}. \tag{3.34}$$

### 3.4.2 Balance of momentum

The balance equation of momentum with

$$(\mathbf{l}^{\alpha})'_{\alpha} = \mathbf{k}^{\alpha} + \int_{\mathcal{B}_{\alpha}} \hat{\mathbf{p}}^{\alpha} \mathrm{dv} \tag{3.35}$$

states the material time derivative of momentum equals the sum of the external forces where $\hat{\mathbf{p}}$ is the interaction force between phases. In (3.35),

$$\mathbf{l}^{\alpha} = \int_{\mathcal{B}_{\alpha}} \rho^{\alpha} \mathbf{x}'_{\alpha} \mathrm{dv} \tag{3.36}$$

and

$$\mathbf{k}^{\alpha} = \int_{\mathcal{B}_{\alpha}} \rho^{\alpha} \mathbf{b}^{\alpha} \mathrm{dv} + \int_{\partial\mathcal{B}_{\alpha}} \mathbf{t}^{\alpha} \mathrm{da} \tag{3.37}$$

are quantities that denote the momentum $\mathbf{l}^{\alpha}$ and $\mathbf{k}^{\alpha}$ is the external force vector. The local volume force is $\rho^{\alpha}\mathbf{b}^{\alpha}$ and $\mathbf{t}^{\alpha}$ is the external surface force.

$$\int_{\partial\mathcal{B}_{\alpha}} \mathbf{t}^{\alpha} \mathrm{da} = \int_{\partial\mathcal{B}_{\alpha}} \mathbf{T}^{\alpha}\mathbf{n} \mathrm{da} = \int_{\partial\mathcal{B}_{\alpha}} \mathbf{T}^{\alpha}\mathbf{da} \tag{3.38}$$

where $\mathbf{T}$ is the *Cauchy* stress tensor. The term $\mathrm{d}\mathbf{a} = \mathbf{n}\mathrm{da}$ represents a surface element in the actual configuration and $\mathbf{n}$ denotes the outstanding unit normal at the surface of the body. The local supply term is given by the interaction forces is

$$\hat{\mathbf{p}}^{\alpha} = \hat{\mathbf{p}}^{\alpha}(\mathbf{x}, \mathrm{t}). \tag{3.39}$$

Using the material time derivative of momentum

$$(\mathbf{l}^{\alpha})'_{\alpha} = \int_{\mathcal{B}_{\alpha}} (\rho^{\alpha}\mathbf{x}''_{\alpha} + \hat{\rho}^{\alpha}\mathbf{x}'_{\alpha})\mathrm{dv} \tag{3.40}$$

and the divergence theorem

$$\int_{\partial\mathcal{B}_{\alpha}} \mathbf{T}^{\alpha}\mathbf{n} \mathrm{da} = \int_{\mathcal{B}_{\alpha}} \mathrm{div}\mathbf{T}^{\alpha} \mathrm{dv} \tag{3.41}$$

and using (3.35) and (3.36) , the balance equation of momentum (3.37) can be transformed to

$$\int_{\mathcal{B}_{\alpha}} (\rho^{\alpha}\mathbf{x}''_{\alpha} + \hat{\rho}^{\alpha}\mathbf{x}'_{\alpha})\mathrm{dv} = \int_{\mathcal{B}_{\alpha}} (\mathrm{div}\mathbf{T}^{\alpha} + \rho^{\alpha}\mathbf{b}^{\alpha})\mathrm{dv} + \int_{\mathcal{B}_{\alpha}} \hat{\mathbf{p}}^{\alpha}\mathrm{dv} \tag{3.42}$$

or in local form

$$\mathrm{div}\mathbf{T}^{\alpha} + \rho^{\alpha}(\mathbf{b}^{\alpha} - \mathbf{x}''_{\alpha}) = \hat{\rho}^{\alpha}\mathbf{x}'_{\alpha} - \hat{\mathbf{p}}^{\alpha}. \tag{3.43}$$

The sum of the local form of the balance of momentum (3.43) over all $\kappa$ constituents

$$\sum_{\alpha=1}^{\kappa} [\mathrm{div}\mathbf{T}^{\alpha} + \rho^{\alpha}(\mathbf{b}^{\alpha} - \mathbf{x}''_{\alpha})] = \sum_{\alpha=1}^{\kappa} [\hat{\rho}\mathbf{x}'_{\alpha} - \hat{\mathbf{p}}^{\alpha}] \tag{3.44}$$

yields the local balance of momentum equation of the mixture. The interaction force between the phases must be in equilibrium

$$\sum_{\alpha=1}^{\kappa} \hat{\mathbf{p}}^{\alpha} \stackrel{!}{=} 0. \tag{3.45}$$

### 3.4.3 Balance of moment of momentum

Assuming non-polar, partial bodies, the balance of the moment of momentum equation of a fixed point 0 is

$$(\mathbf{h}^{\alpha}_{(0)})^{'}_{\alpha} = \mathbf{m}^{\alpha}_{(0)} + \hat{\mathbf{h}}^{\alpha}_{(0)} \tag{3.46}$$

where

$$\mathbf{h}^{\alpha}_{(0)} = \int_{\mathcal{B}_\alpha} \mathbf{x} \times \rho^{\alpha} \mathbf{x}^{'}_{\alpha} \mathrm{dv} \tag{3.47}$$

is the moment of momentum,

$$\mathbf{m}^{\alpha}_{(0)} = \int_{\mathcal{B}_\alpha} \mathbf{x} \times \rho^{\alpha} \mathbf{b}^{\alpha} \mathrm{dv} + \int_{\partial\mathcal{B}_\alpha} \mathbf{x} \times \mathbf{T}^{\alpha} \mathbf{da} \tag{3.48}$$

is the moment of external forces and

$$\hat{\mathbf{h}}^{\alpha}_{(0)} = \int_{\mathcal{B}_\alpha} \mathbf{x} \times \hat{\mathbf{p}}^{\alpha} \mathrm{dv} \tag{3.49}$$

is the moment from interaction forces.

Polar materials with an additional rotational degree of freedom need an additional internal moment. These types of materials or effects will not be considered.

From the material time derivative of the moment of momentum

$$(\mathbf{h}^{\alpha}_{(0)})^{'}_{\alpha} = \int_{\mathcal{B}_\alpha} \mathbf{x} \times (\rho^{\alpha} \mathbf{x}^{''}_{\alpha} + \hat{\rho}^{\alpha} \mathbf{x}^{'}_{\alpha}) \mathrm{dv} \tag{3.50}$$

and by applying the divergence theorem

$$\int_{\partial\mathcal{B}_\alpha} \mathbf{x} \times \mathbf{T}^{\alpha} \mathbf{n} \mathrm{da} = \int_{\mathcal{B}_\alpha} (\mathbf{x} \times \mathrm{div}\mathbf{T}^{\alpha} + \mathbf{1} \times \mathbf{T}^{\alpha}) \mathrm{dv} \tag{3.51}$$

the balance equation of the moment of momentum (3.46) yields

$$\int_{\mathcal{B}_\alpha} \mathbf{x} \times (\rho^{\alpha} \mathbf{x}^{''}_{\alpha} + \hat{\rho}^{\alpha} \mathbf{x}^{'}_{\alpha}) = \int_{\mathcal{B}_\alpha} [\mathbf{x} \times (\mathrm{div}\mathbf{T}^{\alpha} + \rho^{\alpha} \mathbf{b}^{\alpha}) + \mathbf{1} \times \mathbf{T}^{\alpha}] \mathrm{dv} + \int_{\mathcal{B}_\alpha} \mathbf{x} \times \hat{\mathbf{p}}^{\alpha} \mathrm{dv} \tag{3.52}$$

or in local form,

$$\mathbf{x} \times [\mathrm{div}\mathbf{T}^{\alpha} + \rho^{\alpha} (\mathbf{b}^{\alpha} - \mathbf{x}^{''}_{\alpha}) + \hat{\mathbf{p}}^{\alpha} - \hat{\rho}^{\alpha} \mathbf{x}^{'}_{\alpha}] + \mathbf{1} \times \mathbf{T}^{\alpha} = \mathbf{0}. \tag{3.53}$$

Considering the local form of the balance of momentum (3.43), the local form of the moment of momentum (3.53) becomes

$$\mathbf{1} \times \mathbf{T}^{\alpha} = \mathbf{0}. \tag{3.54}$$

Providing the partial *Cauchy* stress tensor is symmetric,

$$\mathbf{T}^{\alpha} = (\mathbf{T}^{\alpha})^{\mathrm{T}}. \tag{3.55}$$

### 3.4.4 Balance of energy

The balance of energy describes the energy conservation in porous solids. Coupling of thermal fields (temperature, heat flux and internal heat supply) with mechanical fields (motion, velocity, acceleration, deformation and velocity of deformation) make the balance equations of energy extremely important. In a one component material, the sum of the material time derivatives of the internal and kinetic energies equals the rates of mechanical work and heat and the energy supply $\hat{e}^\alpha$. This yields the balance equation of energy,

$$(\mathrm{E}^\alpha)'_\alpha + (\mathrm{K}^\alpha)'_\alpha = \mathrm{W}^\alpha + \mathrm{Q}^\alpha + \int_{\mathcal{B}_\alpha} \hat{\mathrm{e}}^\alpha \mathrm{dv} \tag{3.56}$$

where

$$\mathrm{E}^\alpha = \int_{\mathcal{B}_\alpha} \rho^\alpha \epsilon^\alpha \mathrm{dv} \tag{3.57}$$

is the internal energy with the specific internal energy $\epsilon^\alpha$ of $\varphi^\alpha$ and

$$\mathrm{K}^\alpha = \int_{\mathcal{B}_\alpha} \frac{1}{2} \rho^\alpha \mathbf{x}'_\alpha \cdot \mathbf{x}'_\alpha \mathrm{dv} \tag{3.58}$$

is the kinetic energy.

$$\mathrm{W}^\alpha = \int_{\mathcal{B}_\alpha} \mathbf{x}'_\alpha \cdot \rho^\alpha \mathbf{b}^\alpha \mathrm{dv} + \int_{\partial\mathcal{B}_\alpha} \mathbf{x}'_\alpha \cdot \mathbf{T}^\alpha \mathbf{da} \tag{3.59}$$

is the increment of mechanical work. The increment of non-mechanical work/rate of heat with the partial energy source $r^\alpha = r^\alpha(\mathbf{x}, t)$ and the partial heat flux vector, $\mathbf{q}^\alpha = \mathbf{q}^\alpha(\mathbf{x}, t)$ ($\mathbf{q}^\alpha$ is positive when entering a body) is

$$\mathrm{Q}^\alpha = \int_{\mathcal{B}_\alpha} \rho^\alpha \mathrm{r}^\alpha \mathrm{dv} - \int_{\partial\mathcal{B}_\alpha} \mathbf{q}^\alpha \cdot \mathbf{da}. \tag{3.60}$$

$\hat{e}^\alpha$ is the local energy supply of the constituents $\varphi^\alpha$ which is caused by the other $\kappa - 1$ constituents. Using the material time derivatives

$$(\mathrm{E}^\alpha)'_\alpha = \int_{\mathcal{B}_\alpha} [\rho^\alpha (\epsilon^\alpha)'_\alpha + \hat{\rho}^\alpha \epsilon^\alpha] \mathrm{dv} \qquad (\mathrm{K}^\alpha)'_\alpha = \int_{\mathcal{B}_\alpha} (\rho^\alpha \mathbf{x}''_\alpha + \frac{1}{2} \hat{\rho}^\alpha \mathbf{x}'_\alpha) \cdot \mathbf{x}'_\alpha \mathrm{dv} \tag{3.61}$$

and the relations

$$\int_{\partial\mathcal{B}_\alpha} \mathbf{x}'_\alpha \cdot \mathbf{T}^\alpha \mathbf{n} \mathrm{da} = \int_{\mathcal{B}_\alpha} (\mathrm{div}\mathbf{T}^\alpha \cdot \mathbf{x}'_\alpha + \mathbf{T}^\alpha : \mathbf{L}_\alpha) \mathrm{dv} \qquad \int_{\partial\mathcal{B}_\alpha} \mathbf{q}^\alpha \cdot \mathbf{n} \mathrm{da} = \int_{\mathcal{B}_\alpha} \mathrm{div}\mathbf{q}^\alpha \mathrm{dv}, \tag{3.62}$$

the balance of energy (3.56) can be transformed to

$$\begin{aligned} &\int_{\mathcal{B}_\alpha} [\rho^\alpha (\epsilon^\alpha)'_\alpha + \hat{\rho}^\alpha \epsilon^\alpha] \mathrm{dv} + \int_{\mathcal{B}_\alpha} (\rho^\alpha \mathbf{x}''_\alpha + \frac{1}{2} \rho^\alpha \mathbf{x}'_\alpha) \cdot \mathbf{x}'_\alpha \mathrm{dv} = \\ &\int_{\mathcal{B}_\alpha} [(\mathrm{div}\mathbf{T}^\alpha + \rho^\alpha \mathbf{b}^\alpha) \cdot \mathbf{x}'_\alpha + \mathbf{T}^\alpha : \mathbf{L}_\alpha] \mathrm{dv} + \int_{\mathcal{B}_\alpha} (\rho^\alpha \mathrm{r}^\alpha - \mathrm{div}\mathbf{q}^\alpha) \mathrm{dv} + \int_{\mathcal{B}_\alpha} \hat{\mathrm{e}}^\alpha \mathrm{dv} \end{aligned} \tag{3.63}$$

or in local form

$$\rho^{\alpha}(\epsilon^{\alpha})^{'}_{\alpha} + \hat{\rho}^{\alpha}(\epsilon^{\alpha} + \frac{1}{2}\mathbf{x}^{'}_{\alpha} \cdot \mathbf{x}^{'}_{\alpha}) = [\mathrm{div}\mathbf{T}^{\alpha} + \rho^{\alpha}(\mathbf{b}^{\alpha} - \mathbf{x}^{''}_{\alpha})] \cdot \mathbf{x}^{'}_{\alpha} +$$
$$\mathbf{T}^{\alpha} : \mathbf{L}_{\alpha} + \rho^{\alpha} r^{\alpha} - \mathrm{div}\mathbf{q}^{\alpha} + \hat{\mathrm{e}}^{\alpha}. \tag{3.64}$$

Making use of the local balance of momentum (3.43) and the symmetry of the partial *Cauchy* stress tensor $\mathbf{T}^{\alpha}$ in (3.55) causing the replacement of the spatial velocity gradient $\mathbf{L}_{\alpha}$ by the rate of deformation tensor $\mathbf{D}_{\alpha}$ allows one to obtain the alternative local form of the balance of energy equation

$$\rho^{\alpha}(\epsilon^{\alpha})^{'}_{\alpha} - \mathbf{T}^{\alpha} : \mathbf{D}^{\alpha} - \rho^{\alpha}\mathrm{r}^{\alpha} + \mathrm{div}\mathbf{q}^{\alpha} = \hat{\mathrm{e}}^{\alpha} + \hat{\mathbf{p}}^{\alpha} \cdot \mathbf{x}^{'}_{\alpha} - \hat{\rho}^{\alpha}(\epsilon^{\alpha} + \frac{1}{2}\mathbf{x}^{'}_{\alpha} \cdot \mathbf{x}^{'}_{\alpha}). \tag{3.65}$$

The summation of the alternative local form of balance of energy (3.65) over $\kappa$ constituents yields

$$\sum_{\alpha=1}^{\kappa}[\rho^{\alpha}(\epsilon^{\alpha})^{'}_{\alpha} - \mathbf{T}^{\alpha} : \mathbf{D}^{\alpha} - \rho^{\alpha}\mathrm{r}^{\alpha} + \mathrm{div}\mathbf{q}^{\alpha}] = \sum_{\alpha=1}^{\kappa}[\hat{\mathrm{e}}^{\alpha} - \hat{\mathbf{p}}^{\alpha} \cdot \mathbf{x}^{'}_{\alpha} - \hat{\rho}^{\alpha}(\epsilon^{\alpha} + \frac{1}{2}\mathbf{x}^{'}_{\alpha} \cdot \mathbf{x}^{'}_{\alpha})]. \tag{3.66}$$

The condition

$$\sum_{\alpha=1}^{\kappa}\hat{\mathrm{e}}^{\alpha} = 0 \tag{3.67}$$

for a single component material is sufficient to fulfil *Truesdell's* third metaphysical principle. An alternative for the local form of the balance of energy (3.65) can be obtained using the partial Helmholtz free energy $\psi^{\alpha} = \psi^{\alpha}(\mathbf{x}, t)$:

$$\psi^{\alpha} = \epsilon^{\alpha} - \theta^{\alpha}\eta^{\alpha} \tag{3.68}$$

where $\epsilon^{\alpha}$ is the inner energy and $\eta^{\alpha}$ is the specific entropy. The Helmholtz free energy of the system must be minimised and the material time derivative yields

$$(\psi^{\alpha})^{'}_{\alpha} = (\epsilon^{\alpha})^{'}_{\alpha} - (\theta^{\alpha})^{'}_{\alpha}\eta^{\alpha} - \theta^{\alpha}(\eta^{\alpha})^{'}_{\alpha} \tag{3.69}$$

where $\eta^{\alpha} = \eta^{\alpha}(\mathbf{x}, \mathrm{t})$ and $\theta^{\alpha} = \theta^{\alpha}(\mathbf{x}, \mathrm{t})$ are the partial specific entropy and partial temperature. (3.65) can be transformed to,

$$\rho^{\alpha}[(\psi^{\alpha})^{'}_{\alpha} + (\theta^{\alpha})^{'}_{\alpha}\eta^{\alpha} - \theta^{\alpha}(\eta^{\alpha})^{'}_{\alpha}] - \mathbf{T}^{\alpha} : \mathbf{D}^{\alpha} - \rho^{\alpha}r^{\alpha} + \mathrm{div}\mathbf{q}^{\alpha} =$$
$$\hat{e}^{\alpha} - \hat{\mathbf{p}}^{\alpha} \cdot \mathbf{x}^{'}_{\alpha} - \hat{\rho}^{\alpha}(\psi^{\alpha} + \theta^{\alpha}\eta^{\alpha} - \frac{1}{2}\mathbf{x}^{'}_{\alpha} \cdot \mathbf{x}^{'}_{\alpha}). \tag{3.70}$$

## 3.5 Entropy inequality

To find restrictions for the constitutive equations, the second law of thermodynamics, the entropy principle is used. The entropy inequality governs the direction of energy conversion and is defined as,

$$\sum_{\alpha=1}^{\kappa}(\mathrm{H}^{\alpha})'_{\alpha} \geq \sum_{\alpha=1}^{\kappa}\int_{\mathcal{B}_{\alpha}}(\frac{1}{\theta^{\alpha}}\rho^{\alpha}\mathrm{r}^{\alpha})\mathrm{dv} - \sum_{\alpha=1}^{\kappa}\int_{\partial\mathcal{B}_{\alpha}}\frac{1}{\theta^{\alpha}}\mathbf{q}^{\alpha}\cdot\mathbf{da}. \tag{3.71}$$

for the mixture. The entropy

$$\mathrm{H}^{\alpha} = \int_{\mathcal{B}_{\alpha}}\rho^{\alpha}\eta^{\alpha}\mathrm{dv} \tag{3.72}$$

has been used. The material time derivative of entropy

$$(\mathrm{H}^{\alpha})'_{\alpha} = \int_{\mathcal{B}_{\alpha}}[\rho^{\alpha}(\eta^{\alpha})'_{\alpha} + \hat{\rho}^{\alpha}\eta^{\alpha}]\mathrm{dv} \tag{3.73}$$

which makes use of the local balance of mass (3.31) and the relation

$$\int_{\partial\mathcal{B}_{\alpha}}\frac{1}{\theta^{\alpha}}\mathbf{q}^{\alpha}\cdot\mathbf{da} = \int_{\mathcal{B}_{\alpha}}\mathrm{div}(\frac{1}{\theta^{\alpha}}\mathbf{q}^{\alpha})\mathrm{dv} \tag{3.74}$$

leads to

$$\sum_{\alpha=1}^{\kappa}\int_{\mathcal{B}_{\alpha}}[\rho^{\alpha}(\eta^{\alpha})'_{\alpha} + \hat{\rho}^{\alpha}\eta^{\alpha}]\mathrm{dv} \geq \sum_{\alpha=1}^{\kappa}\int_{\mathcal{B}_{\alpha}}[\frac{1}{\theta^{\alpha}}\rho^{\alpha}\mathrm{r}^{\alpha} - \mathrm{div}(\frac{1}{\theta^{\alpha}}\mathbf{q}^{\alpha})\mathrm{dv}. \tag{3.75}$$

Considering the *Helmholtz* free energy, its derivative, the local balance of energy (3.65) with the following

$$\rho^{\alpha}\mathrm{r}^{\alpha} = -\rho^{\alpha}(\epsilon^{\alpha})'_{\alpha} + \mathbf{T}^{\alpha}:\mathbf{D}^{\alpha} - \mathrm{div}\mathbf{q}^{\alpha} - \hat{\mathrm{e}}^{\alpha} + \hat{\mathbf{p}}^{\alpha}\cdot\mathbf{x}'_{\alpha} + \hat{\rho}^{\alpha}(\epsilon^{\alpha} + \frac{1}{2}\mathbf{x}'_{\alpha}\cdot\mathbf{x}'_{\alpha}) \tag{3.76}$$

and the relation

$$\mathrm{div}(\frac{1}{\theta^{\alpha}}\mathbf{q}^{\alpha}) = -\frac{1}{\theta^{\alpha}}\mathrm{grad}\theta^{\alpha}\cdot\mathbf{q}^{\alpha} + \mathrm{div}\mathbf{q}^{\alpha}, \tag{3.77}$$

the local entropy inequality is given as

$$\sum_{\alpha=1}^{\kappa}\frac{1}{\theta^{\alpha}}\{-\rho^{\alpha}[(\psi^{\alpha})'_{\alpha} + (\theta^{\alpha})'_{\alpha}\eta^{\alpha}] -$$
$$\hat{\rho}^{\alpha}(\psi^{\alpha} - \frac{1}{2}\mathbf{x}'_{\alpha}\cdot\mathbf{x}'_{\alpha}) + \mathbf{T}^{\alpha}:\mathbf{D} - \hat{\mathbf{p}}^{\alpha}\cdot\mathbf{x}'_{\alpha} - \frac{1}{\theta^{\alpha}}\mathbf{q}^{\alpha}\cdot\mathrm{grad}\theta^{\alpha} + \hat{\mathrm{e}}^{\alpha}\} \geq 0. \tag{3.78}$$

The local entropy inequality (3.78) is sufficient to obtain restrictions for the constitutive modelling.

# Chapter 4

# Biphasic material model

It is to be assumed that the porosity of the sea ice sample remains constant over small time-scales but only varies over large scale seasonal temperature variations linked to growth and melt [25]. Accordingly, temperature variations will not by accounted for in the biphasic TPM model and the porosity of the sea ice is not to change. The following assumptions are adopted for the biphasic model of two constituents of solid and fluid phase $\varphi^\alpha, \alpha \in \{\mathrm{S}, \mathrm{F}\}$. A biphasic porous body where both phases are of equal temperature

$$\theta = \theta^{\mathrm{S}} = \theta^{\mathrm{F}}. \tag{4.1}$$

Both phases are assumed incompressible $\rightarrow (\rho^{\mathrm{SR}})'_{\mathrm{S}} = 0$ and $(\rho^{\mathrm{FR}})'_{\mathrm{F}} = 0$ and the material is isothermal

$$(\theta^\alpha)'_\alpha = 0. \tag{4.2}$$

There is no internal energy supply

$$\hat{\mathrm{e}}^{\mathrm{S}} = \hat{\mathrm{e}}^{\mathrm{F}} = 0 \tag{4.3}$$

as it results from a temperature difference between the phases and thus must be zero as there is no temperature difference between the phases as stated in (4.1). The system is quasi-static meaning therefore the acceleration is equal to zero

$$\mathbf{x}''_\alpha = 0 \tag{4.4}$$

and there is no mass supply/exchange

$$\hat{\rho}^\alpha = 0. \tag{4.5}$$

Furthermore model equations such as the saturation condition,

$$\mathrm{n}^{\mathrm{S}} + \mathrm{n}^{\mathrm{F}} = 1, \tag{4.6}$$

the partial densities

$$\mathrm{n}^{\mathrm{S}} = \frac{\rho^{\mathrm{S}}}{\rho^{\mathrm{SR}}}; \qquad \mathrm{n}^{\mathrm{F}} = \frac{\rho^{\mathrm{F}}}{\rho^{\mathrm{FR}}} \tag{4.7}$$

and the interaction forces

$$\hat{\mathbf{p}}^{\mathrm{S}} + \hat{\mathbf{p}}^{\mathrm{F}} = \mathbf{0} \tag{4.8}$$

are to be used as physical constraints. Due to incompressibility of the solid phase, the real desnity $\rho^{SR}$ is

$$\rho^{\mathrm{SR}} = \rho^{\mathrm{SR}}_{0\mathrm{S}} = \mathrm{const} \Rightarrow (\rho^{\mathrm{SR}})'_{\mathrm{S}} = (\rho^{\mathrm{SR}}_{0\mathrm{S}})'_{\mathrm{S}} = 0 \Rightarrow (\rho^{\mathrm{S}})'_{\mathrm{S}} = (\mathrm{n}^{\mathrm{S}})'_{\mathrm{S}} \rho^{\mathrm{SR}}_{0\mathrm{S}} \tag{4.9}$$

and the real density of the fluid phase $\rho^F R$ is

$$\rho^{\mathrm{FR}} = \rho^{\mathrm{FR}}_{0\mathrm{F}} = \mathrm{const} \Rightarrow (\rho^{\mathrm{FR}})'_{\mathrm{F}} = (\rho^{\mathrm{FR}}_{0\mathrm{F}})'_{\mathrm{F}} = 0 \Rightarrow (\rho^{\mathrm{F}})'_{\mathrm{F}} = (\mathrm{n}^{\mathrm{F}})'_{\mathrm{F}} \rho^{\mathrm{FR}}_{0\mathrm{F}} \tag{4.10}$$

## 4.1 Local forms of balance field equations

The balance equations are formulated in local forms for each individual constituent. The interaction effects are taken into consideration. From (3.31), for the constituents $\varphi^S$ and $\varphi^F$, the local balance of mass is given as

$$(\mathrm{n^S})'_{\mathrm{S}} + \mathrm{n^S div}\mathbf{x}'_{\mathrm{S}} = 0 \tag{4.11}$$

and

$$(\mathrm{n^F})'_{\mathrm{F}} + \mathrm{n^F div}\mathbf{x}'_{\mathrm{F}} = 0 \tag{4.12}$$

From (3.54), the local balance of momentum of the solid yields

$$\mathrm{div}\mathbf{T}^{\mathrm{S}} + \mathrm{n^S}\rho^{\mathrm{SR}}\mathbf{b} + \hat{\mathbf{p}}^{\mathrm{S}} = 0 \tag{4.13}$$

and for a fluid

$$\mathrm{div}\mathbf{T}^{\mathrm{F}} + \mathrm{n^F}\rho^{\mathrm{FR}}\mathbf{b} + \hat{\mathbf{p}}^{\mathrm{F}} = 0. \tag{4.14}$$

(3.66) describes the mixture balance of energy equation to describe the thermal behaviour of the body which is

$$\sum_{\alpha}^{SF}[\rho^\alpha(\epsilon^\alpha)'_\alpha - \mathbf{T}^\alpha : \mathbf{D}_\alpha - \rho^\alpha r^\alpha + \mathrm{div}\mathbf{q}^\alpha =$$
$$\sum_{\alpha}^{SF}[\hat{e}^\alpha - \hat{\mathbf{p}}^\alpha \cdot \mathbf{x}'_\alpha = \hat{\rho}^\alpha(\epsilon^\alpha - \frac{1}{2}\mathbf{x}'_\alpha \cdot \mathbf{x}'_\alpha)] \tag{4.15}$$

with internal energy being

$$\epsilon^\alpha = \psi^\alpha + \theta\eta^\alpha. \tag{4.16}$$

## 4.2 Basic constitutive relations

The constitutive quantities of the field equation system are

$$\mathcal{C} = \left\{\mathbf{T}^{\mathrm{S}}, \mathbf{T}^{\mathrm{F}}, \hat{\mathbf{p}}^{\mathrm{S}}\right\}, \tag{4.17}$$

noting either $\hat{\mathbf{p}}^S$ or $\hat{\mathbf{p}}^F$ can be used. The remaining constitutive quantities are

$$\mathcal{P} = \left\{\mathbf{C}_{\mathrm{S}}, \mathbf{w}_{\mathrm{FS}}, \mathrm{gradn^F}\right\} \tag{4.18}$$

where $\mathbf{w}_{FS}$ is the fluid seepage velocity defined as

$$\mathbf{w}_{\mathrm{FS}} = \mathbf{x}'_{\mathrm{F}} - \mathbf{x}'_{\mathrm{S}}. \tag{4.19}$$

Considering the assumptions, we gain the entropy inequality

$$\sum_{\alpha}^{\mathrm{SF}} \frac{1}{\theta}\left\{-\rho^\alpha(\psi^\alpha)'_\alpha + \mathbf{T}^\alpha : \mathbf{D}_\alpha - \hat{\mathbf{p}}^\alpha \mathbf{x}'_\alpha\right\} \geq 0. \tag{4.20}$$

### 4.2.1 Evaluation of the entropy inequality

The evaluation of the entropy inequality is used for the construction of restrictions for the constitutive modelling in order to capture all dependencies which may be included in the model. Additionally to the entropy inequality, the material time derivative of the saturation condition and the balance of mass will be considered.

The material time derivative of the saturation condition (4.6) with respect to the solids motion is

$$(\mathrm{n}^{\mathrm{S}})'_{\mathrm{S}} + (\mathrm{n}^{\mathrm{F}})'_{\mathrm{S}} = 0. \tag{4.21}$$

With $n^\alpha = n^\alpha(\mathbf{x}(\mathbf{X}_\alpha, t), t)$ follows the material time derivative for the solid volume fraction with respect to the solid motion

$$(\mathrm{n}^{\mathrm{S}})'_{\mathrm{S}} = \frac{\partial \mathrm{n}^{\mathrm{S}}}{\partial \mathrm{t}} + \mathrm{gradn}^{\mathrm{S}} \cdot \mathbf{x}'_{\mathrm{S}}, \tag{4.22}$$

and the fluid volume fraction with respect to the fluid motion,

$$(\mathrm{n}^{\mathrm{F}})'_{\mathrm{F}} = \frac{\partial \mathrm{n}^{\mathrm{F}}}{\partial \mathrm{t}} + \mathrm{gradn}^{\mathrm{F}} \cdot \mathbf{x}'_{\mathrm{F}} \tag{4.23}$$

Additionally, the material time derivative of the fluid volume fraction with respect to the solid motion yields

$$\begin{aligned}
(\mathrm{n}^{\mathrm{F}})'_{\mathrm{S}} &= \frac{\partial \mathrm{n}^{\mathrm{F}}}{\partial \mathrm{t}} + \mathrm{gradn}^{\mathrm{F}} \cdot \mathbf{x}'_{\mathrm{S}} \\
(\mathrm{n}^{\mathrm{F}})'_{\mathrm{S}} &= (\mathrm{n}^{\mathrm{F}})'_{\mathrm{F}} - \mathrm{gradn}^{\mathrm{F}} \cdot \mathbf{x}'_{\mathrm{F}} + \mathrm{gradn}^{\mathrm{F}} \cdot \mathbf{x}'_{\mathrm{S}} \\
(\mathrm{n}^{\mathrm{F}})'_{\mathrm{S}} &= (\mathrm{n}^{\mathrm{F}})'_{\mathrm{F}} - \mathrm{gradn}^{\mathrm{F}} \cdot (\mathbf{x}'_{\mathrm{F}} - \mathbf{x}'_{\mathrm{S}}) \\
(\mathrm{n}^{\mathrm{F}})'_{\mathrm{S}} &= (\mathrm{n}^{\mathrm{F}})'_{\mathrm{F}} - \mathrm{gradn}^{\mathrm{F}} \cdot \mathbf{w}_{\mathrm{FS}}
\end{aligned} \tag{4.24}$$

where $\mathbf{w}_{FS}$ is as defined in (4.19). From (4.24), the material time derivative of the saturation condition is

$$(\mathrm{n}^{\mathrm{S}})'_{\mathrm{S}} + (\mathrm{n}^{\mathrm{F}})'_{\mathrm{F}} - \mathrm{gradn}^{\mathrm{F}} \cdot \mathbf{w}_{\mathrm{FS}} = 0. \tag{4.25}$$

The volume balance of mass is given as

$$(\mathrm{n}^{\alpha})'_{\alpha} + \mathrm{n}^{\alpha}\mathrm{div}\mathbf{x}'_{\alpha} = 0 \tag{4.26}$$

where $\mathrm{div}\mathbf{x}'_{\alpha} = \mathrm{grad}\mathbf{x}'_{\alpha} \cdot \mathbf{1} = \mathbf{L}_{\alpha} \cdot \mathbf{1} = \mathbf{D}_{\alpha} \cdot \mathbf{1}$.

(4.26) then becomes

$$(\mathrm{n}^{\alpha})'_{\alpha} = -\mathrm{n}^{\alpha}\mathbf{D}_{\alpha} : \mathbf{1}. \tag{4.27}$$

By substituting (4.25) into (4.26) we yield

$$\mathrm{n^S}\mathbf{D}_\mathrm{S} : \mathbf{1} + \mathrm{n^F}\mathbf{D}_\mathrm{F} : \mathbf{1} + \mathrm{gradn^F}\mathbf{w}_\mathrm{FS} = 0 \tag{4.28}$$

The multiplication of (4.28) with the Lagrange multiplier $\lambda$ yields the constraint

$$\frac{1}{\theta}\lambda\left\{\mathrm{n^S}\mathbf{D}_\mathrm{S} : \mathbf{1} + \mathrm{n^F}\mathbf{D}_\mathrm{F} : \mathbf{1} + \mathrm{gradn^F}\mathbf{w}_\mathrm{FS}\right\} = 0. \tag{4.29}$$

which will be added to the entropy (4.20) of the mixture yielding

$$\begin{aligned}&\frac{1}{\theta}[-\rho^S(\psi^S)'_S - \rho^F(\psi^F)'_F + \mathbf{D}_S : [\mathbf{T}^S + n^S\lambda\mathbf{1}] + \mathbf{D}_F : [\mathbf{T}^F + \mathrm{n^F}\lambda\mathbf{1}]\\ &- \hat{\mathbf{p}}^S \cdot \mathbf{x}'_S - \hat{\mathbf{p}}^F \cdot \mathbf{x}'_F + \lambda\mathrm{gradn^F} \cdot \mathbf{w}_\mathrm{FS}] \geq 0\end{aligned} \tag{4.30}$$

where the relation $\hat{\mathbf{p}}^S = -\hat{\mathbf{p}}^F$ is to be considered. The inequality (4.30) represents the entropy inequality of the biphasic porous medium based on all aforementioned assumptions and constraints.

The assumptions for the restriction of the *Helmholtz* free energy functions for the solid and fluid phases are

$$\psi^\mathrm{S} = \psi^\mathrm{S}(\mathbf{C}_\mathrm{S}) \qquad \text{and} \qquad \psi^\mathrm{F} = \psi^\mathrm{F}(-) \tag{4.31}$$

[21] respectively.

To evaluate the local form of the entropy inequality (3.78), terms for $(\psi^S)'_S$ and $(\psi^F)'_F$ need to be included.

The derivation of the *Helmholtz* free energy function with respect to $\mathbf{C}_S$ is

$$(\psi^\mathrm{S})'_\mathrm{S} = \frac{\partial\psi^\mathrm{S}}{\partial\mathbf{C}_\mathrm{S}} \cdot (\mathbf{C}_\mathrm{S})'_\mathrm{S} \tag{4.32}$$

The relation

$$(\mathbf{C}_\mathrm{S})'_\mathrm{S} = 2\mathbf{F}^\mathrm{T}_\mathrm{S}\mathbf{D}_\mathrm{S}\mathbf{F}_\mathrm{S} \tag{4.33}$$

along with (4.33) yields the *Helmholtz* free energy function with respect to $\mathbf{C}_S$

$$(\psi^S)'_S = 2\mathbf{F}_S\frac{\partial\psi^S}{\partial\mathbf{C}_S}\mathbf{F}^T_S : \mathbf{D}_S \tag{4.34}$$

$$(\psi^F)'_F = 0. \tag{4.35}$$

The final entropy inequality is obtained by including the relation in (4.34) and is

$$\begin{aligned}&\mathbf{D}_S : [\mathbf{T}^S + n^S\lambda\mathbf{1} - 2\mathbf{F}_S\frac{\partial\psi^S}{\partial\mathbf{C}_S}\mathbf{F}^T_S]+\\ &\mathbf{D}_F : [\mathbf{T}^F + n^F\lambda\mathbf{1}] + \mathbf{w}_{FS} \cdot [-\hat{\mathbf{p}}^F + \lambda\mathrm{gradn^F}] \geq 0\end{aligned} \tag{4.36}$$

### 4.2.2 Stress

The *Cauchy* stress tensor for the solid phase depends on the derivative of $\psi_s$ with respect to the deformation. The deformation is represented through the right *Cauchy* green tensor $\mathbf{C}_s$. From (4.36) an by making use of standard thermodynamic arguments, the solid stress yields

$$\mathbf{T}^{\mathrm{S}} = -\mathrm{n}^{\mathrm{S}}\lambda\mathbf{1} + 2\mathbf{F}_{\mathrm{S}}\frac{\partial\psi^{\mathrm{S}}}{\partial\mathbf{C}_{\mathrm{S}}}\mathbf{F}_{\mathrm{S}}^{\mathrm{T}} \tag{4.37}$$

where $2\mathbf{F}_{\mathrm{S}}\frac{\partial\psi^{\mathrm{S}}}{\partial\mathbf{C}_{\mathrm{S}}}\mathbf{F}_{\mathrm{S}}^{\mathrm{T}} = \mathbf{T}_{\mathrm{E}}^{\mathrm{S}}$ is the effective *Cauchy* stress tensor. The fluid stress yields

$$\mathbf{T}^{\mathrm{F}} = -\mathrm{n}^{\mathrm{F}}\lambda\mathbf{1} \tag{4.38}$$

where $\lambda$ is the pore pressure, an indeterminate reaction force with an unknown quantity that must be additionally solved. The total stress is the sum of the partial stresses while considering the saturation condition which yields

$$\begin{aligned}
\mathbf{T} &= \mathbf{T}^{\mathrm{S}} + \mathbf{T}^{\mathrm{F}} \\
\mathbf{T} &= -\lambda\mathbf{1} + \mathbf{T}_{\mathrm{E}}^{\mathrm{S}} \\
\mathbf{T} &= \frac{1}{J_S}[2\mu\mathbf{k}_S + (\lambda^S \ln J_S + J_S\lambda)\mathbf{1}] \\
\mathbf{T} &= \frac{1}{J_S}\mathbf{F}\mathbf{S}\mathbf{F}^T
\end{aligned} \tag{4.39}$$

where $\mu^S$ and $\lambda^S$ are the *Lamé* parameters and $\mathbf{S}$ is the second Piola Kirrchoff stress tensor defined as

$$\mathbf{S} = \mathrm{J}_{\mathrm{S}}\mathbf{F}_{\mathrm{S}}^{-1}\mathbf{T}\mathbf{F}_{\mathrm{S}}^{-\mathrm{T}} \qquad \text{and} \qquad \mathbf{S} = \mathbf{S}_{\mathrm{E}}^{\mathrm{S}} - \mathrm{J}_{\mathrm{S}}\lambda\mathbf{C}_{\mathrm{S}}^{-1} \tag{4.40}$$

Then making use of linear elastic material behaviour, the effective second Piola Kirchhoff stress tensor is given by

$$\mathbf{S}_{\mathrm{E}}^{\mathrm{S}} = 2\frac{\partial\psi(\mathbf{C}_{\mathrm{S}})}{\partial\mathbf{C}_{\mathrm{S}}} \tag{4.41}$$

with the Neo-Hookean strain energy density function

$$\psi(\mathbf{C}_{\mathrm{S}}) = \frac{\mu}{2}(\mathbf{C}_{\mathrm{S}} : \mathbf{1} - 3) - \mu\mathrm{ln}\mathrm{J}_{\mathrm{S}} + \frac{\lambda}{2}(\mathrm{ln}\mathrm{J}_{\mathrm{S}})^2. \tag{4.42}$$

The first Piola Kirrchoff stress tensor is defined as

$$\mathbf{P} = \mathbf{F}_{\mathrm{S}}\mathbf{S}. \tag{4.43}$$

### 4.2.3 Seepage velocity

The motion of the fluid in a porous solid is calculated relative to the motion of the solid. This is done through the seepage velocity $\mathbf{w}_{\mathrm{FS}} = \mathbf{x}_{\mathrm{F}}^{'} - \mathbf{x}_{\mathrm{S}}^{'}$. The reduced dissipation inequality is

$$\mathcal{D} = \mathbf{w}_{\mathrm{FS}} \cdot (-\hat{\mathbf{p}}^{\mathrm{F}} + \lambda \mathrm{gradn}^{\mathrm{F}}) \geq 0 \tag{4.44}$$

The dissipation is fulfilled with

$$-(-\hat{\mathbf{p}}^{\mathrm{F}} + \lambda \mathrm{gradn}^{\mathrm{F}}) = \alpha_{\mathrm{FS}} \mathbf{w}_{\mathrm{FS}} \tag{4.45}$$

where $\alpha_{\mathbf{w}_{\mathrm{FS}}} \geq 0$ is a material parameter linked to the permeability. The local balance of momentum (4.14) with the relation given in (4.38), the balance of momentum becomes

$$\mathrm{div}(-\mathrm{n}^{\mathrm{F}} \lambda \mathbf{1}) = -\mathrm{n}^{\mathrm{F}} \mathrm{grad}\lambda + \rho^{\mathrm{F}} \mathbf{b} - \alpha_{\mathrm{FS}} \mathbf{w}_{\mathrm{FS}} \tag{4.46}$$

If the relation $\rho^{\mathrm{F}} = \mathrm{n}^{\mathrm{F}} \rho^{\mathrm{FR}}$ we obtain the seepage velocity

$$\mathrm{n}^{\mathrm{F}} \mathbf{w}_{\mathrm{FS}} = \frac{(\mathrm{n}^{\mathrm{F}})^2}{\alpha_{\mathrm{FS}}} [-\mathrm{grad}\lambda + \rho^{\mathrm{FR}} \mathbf{b}] \tag{4.47}$$

The determination of the physical parameter $\alpha_{FS}$ can be done two ways [35]. The first is

$$\frac{(\mathrm{n}^{\mathrm{F}})^2}{\alpha_{\mathrm{FS}}} = \frac{\mathrm{K}^{\mathrm{S}}_{0\mathrm{S}}}{\mu^{\mathrm{FR}}} [\frac{\mathrm{n}^{\mathrm{F}}}{\mathrm{n}^{\mathrm{F}}_{0\mathrm{S}}}]^{\mathrm{m}} \tag{4.48}$$

where $\mathrm{K}^{\mathrm{S}}_{0\mathrm{S}}$ refers to the intrinsic permeability of the material, $\mu^{\mathrm{FR}}$refers to the dynamic viscosity of the fluid, $\frac{\mathrm{n}^{\mathrm{F}}}{\mathrm{n}^{\mathrm{F}}_{0\mathrm{S}}}$ is the actual reference pore volume and where m is a parameter for the change in permeability due to deformation with $\mathrm{m} = 1$ being a linear dependence. The second way of determining $\alpha_{\mathrm{FS}}$ is

$$\frac{(\mathrm{n}^{\mathrm{F}})^2}{\alpha_{\mathrm{FS}}} = \frac{\mathrm{K}^{\mathrm{F}}_{0\mathrm{S}}}{\gamma^{\mathrm{FR}}} [\frac{\mathrm{n}^{\mathrm{F}}}{\mathrm{n}^{\mathrm{F}}_{0\mathrm{S}}}]^{\mathrm{m}} \tag{4.49}$$

where $\mathrm{K}^{\mathrm{F}}_{0\mathrm{S}}$ is the Darcy permeability and $\gamma^{\mathrm{FR}} = \rho^{\mathrm{FR}} \mathbf{b}$ is the bulk density. An expression for the seepage velocity is the

$$\mathrm{n}^{\mathrm{F}} \mathbf{w}_{\mathrm{FS}} = \alpha_{\mathrm{F}} [\frac{\mathrm{n}^{\mathrm{F}}}{\mathrm{n}^{\mathrm{F}}_{0\mathrm{S}}}]^{\mathrm{m}} [-\mathrm{grad}\lambda + \rho^{\mathrm{FR}} \mathbf{b}] \tag{4.50}$$

with $\alpha_{\mathrm{F}} = \frac{\mathrm{K}^{\mathrm{S}}_{0\mathrm{S}}}{\mu^{\mathrm{FR}}}$ or $\alpha_{\mathrm{F}} = \frac{\mathrm{K}^{\mathrm{F}}_{0\mathrm{S}}}{\gamma^{\mathrm{FR}}}$.

## 4.3 Weak forms for biphasic model

In this section the weak forms for the balance of momentum and balance of mass for the mixture of the biphasic model are described based on the constitutive relations and balance equations.

### 4.3.1 Weak form of the momentum balance

Considering the balance of momentum (3.44) along with the local balance of momentum of the solid (4.13), and the fluid (4.14) the following can be obtained

$$\mathrm{div}(\mathbf{T}^{\mathrm{S}} + \mathbf{T}^{\mathrm{F}}) + (\rho^{\mathrm{S}} + \rho^{\mathrm{F}})\mathbf{b} + \hat{\mathbf{p}}^{\mathrm{S}} + \hat{\mathbf{p}}^{\mathrm{F}} = 0. \tag{4.51}$$

Considering the equation for the balance of momentum (3.43), along with (4.37), (4.38) and the saturation condition $\mathrm{n}^{\mathrm{S}} + \mathrm{n}^{\mathrm{F}} = 1$ we achieve the following

$$\mathrm{div}(-\lambda\mathbf{1} + \mathbf{T}_{\mathrm{E}}^{\mathrm{S}}) + (\rho^{\mathrm{S}} + \rho^{\mathrm{F}})\mathbf{b} = 0 \tag{4.52}$$

which along with (4.39) yields

$$\mathrm{div}(\mathbf{T}) + (\rho^{\mathrm{S}} + \rho^{\mathrm{F}})\mathbf{b} = 0. \tag{4.53}$$

Under the condition for the stress in (4.39) and

$$\overset{+}{\mathbf{F}}_{\mathrm{S}} = \mathbf{F}_{\mathrm{S}}^{-\mathrm{T}}\mathrm{J}_{\mathrm{S}} \tag{4.54}$$

and the transport theorem

$$\mathrm{d}\mathbf{a} = \overset{+}{\mathbf{F}}_{\mathrm{S}}\mathrm{d}\mathbf{A}_{0\mathrm{S}} = \mathrm{J}_{\mathrm{S}}^{-}\mathbf{F}_{\mathrm{S}}^{-\mathrm{T}}\mathrm{d}\mathrm{A}_{0\mathrm{S}} \qquad \text{and} \qquad \mathrm{d}\mathrm{v} = \mathrm{J}_{\mathrm{S}}\mathrm{d}\mathrm{V}_{0\mathrm{S}} \tag{4.55}$$

the mapping of (4.53) to the reference configuration yields

$$\int_{\mathcal{B}_{\mathrm{S}}} \mathrm{div}\mathbf{T} + (\rho^{\mathrm{S}} + \rho^{\mathrm{F}})\mathbf{b}\mathrm{d}\mathrm{v} = 0. \tag{4.56}$$

Applying the transport theorem yields the global form of the balance of momentum which is

$$\int_{\mathcal{B}_{0\mathrm{S}}} \mathrm{div}\mathbf{P} + (\rho^{\mathrm{S}} + \rho^{\mathrm{F}})\mathrm{J}_{\mathrm{S}}\mathbf{b}\mathrm{d}\mathrm{V}_{0\mathrm{S}} = 0. \tag{4.57}$$

The global form of the balance of momentum is multiplied by an arbitrary test function $\delta\mathbf{u}_{\mathrm{S}}$

$$\int_{\mathcal{B}_{0\mathrm{S}}} [\mathrm{div}\mathbf{P} \cdot \delta\mathbf{u}_{\mathrm{S}} + (\rho^{\mathrm{S}} + \rho^{\mathrm{F}})\mathrm{J}_{\mathrm{S}}\mathbf{b} \cdot \delta\mathbf{u}_{\mathrm{S}}]\mathrm{d}\mathrm{V}_{0\mathrm{S}} = 0 \tag{4.58}$$

to solve for the solid displacement $\mathbf{u}_{\mathrm{S}}$. The use of *Gauss's* divergence theorem yields the corresponding weak form

$$\begin{aligned}
&\int_{\mathcal{B}_{0\mathrm{S}}} \mathbf{P} \cdot \mathrm{Grad}(\delta\mathbf{u}_{\mathrm{S}})\mathrm{d}\mathrm{V}_{0\mathrm{S}} - \int_{\mathcal{B}_{0\mathrm{S}}} (\mathrm{n}^{\mathrm{S}}\rho^{\mathrm{SR}} + \mathrm{n}^{\mathrm{F}}\rho^{\mathrm{FR}})\mathrm{J}_{\mathrm{S}}\mathbf{b} \cdot \delta\mathbf{u}_{\mathrm{S}}\mathrm{d}\mathrm{V}_{0\mathrm{S}} - \int_{\mathcal{B}_{0\mathrm{S}}} \mathrm{Div}(\mathbf{P}^{\mathrm{T}}\delta\mathbf{u}_{\mathrm{S}})\mathrm{d}\mathrm{V}_{0\mathrm{S}} \\
&= \int_{\mathcal{B}_{0\mathrm{S}}} \mathbf{P} \cdot \mathrm{Grad}(\delta\mathbf{u}_{\mathrm{S}})\mathrm{d}\mathrm{V}_{0\mathrm{S}} - \int_{\mathcal{B}_{0\mathrm{S}}} (\mathrm{n}^{\mathrm{S}}\rho^{\mathrm{SR}} + \mathrm{n}^{\mathrm{F}}\rho^{\mathrm{FR}})\mathrm{J}_{\mathrm{S}}\mathbf{b} \cdot \delta\mathbf{u}_{\mathrm{S}}\mathrm{d}\mathrm{V}_{0\mathrm{S}} - \int_{\partial\mathcal{B}_{0\mathrm{S}}} \mathbf{P}\mathbf{n}_{0\mathrm{S}}\mathrm{d}\mathrm{A}_{0\mathrm{S}} = 0.
\end{aligned} \tag{4.59}$$

The stress in terms of the second *Piola-Kirchhoff* stress yields

$$\mathrm{G}_{\mathrm{mom}}^{\mathrm{mix}} = \int_{\mathcal{B}_{0\mathrm{S}}} \mathbf{S} \cdot \delta\mathbf{E}_{\mathrm{S}}\mathrm{d}\mathrm{V}_{0\mathrm{S}} - \int_{\mathcal{B}_{0\mathrm{S}}} (\mathrm{n}^{\mathrm{S}}\rho^{\mathrm{SR}} + \mathrm{n}^{\mathrm{F}}\rho^{\mathrm{FR}})\mathrm{J}_{\mathrm{S}}\mathbf{b} \cdot \delta\mathbf{u}_{\mathrm{S}}\mathrm{d}\mathrm{V}_{0\mathrm{S}} - \int_{\partial\mathcal{B}_{0\mathrm{S}}} \mathbf{t}_0 \cdot \delta\mathbf{u}_{\mathrm{S}}\mathrm{d}\mathrm{A}_{0\mathrm{S}} = 0. \tag{4.60}$$

where the traction vector $\mathbf{t}_0$ in the reference configuration is $\mathbf{t}_0 = \mathbf{t}_{\mathrm{S}0} + \mathbf{t}_{\mathrm{F}0} = \mathbf{P}\mathbf{n}_{0\mathrm{S}}$. The final balance of momentum equation in the reference configuration expressed in terms of the right *Cauchy-Green* deformation tensor which is sufficient to solve the displacement solid $\mathbf{u}_{\mathrm{S}}$

$$\mathrm{G}_{\mathrm{mom}}^{\mathrm{mix}} = \int_{\mathcal{B}_{0\mathrm{S}}} \frac{1}{2}\mathbf{S} \cdot \delta\mathbf{C}_{\mathrm{S}}\mathrm{d}\mathrm{V}_{0\mathrm{S}} - \int_{\mathcal{B}_{0\mathrm{S}}} (\mathrm{n}^{\mathrm{S}}\rho^{\mathrm{SR}} + \mathrm{n}^{\mathrm{F}}\rho^{\mathrm{FR}})\mathrm{J}_{\mathrm{S}}\mathbf{b} \cdot \delta\mathbf{u}_{\mathrm{S}}\mathrm{d}\mathrm{V}_{0\mathrm{S}} - \int_{\partial\mathcal{B}_{0\mathrm{S}}} \mathbf{t}_0 \cdot \delta\mathbf{u}_{\mathrm{S}}\mathrm{d}\mathrm{A}_{0\mathrm{S}} = 0. \tag{4.61}$$

### 4.3.2 Weak form of the balance of mass of mixture

The additional unknown displacement field, the *Lagrange* multiplier $\lambda$ exists in the system of equations. Combining (4.11) and (4.12) and presenting the result in integral form yields

$$\int_{\mathcal{B}_S} \left\{ (\mathrm{n}^S)'_S + (\mathrm{n}^F)'_F + \mathrm{n}^S \mathrm{div}\mathbf{x}'_S + \mathrm{n}^F \mathrm{div}\mathbf{x}'_F \right\} \mathrm{dv} = 0. \tag{4.62}$$

Recall the relation $(\mathrm{n}^F)'_F = (\mathrm{n}^F)'_S + \mathrm{gradn}^F \cdot \mathbf{w}_{FS}$ and $(\mathrm{n}^S)'_S + (\mathrm{n}^F)'_S = 0$ yields

$$\int_{\mathcal{B}_S} \left\{ \mathrm{gradn}^F \cdot \mathbf{w}_{FS} + \mathrm{n}^S \mathrm{div}\mathbf{x}'_S + \mathrm{n}^F \mathrm{div}\mathbf{x}'_F \right\} \mathrm{dv} = 0. \tag{4.63}$$

The relation

$$\mathrm{div}(\mathrm{n}^F \mathbf{w}_{FS}) = \mathrm{grad}(\mathrm{n}^F) \cdot \mathbf{w}_{FS} + \mathrm{n}^F \mathrm{div}(\mathbf{x}'_F) - \mathrm{n}^F \mathrm{div}(\mathbf{x}'_S) \tag{4.64}$$

which, once rearranged yields

$$\mathrm{grad}(\mathrm{n}^F) \cdot \mathbf{w}_{FS} = \mathrm{div}(\mathrm{n}^F \mathbf{w}_{FS}) - \mathrm{n}^F \mathrm{div}(\mathbf{x}'_F) + \mathrm{n}^F \mathrm{div}(\mathbf{x}'_S). \tag{4.65}$$

Applying the relation in (4.65) to (4.63) yields the strong form of the balance of mass of the mixture

$$\int_{\mathcal{B}_S} \left\{ \mathrm{div}(\mathrm{n}^F \mathbf{w}_{FS}) + \mathrm{div}\mathbf{x}'_S \right\} \mathrm{dv} = 0. \tag{4.66}$$

By making use of *Greens's* theorem yields

$$\int_{\partial\mathcal{B}_S} (\mathbf{x}'_S + \mathrm{n}^F \mathbf{w}_{FS}) \mathrm{d}\mathbf{a} = 0. \tag{4.67}$$

Applying the transport theorem (4.55) maps the balance of mass to the reference configuration as

$$\int_{\partial\mathcal{B}_{0S}} (\mathbf{x}'_S + \mathrm{n}^F \mathbf{w}_{FS}) \overset{+}{\mathbf{F}}_S \mathrm{d}\mathbf{A}_{0S} = 0. \tag{4.68}$$

The balance equation of mass in the reference configuration follows the relation

$$\int_{\mathcal{B}} \mathrm{div}\mathbf{v} \mathrm{dv} = \int_{\partial\mathcal{B}} \mathbf{v} \mathrm{d}\mathbf{a} = \int_{\partial\mathcal{B}_0} \mathbf{v} \overset{+}{\mathbf{F}}_S \mathrm{d}\mathbf{A}_{0S} = \int_{\partial\mathcal{B}_0} \mathrm{J}\mathbf{v}\mathbf{F}_S^{-\mathrm{T}} \mathrm{d}\mathbf{A}_{0S} = \int_{\mathcal{B}_0} \mathrm{Div}(\mathrm{J}_S \mathbf{v}\mathbf{F}_S^{-\mathrm{T}}) \mathrm{dV}_{0S} \tag{4.69}$$

yielding

$$\int_{\mathcal{B}} \mathrm{div}(\mathbf{x}'_S + \mathrm{n}^F \mathbf{w}_{FS}) \mathrm{dv} = \int_{\partial\mathcal{B}} (\mathbf{x}'_S + \mathrm{n}^F \mathbf{w}_{FS}) \mathrm{d}\mathbf{a} = \int_{\partial\mathcal{B}_0} (\mathbf{x}'_S + \mathrm{n}^F \mathbf{w}_{FS}) \overset{+}{\mathbf{F}}_S \mathrm{d}\mathbf{A}_{0S} =$$
$$\int_{\partial\mathcal{B}_0} \mathrm{J}(\mathbf{x}'_S + \mathrm{n}^F \mathbf{w}_{FS}) \mathbf{F}_S^{-\mathrm{T}} \mathrm{d}\mathbf{A}_{0S} = \int_{\mathcal{B}_0} \mathrm{Div}(\mathrm{J}_S (\mathbf{x}'_S + \mathrm{n}^F \mathbf{w}_{FS}) \mathbf{F}_S^{-\mathrm{T}}) \mathrm{dV}_{0S} \tag{4.70}$$

By multiplying (4.70) by an arbitrary test function $\delta\lambda$ yields

$$\int_{\mathcal{B}_0} \left\{ \mathrm{Div}(\mathrm{J_S n^F \mathbf{w}_{FS} \mathbf{F}_S^{-T}}) + \mathrm{Div}(\mathrm{J_S \mathbf{x}_S' \mathbf{F}_S^{-T}}) \right\} \delta\lambda \mathrm{dV_{0S}} =$$
$$\int_{\mathcal{B}_0} \left\{ \mathrm{Div}(\mathrm{J_S n^F \mathbf{w}_{FS} \mathbf{F}_S^{-T}} + \mathrm{J_S \mathbf{x}_S' \mathbf{F}_S^{-T}}) \right\} \delta\lambda \mathrm{dV_{0S}}. \tag{4.71}$$

Applying

$$\mathrm{div}(\mathbf{v})\phi = \mathrm{div}(\mathbf{v}\phi) - \mathbf{v} \cdot \mathrm{grad}(\phi) \tag{4.72}$$

to (4.71) yields

$$\int_{\mathcal{B}_0} \left\{ -\mathrm{n^F \mathbf{w}_{FS0}} \cdot \mathrm{Grad}(\delta\lambda) + \mathrm{Div}(\mathrm{J_S \mathbf{x}_S' \mathbf{F}_S^{-T}})\delta\lambda \right\} \mathrm{dV_{0S}} +$$
$$\int_{\partial\mathcal{B}_0} \mathrm{n^F \mathbf{w}_{FS0}} \cdot \mathbf{n}_{0S} \delta\lambda \mathrm{dA_{0S}} = 0. \tag{4.73}$$

The relation $\mathrm{J_S n^F \mathbf{w}_{FS} \mathbf{F}_S^{-T}} = \mathrm{n^F \mathbf{w}_{FS0}}$ is used for the seepage velocity hence

$$\int_{\mathcal{B}_{0S}} \mathrm{Div}(\mathrm{J_S \mathbf{x}_S' \mathbf{F}_S^{-T}}) \mathrm{dV} = \int_{\mathcal{B}_{0S}} \mathrm{J_S} (\mathbf{E}_S)_S' : \mathbf{C}_S^{-1} \mathrm{dV} \tag{4.74}$$

where $(\mathbf{E}_S)_S' = \mathbf{F}_S^T \mathbf{D}_S \mathbf{F}_S$ is the material time derivative of the *Green* strain tensor $\mathbf{E}_S = \frac{1}{2}(\mathbf{C}_S - \mathbf{1})$. This yields the final weak from of the balance of mass the mixture

$$\mathrm{G_{mass}^{mix}} = \int_{\mathcal{B}_{0S}} \left\{ -\mathrm{n^F \mathbf{w}_{FS0}} \cdot \mathrm{grad}(\delta\lambda) \right\} \mathrm{dV} + \int_{\mathcal{B}_{0S}} \mathrm{J_S} (\mathbf{E}_S)_S' : \mathbf{C}_S^{-1} \delta\lambda \mathrm{dV} +$$
$$\int_{\partial\mathcal{B}_{0S}} \delta\lambda \mathrm{n^F \mathbf{w}_{FS0}} \cdot \mathbf{n}_{0S} \mathrm{dA} = 0. \tag{4.75}$$

The term related to the strain rate in (4.75) can be simplified to $(\mathbf{E}_S)_S' : \mathbf{C}_S^{-1} = \mathrm{tr}\mathbf{D}_S$.

## 4.4 Numerical Treatment

The implementation of the biphasic framework exists on SESKA[1] as a finite element code and is used in this study. All elements used are linear hexahedral 8-node finite elements and the numerical integration scheme makes use of 2nd order gauss quadrature.

Consider a solid, three-dimensional body, $B_0 = B_{0S}$ with a surface boundary $\partial B_0 = \partial B_{0S}$. The boundary value problem is comprised of unknown quantities,

$$\mathcal{U} = \{\mathbf{u}_s, \lambda\}. \tag{4.76}$$

These boundary values are given as *Dirichlet* and *Neumann* boundary conditions. *Dirichlet* boundary conditions $\partial B_D \subset \partial B$ explicitly provide a solution to a solve the equation system. The *Neumann* boundary condition is the derivative of a solution applied along a boundary $\partial B_N = \partial B \setminus \partial B_D$.

The prescribed *Dirichlet* boundary values are defined as displacement $\tilde{\mathbf{u}}_S$, and pore pressure $\tilde{\lambda}$, while the *Neumann* boundary quantities are traction $\mathbf{t}$, fluid surface flux $\mathbf{q}$ and the body force $\mathbf{b}$.

[1] The University of Cape Town's in house finite element software developed by Sebastian Skatulla

### 4.4.1 Time discretisation

The *Newmark* method[2] is the time integration scheme for the SESKA implemented biphasic model. This method is used to ensure stable finite element approximations.

Beginning with the finite difference approximation of a quantity $(\bullet)$, the Newmark equations of motion are written as follows

$$(\ddot{\bullet})_k^{n+1} = \frac{1}{\triangle \mathrm{t}^2 \beta}\left[(\bullet)_k^{n+1} - (\bullet)^n - \triangle t(\ddot{\bullet})^n - \triangle t^2\left(\frac{1}{2} - \beta\right)(\ddot{\bullet})^n\right] \qquad \text{and} \tag{4.77}$$

$$(\dot{\bullet})_k^{n+1} = (\bullet)^n + \triangle t\left[(1-\gamma)(\ddot{\bullet})^n + \gamma(\ddot{\bullet})_k^{n+1}\right] \tag{4.78}$$

where n+1 denotes the current time and k denotes the iteration step. The Newmark parameters, $\gamma$ and $\beta$, are chosen as

$$\gamma = \frac{a}{4} \qquad \text{and} \qquad \beta = \frac{1}{2}. \tag{4.79}$$

to ensure linear interpolation between discrete time steps.

The quantity in the current iteration time step must be updated using the increment of the quantity $\triangle(\bullet)$, so that

$$(\bullet)_k^{n+1} = (\bullet)_{k-1}^{n+1} + \triangle(\bullet) \tag{4.80}$$

By making use of the Newmark equations of motion as well as $(\bullet)_k^{n+1}$ the acceleration and velocity can be determined. By substituting equation (4.79) and equation (4.77) into (4.78) and computing the change with respect to the quantity $(\bullet)$, the increment for the velocity field $\triangle(\dot{\bullet})_k^{n+1}$ can be determined as

$$\triangle(\dot{\bullet})_k^{n+1} = \frac{\gamma}{\triangle t \beta}\triangle(\bullet)_k^{n+1} \tag{4.81}$$

## 4.5 Benchmark example

To ensure the validation of the results obtained by using the model, a benchmark example was run. The results obtained by the SESKA biphasic model were compared to those obtained using the software FEAP[3] provided by Andrea Thom from the University of Stuttgart. It is important to note that SESKA is a three dimensional software whereas FEAP is used to solve two dimensional problems.

A common application for TPM is soil mechanics as soil is a porous solid that can be saturated by a liquid. The two dimensional soil column shown in Figure 4.1 consisting of both clay and sand and is fully saturated with fresh water. The column is placed under a uniform

[2] The Newmark method is a numerical integration scheme used to solve differential equations and was developed by Nathan Newmark in 1959

[3] FEAP is a finite element analysis programme

compression load of 1000N and the simulation was run for 10 seconds. The bottom surface had a displacement boundary condition in the y direction equal to zero. The pore pressure on the top surface of the column is set to $0\text{N/m}^2$ thus allowing fluid to flow freely in and out the top surface. The soil column was meshed with linear elements with 8 elements along the x direction, 44 along the y direction and 2 along the z direction all equally spaced totalling 704 hexahedral elements.

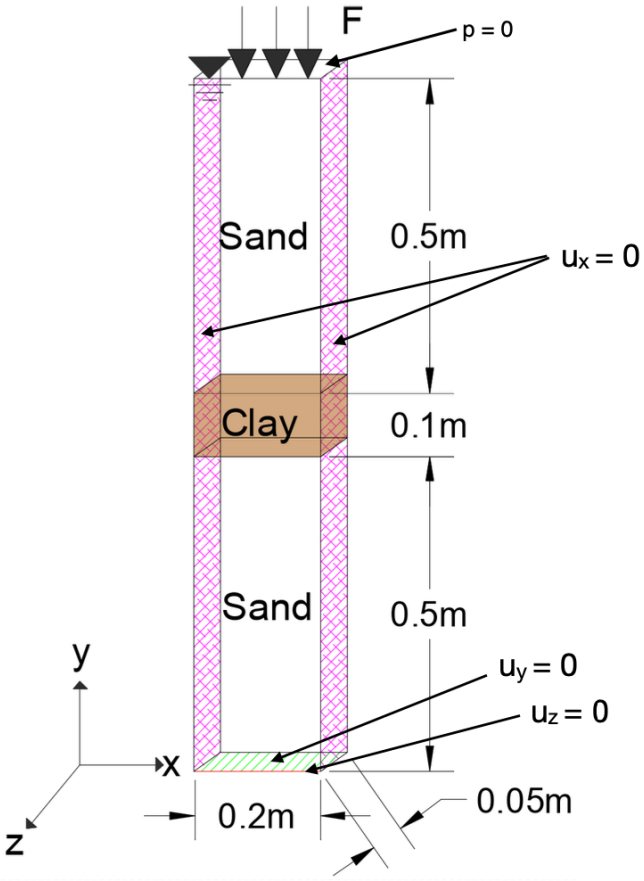


**Figure 4.1.** The three dimensional layout of the benchmark problem depicting a fully saturated soil column comprised of both clay and soil undergoing compression with boundary conditions.

The soil column problem was run on FEAP with different problem input parameters specified for Reference, IV and MP in Table 4.1 to obtain the results shown in Figure 4.2. These problem inputs vary in permeability and volume fraction.

| | $K^F_{0S}$ Sand (m/s) | $K^F_{0S}$ Clay (m/s) | $n^S_{0S}$ | $\lambda$(Pa) | $\mu$(Pa) | $\rho^{SR}$(kg/m$^3$) | $\rho^{FR}$(kg/m$^3$) |
|---|---|---|---|---|---|---|---|
| Reference | $10^{-6}$ | $10^{-8}$ | 0.6 | 27780 | 41670 | 10 000 | 1000 |
| IV | $10^{-6}$ | $10^{-8}$ | 0.8 | 27780 | 41670 | 10 000 | 1000 |
| MP | $10^{-5}$ | $10^{-7}$ | 0.6 | 27780 | 41670 | 10 000 | 1000 |

**Table 4.1.** Material parameters used for the benchmark soil problem

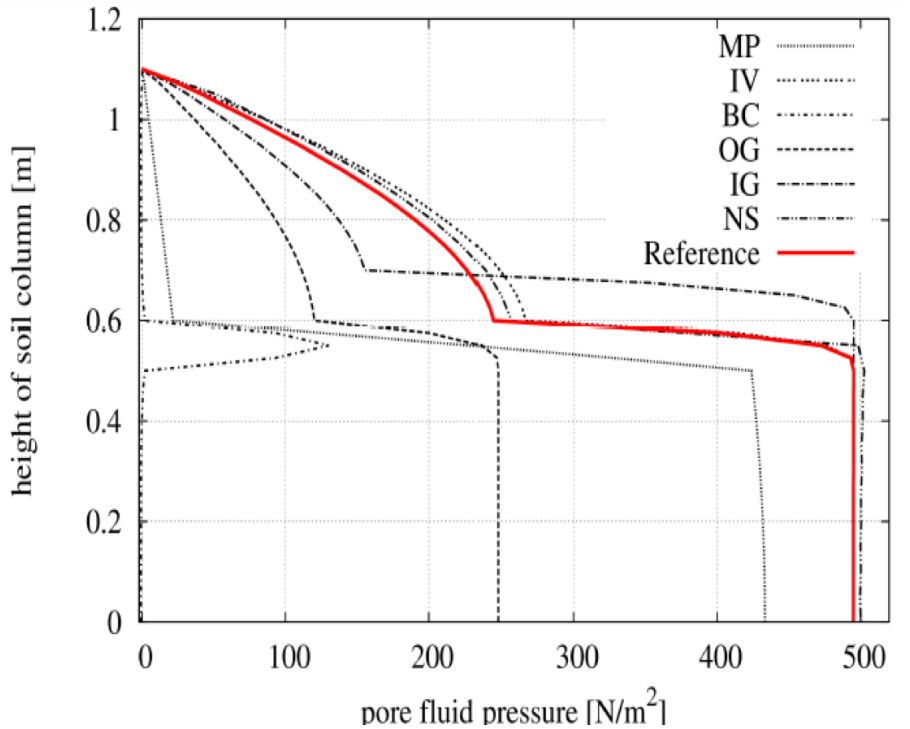


**Figure 4.2.** Height of soil column vs pore fluid pressure obtained using FEAP focusing on the Reference, MP and IV results obtained by inputting material parameters described in Table 4.1 for the two dimensional soil column problem.

To allow for validation of the SESKA biphasic model, the soil column problem had to be treated as a three dimensional problem and so the soil column was given a thickness of 0.05m and two additional *Dirichlet* boundary conditions. These are fixing the right and left surfaces of the soil column in the x Cartesian plane and a fixed line boundary condition in the z Cartesian plane as shown in Figure 4.1. This is done to achieve a plane strain problem.

It is clear that the change in material properties associated with sand and clay influences the pore pressure that develops in the soil column. This is evident in the spike in pore pressure shown in Figure 4.4 associated with the clay layer. Comparing the results of the Reference, IV and MP material inputs it is evident that the higher permeability of MP in comparison to that of Reference results in a lower pore fluid pressure as expected due to the fact that there is less resistance to fluid flow in more permeable materials. The effects of a higher solid volume fraction in IV when compared to that of Reference are only evident in the top sand layer of the soil column. The decrease in fluid volume resulted in a higher pore fluid pressure

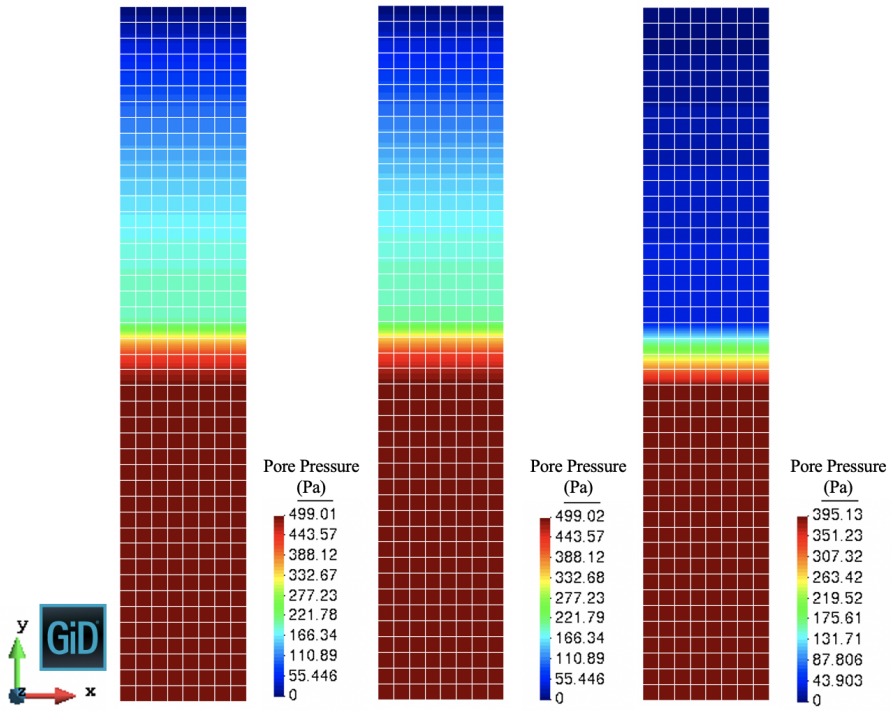


**Figure 4.3.** The three dimensional development of pore pressure ($N/m^2$) with a, b and c using the *Reference*, *IV* and *MP* material parameters respectively.

in the sand layer that lies above the clay layer. The results obtained using FEAP and SESKA, although differ slightly in values due to the additional dimension, display similar trends with the change in material inputs. The problem converged and obtained reasonable values when compared with those obtained using FEAP, making SESKA sufficient for modelling brine transport within Antarctic sea ice.

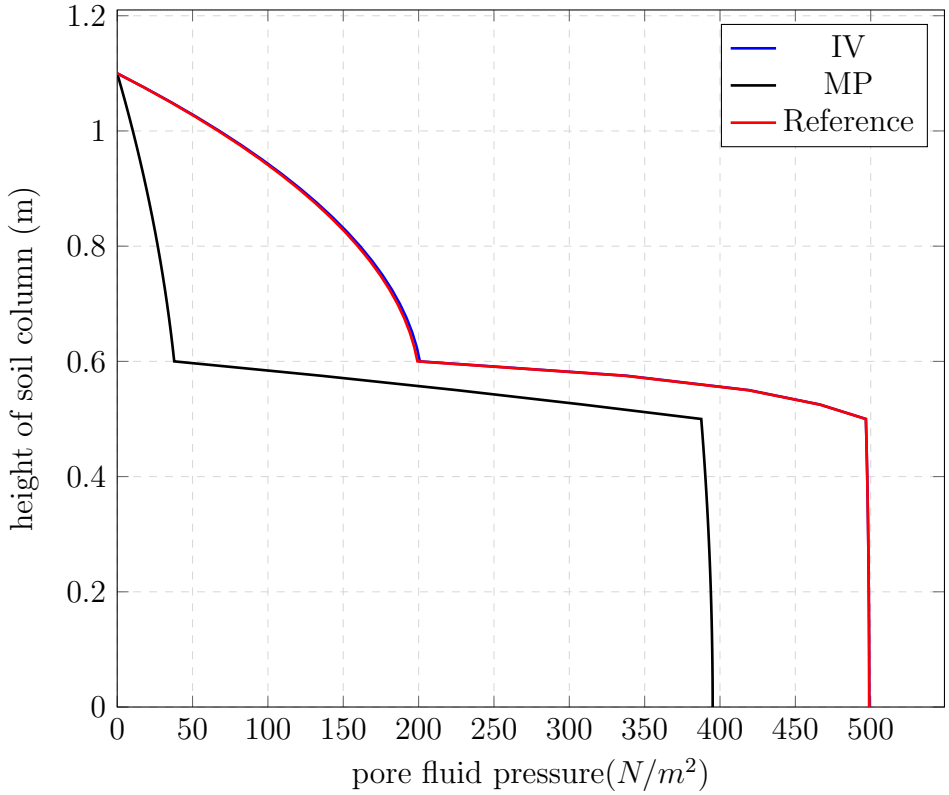


**Figure 4.4.** Height of soil column vs pore fluid pressure obtained using SESKA of various material input parameters of a three dimensional soil column problem of thickness 0.05m

# Chapter 5

# Sea ice mechanics

This chapter investigates two different types of sea ice problems which have the character of initial feasibility studies applying TPM to sea ice modelling. Accordingly, both problems are of an academic nature. The first is an experimental problem focused on the feasibility of deriving permeability from a grey-scale picture of an ice specimen and the second is aimed at simulating an idealized ice floe floating in water.

## 5.1 Grey-scale image-based permeability modelling

### 5.1.1 General

The grey-scale image-based permeability modelling problem is aimed at determining the feasibility of using TPM in conjunction with image processing techniques to asses brine transport within Antarctic sea ice. This problem is courtesy of Dr. Carina Nisters from the University of Duisburg Essen.

During the 2019 SCALE[1] Winter Cruise to the Antarctic Marginal Ice Zone, a section of an ice core was obtained, sliced into a thin section using a band saw inside the University of Cape Town's Polar Engineering Laboratory on board the SA Agulhas II and photographed within the Polar Laboratory. This image was then cropped to have 230 by 658 pixels and the resolution of the image was lowered to 60 by 172 pixels and then 30 by 86 pixels to allow for image processing at these lower resolutions. The results of these can be seen in Figure 5.1. The lower resolution images were then converted to grayscale and a script was run in Mathematica to assign each pixel a value between 0 and 1 based on its level of intensity in the grayscale. White is given the value of 1 while black is given the value of zero. It is known that the upper layers of sea ice are more porous due to their granular structure as discussed in Figure 2.4 and so white pixels are assumed to be liquid and black pixels are assumed to be solid sea ice. For the purpose of this example, the higher resolution pixelated image of 60 by 172 pixels is used.

### 5.1.2 Material parameters

The grayscale value of each pixel is then assumed to be it's liquid volume faction $n^{S}_{0S}$ and the solid volume fraction, due to the saturation condition (3.4) is $n^{F}_{0F} = 1 - n^{S}_{0S}$. This is method

[1] The Southern oCean seAsonaL Experiment is a project investigating the seasonal changes in the Southern Ocean

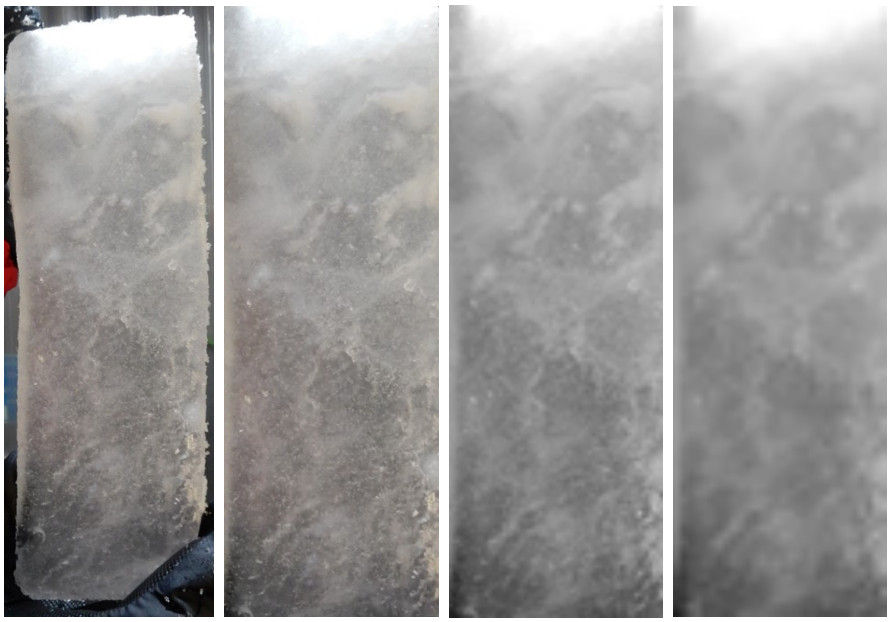


**Figure 5.1.** The processing of the image used for the pixel value problem from left to write starting with the original image of the Antarctic ice core slice, next the cropped image of the segment removing all background and then the higher and lower resolution pixelated images used for analysis.

allows for the improvement of the location of brine inclusions by giving each pixel specific values for volume fractions. The volume fractions can be seen in Figure 5.2 noting that the top of the sea ice section is prominently comprised of liquid and the bottom left corner of the segment is highly solid.

The grayscale value of each pixel is then linked to the permeability of the pixel. A linear relationship between grayscale value and permeability is assumed and is taken as follows:

$$K_m = k_f^{lb} + k_x * \Delta K \tag{5.1}$$

where $K_m$ is the permeability of the pixel, $k_f^{lb}$ is the Darcy permeability of fine sand and is specified in Table 5.1 and $k_x$ is the grayscale value for each pixel. The term $\Delta K$ is $k_f^{ub} - k_f^{lb}$ which is the difference between the Darcy permeability of coarse and fine sand as seen in Table 5.1. The permeability of sand was used as the permeability of sea ice with a porosity greater than 5% is comparable with that of fine sand [11].

### 5.1.3 Boundary conditions and meshing

The two dimensional slice was given a thickness of 0.5cm to allow for three dimensional analysis in SESKA. A linear extrapolation function was used to extrapolate volume fraction and permeability values across the x-y Cartesian plane and were kept constant across the thickness of the slice in the z direction. This three dimensional segment was then meshed with 60 elements in the x direction, 172 in the y direction and 1 in the z direction resulting in

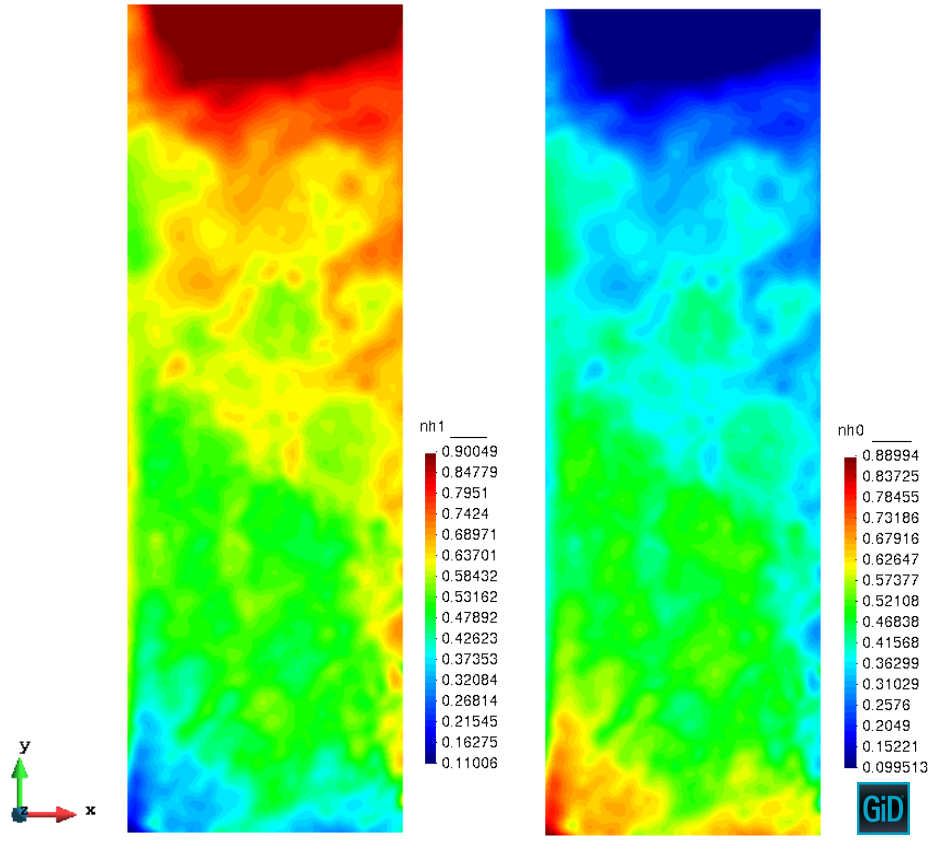


**Figure 5.2.** The liquid (left) and solid (right) volume fraction corresponding to values associated the pixelated image of 60 x 172 pixels used in solving the pixel value problem.

| Parameter | Sign | Value | Unit |
|---|---|---|---|
| Height | h | 24.9 | cm |
| Width | b | 9 | cm |
| Density | $\rho$ | 1 | kg/cm$^3$ |
| Dynamic Viscosity | $\mu$ | 1 | Ns/cm$^3$ |
| Gravity | g | 981 | cm/s$^2$ |
| Lower bound of $k_f$ | $k_f^{lb}$ | $10^{-3}$ | cm/s |
| Upper bound of $k_f$ | $k_f^{ub}$ | $10^{-1}$ | cm/s |

**Table 5.1.** Material parameters used for the pixel problem

10 320 hexahedron elements assigning an element to each pixel. The fluid is allowed free flow at the top surface of the ice segment as a result of a zero pore pressure *Dirichlet* boundary condition. Additional *Dirichlet* boundary conditions ensure that all displacement degrees of freedom are fixed. This problem does not deform to allow for a simplified problem to assess the feasibility of using imagining analysis and processing as well as grayscale values from images to investigate brine transport in Antarctic sea ice. A fluid flux *Neumann* boundary condition at bottom surface of the segment specifying an outward flow magnitude and direction of fluid $\mathbf{q} \cdot \mathbf{n} = -1$.

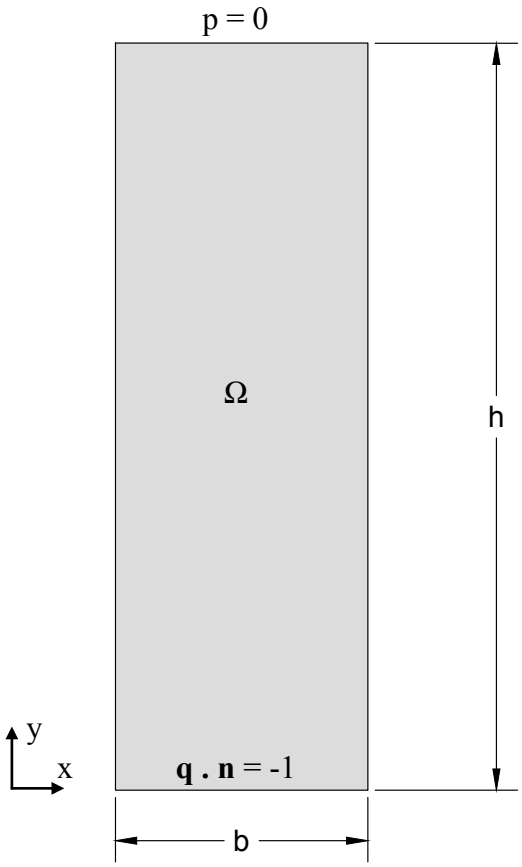


**Figure 5.3.** Boundary conditions assigned to pixel value problem.

### 5.1.4 Results and discussion

Recalling that no deformation takes place in this example, the pore pressure development is a result of the outward fluid surface flux condition specified for the bottom surface of the segment. The pore pressure within the segment increases with an increase in the depth of the segment as displayed in Figure 5.4. The pore pressure is zero at the top of the segment due to the zero pore pressure boundary condition specified for the top surface.

The x, y and absolute seepage velocities are shown in Figure 5.5 and indicate a higher seepage velocity concentrated to the bottom left corner of the segment. This is expected due to the low liquid volume fraction of this corner of the segment shown in 5.2. Recalling that a low liquid volume fraction results in a lower permeability and this low permeability causes an expected higher seepage velocity (4.47). The plot for the seepage velocity in the x direction in particular indicates the variation in the seepage velocity due to the variations in the permeability value which is linked to the liquid volume fraction shown in 5.2 through the equation described in 5.1.2. The seepage velocity in the y direction only moves downwards in the negative y direction towards the bottom surface of the segment. The vector plot displayed for the bottom section of the ice specimen shown in Figure 5.6 displays the absolute seepage velocity vectors giving greater insight into the higher seepage velocity concentrated in the bottom left corner.

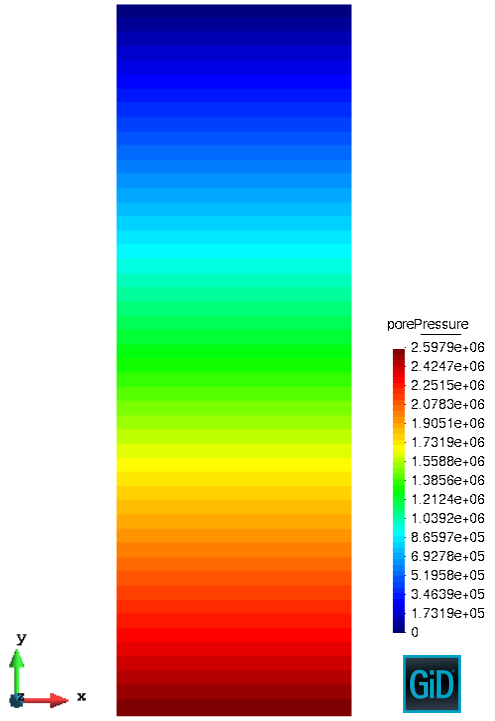


**Figure 5.4.** Pore pressure (N/cm$^2$) development in the specimen of sea ice.

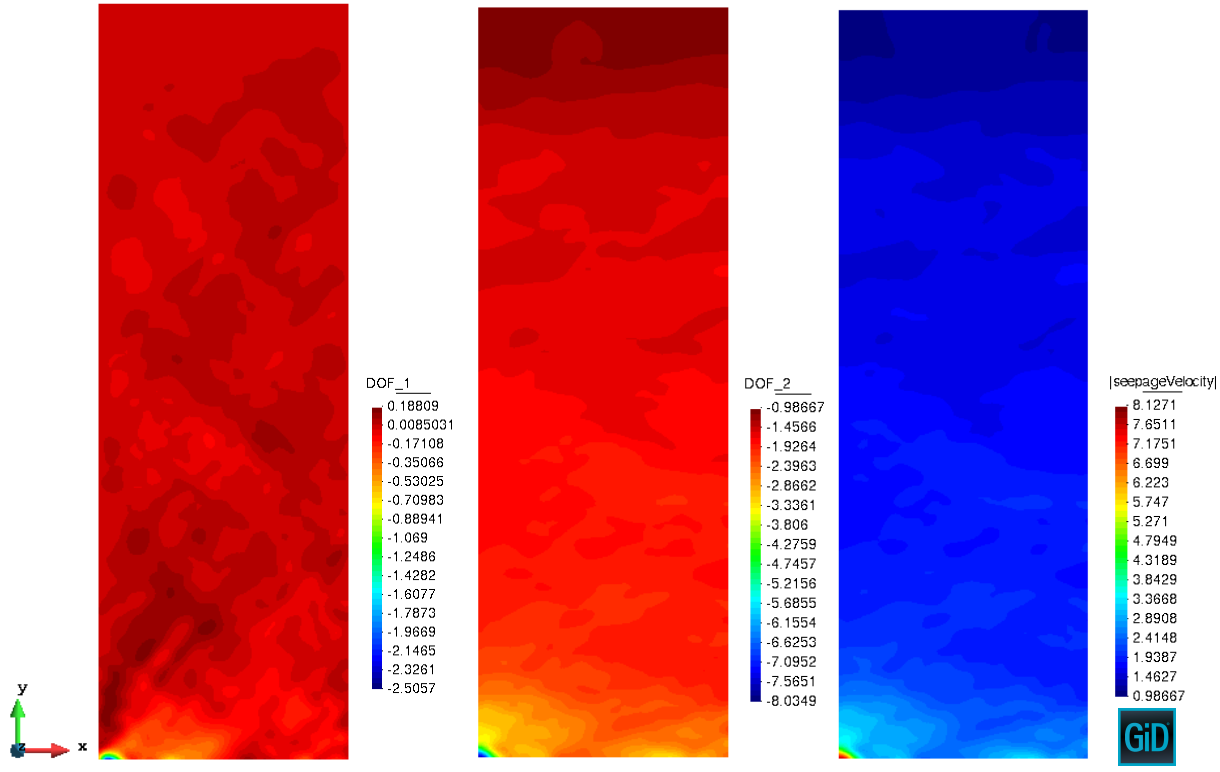


**Figure 5.5.** Horizontal x seepage velocity (left), vertical y seepage velocity (middle) and absolute seepage velocity (right) (cm/s) from a *slice* from an ice core.

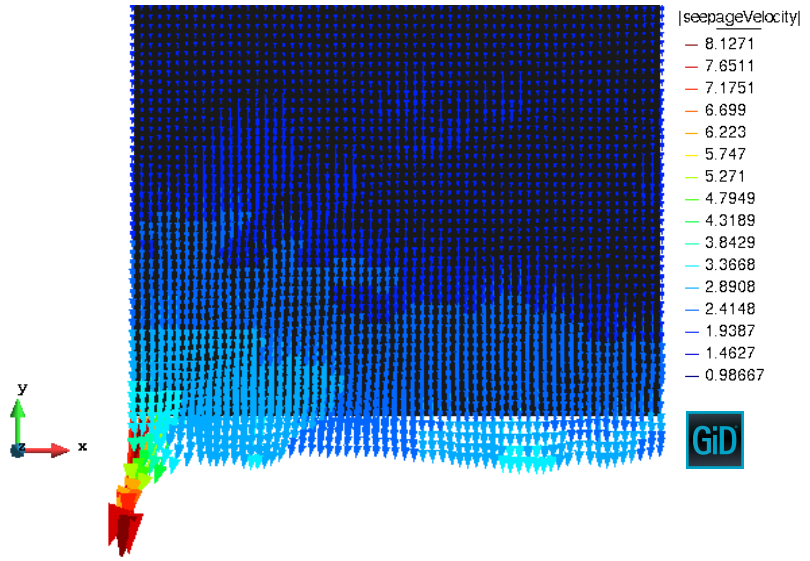


**Figure 5.6.** Absolute seepage vector (cm/s) of bottom section of specimen from a *slice* from an ice core.

## 5.2 Sea ice model

A small ice floe made up of first year ice with a depth of 50cm floating on the ocean surface is used to investigate the multidimensional nature of brine transport mechanisms in Antarctic sea ice. The problem is then assessed using three simulations with varying boundary conditions to assess brine removal mechanisms known to influence brine transport in sea ice.

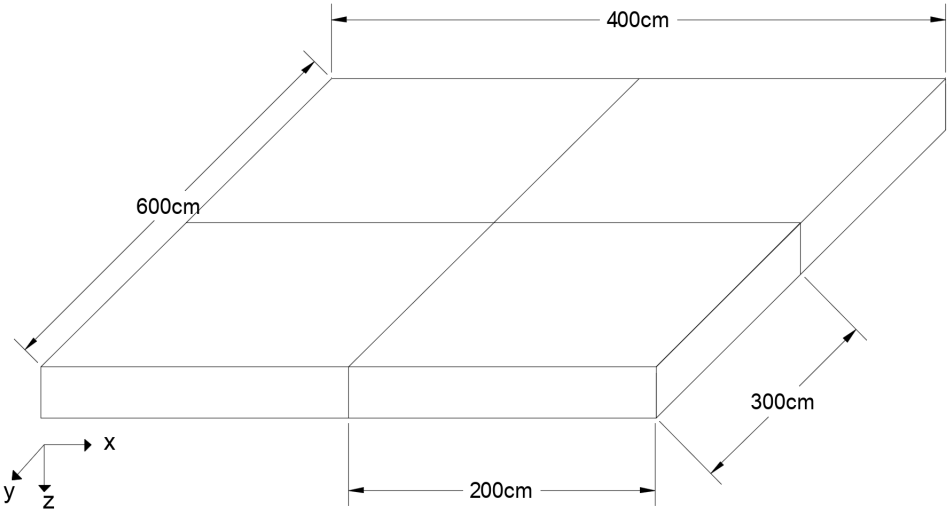


**Figure 5.7.** Ice floe layout highlighting one quarter of the ice floe modelled making use of symmetry of the floe.

### 5.2.1 Problem configuration

A quarter of the sea ice floe (600cm × 400cm × 50m) shown in Figure 5.7 is used to model the the problems described in this section due to the symmetric geometry of the ice floe. Three different problems are presented using the aforementioned geometry. The two internal symmetric cut surfaces and the two external free surfaces will be referred to throughout this section.

### 5.2.2 Problem 1: body force/gravity drainage

The body force/gravity drainage problem entails subjecting the quarter of the ice floe described in Figure 5.7 to it's self weight thus initiating brine movement within the floe due to gravity. All relevant boundary conditions for this problem are shown in Figure 5.8. Two *Dirichlet* boundary conditions exist along the internal planes of symmetry setting the x and y displacement equal to zero along these symmetric surfaces. Similarly, the ice floe is buoyant and so the displacement at the bottom surface in the z direction is equal to zero. The gravity drainage problem has *Dirichlet* boundary conditions added to the top and bottom surfaces of the ice floe setting the pore pressure of the top and bottom surfaces to zero allowing the free flow of liquid brine in and out of these two surfaces. The pore pressure along the two side external free surfaces is expected to be equal to zero and so another two *Dirichlet* zero pore pressure boundary conditions are added along these surfaces.

The gravity drainage problem has a *Neumann* boundary condition, a body force that is applied to the ice floe and is equal to the gravitational force $\mathbf{b} = 981\text{cm/s}^2$. The body force is ramped up during the first 10 time steps after which it remains constant.

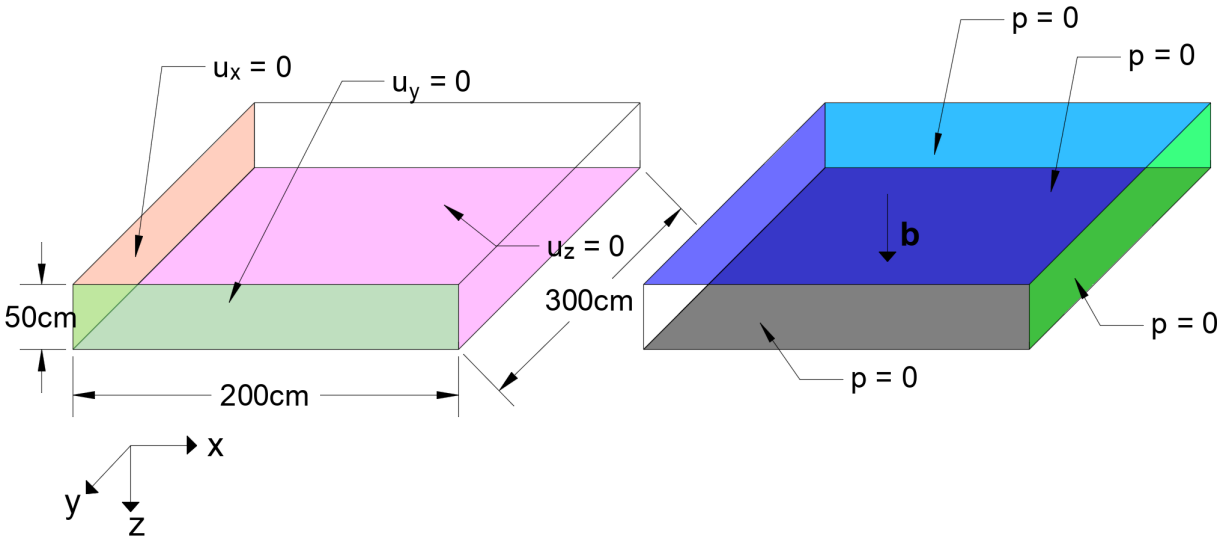


**Figure 5.8.** Quarter of ice floe indicating the pore pressure boundary conditions (left) and the displacement boundary conditions as well as the body force (right) for the problem.

### 5.2.3 Problem 2: uniform flux

The flux problem has similar boundary conditions to that of the gravity drainage problem discussed in subsection 5.2.3, however there is an additional fluid surface flux boundary condition to the top surface of the ice floe in order to simulate a meltpond on the top surface. All relevant boundary conditions for this problem are shown in Figure 5.9. Two *Dirichlet* boundary conditions exist along the planes of symmetry setting the x and y displacement equal to zero along the symmetric surfaces. Similarly, the ice floe is buoyant and so the displacement at the bottom surface in the z direction is equal to zero. The displacement boundary conditions are the same as in problem 1. The flux drainage problem has *Dirichlet* boundary condition added to the bottom and side external free surfaces of the ice floe setting the pore pressure to zero allowing the free flow of liquid brine in and out of these surfaces.

The flux problem has two *Neumann* boundary conditions, a body force that is applied to the ice floe and is equal to the gravitational force $\mathbf{b} = 981\text{cm/s}^2$ as well as a fluid surface flux applied to the top surface of the ice floe $\mathbf{q_1} \cdot \mathbf{n} = 106.64\text{cm/s}^2$. The magnitude for the applied flux force is determined from the steady state solution of the previous example. This is explained in section 5.2.6.

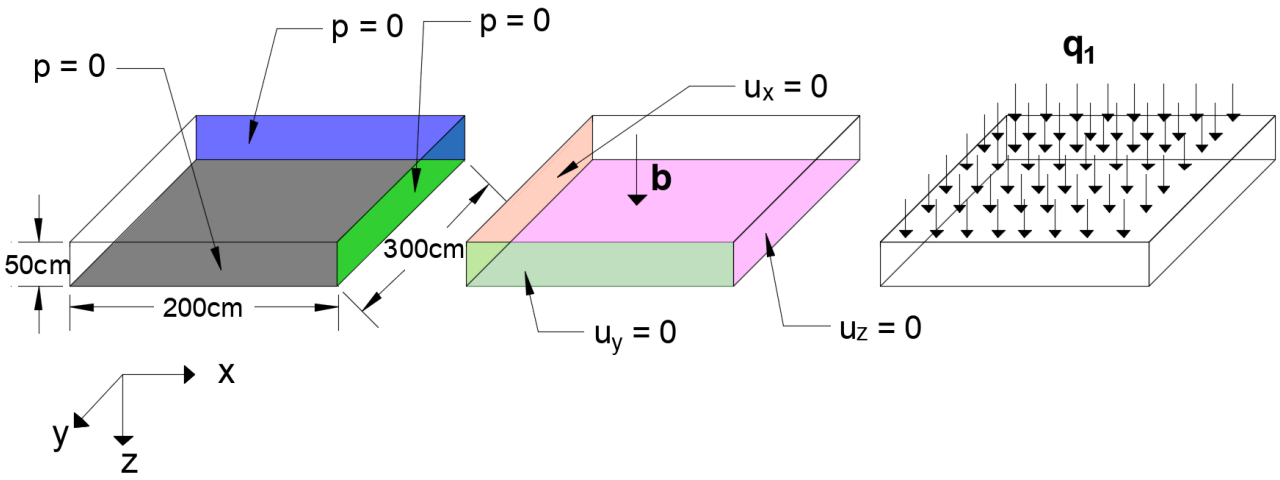


**Figure 5.9.** Quarter of ice floe indicating the pore pressure boundary conditions (left), the displacement boundary conditions as well as the body force (middle) and the flux boundary condition (right) for the problem.

### 5.2.4 Problem 3: non-uniform flux

All relevant boundary conditions for this problem are shown in Figure 5.10. All *Dirichlet* boundary conditions for problem 3 are the same as shown described in problem two (section 5.2.3).

This problem has three *Neumann* boundary conditions, a body force that is applied to the ice floe and is equal to the gravitational force $\mathbf{b} = 981\text{cm/s}^2$ as well as a two fluid surface flux

applied to the top surface of the ice floe $\mathbf{q_1} \cdot \mathbf{n} = 106.64\text{cm/s}^2$ and $\mathbf{q_2} \cdot \mathbf{n} = 130\text{cm/s}^2$. The larger fluid surface flux is applied to the inner half of the floe. The addition of two fluid surface fluxes allows for non uniform flux to be applied to the floe which more accurately represents the uneven pressure that surface meltwater/meltponds exert on the ice floe surface.

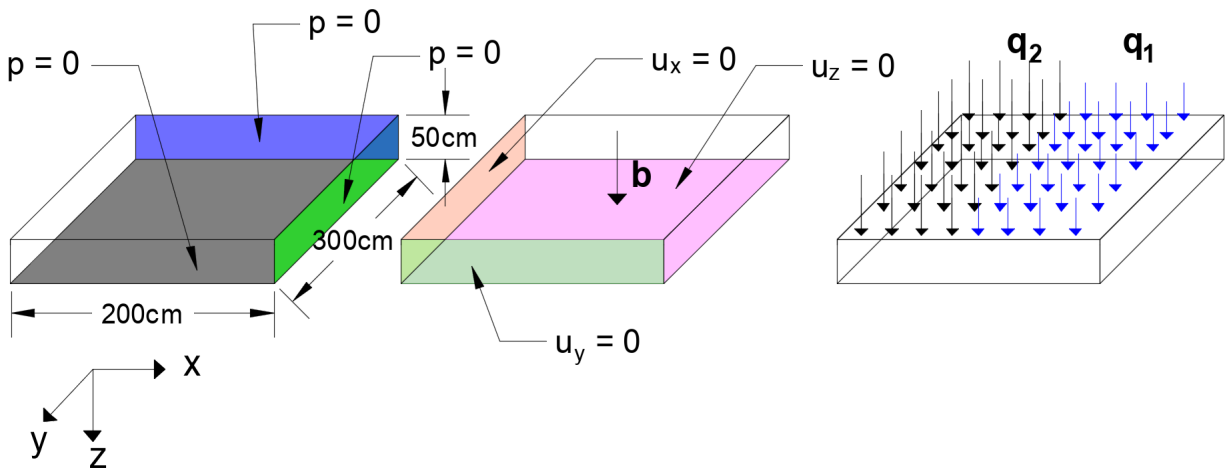


**Figure 5.10.** Quarter of ice floe indicating the pore pressure boundary conditions (left), the displacement boundary conditions as well as the body force (middle) and the flux boundary condition (right) for the problem.

A sea ice density of $920\text{kg/m}^3$ as suggested by Timco *et al.* [39], is assumed to be a reasonable estimate for the density of first year ice. The bulk salinity of first year sea ice $S_{si}$ is said to be approximately 5 PSU [14] however for the purpose of this study, 10 PSU was used to allow for a higher brine content resulting in a higher liquid brine volume fraction $n^F_{0F}$. Materials with lower liquid volume fractions lean towards behaving like single phase materials and not multiphase materials. It is assumed that the density of the entrapped brine is equal to that of sea water. Based on the relationship between a temperature of $-2°$ C and the bulk salinity of 10 PSU Figure 2.6 was used to obtain a liquid brine volume fraction of 0.2. The intrinsic permeability is taken as $4 \times 10^{-10}$ $(\text{m}^2)$ [10]. The quarter of the ice floe is meshed using the same mesh for all three examples. This consists of 5 elements in the z direction, 20 elements in the x direction and 30 elements in the y direction resulting in 3000 hexahedron elements.

| Parameter | Value | Unit |
|---|---|---|
| $\rho^{SR}_{0S}$ | $9.26 \times 10^{-4}$ | $\text{kg/cm}^3$ |
| $\rho^{FR}_{0F}$ | $1.027 \times 10^{-3}$ | $\text{kg/cm}^3$ |
| $n^S_{0S}$ | 0.8 | - |
| $K^F_{0S}$ | $4 \times 10^{-}6$ | $\text{cm}^2$ |
| $\mu_{\text{seawater}}$ | $1.89 \times 10^{-7}$ | $\text{Ns/cm}^2$ |
| $\lambda$ | $1.094 \times 10^6$ | $\text{N/cm}^2$ |
| $\mu$ | $3.633 \times 10^5$ | $\text{N/cm}^2$ |

**Table 5.2.** Material parameters used for sea ice model

### 5.2.5 Results and discussion

The following subsection focuses on the results obtained for the gravity drainage, uniform and non-uniform flux problems. Deformation within the ice floe results in pressure within the pore space that then drives the movement of brine within the ice floe and so the stress, strain, pore pressure and seepage velocity are assessed in this section.

### 5.2.6 Problem 1: body force/gravity drainage

The ice floe undergoes deformation due to its own self weight in this problem. The floe deforms due to compression under its own self weight. The stress and stain in the floe as well as the pore pressure and liquid seepage velocity are assessed in this section.

#### Stress and strain

The contour plots shown in Figure 5.11 indicate the effective stress and strain distribution in the ice floe for the body force problem. The effective stress and strain in is calculated as

$$\mathrm{S_{eff}} = \sqrt{\sigma_{ij} : \sigma_{ij}} \qquad \text{and} \qquad \mathrm{E_{eff}} = \sqrt{\epsilon_{ij} : \epsilon_{ij}} \tag{5.2}$$

for the stress and strain respectively.

It is expected that the highest stress would occur at the surfaces where deformation is restrained in one or more directions. This is the case for the gravity drainage problem as the highest stress occurs along the bottom surface of the floe which has a displacement boundary condition equal to zero in the z direction. There is also a high stress along the bottom of the internal symmetric cut surfaces in the floe.

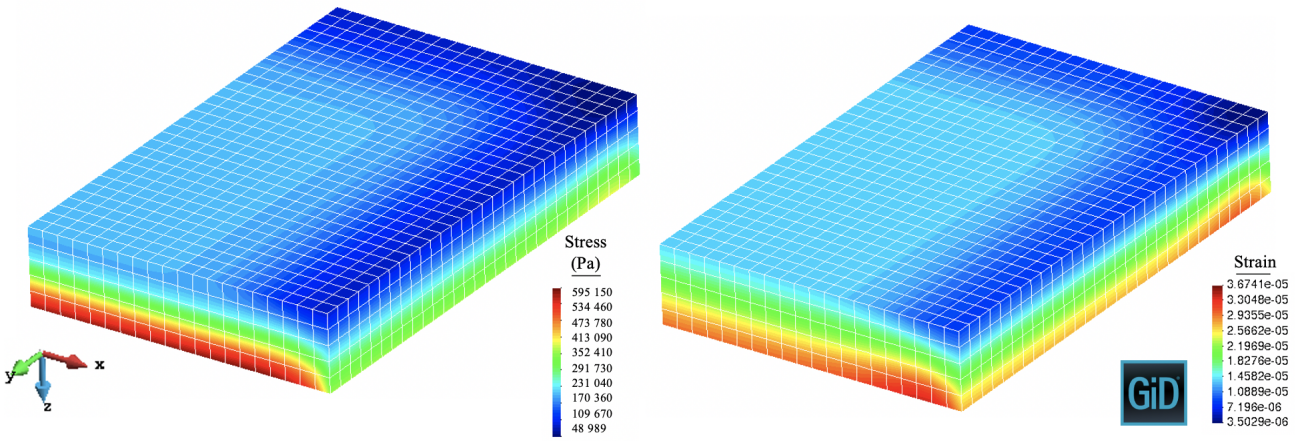


**Figure 5.11.** Effective stress (left) and strain (right) contour plots for the body force problem at steady state

The largest strain that the floe experiences is at the bottom surface of the ice floe along the free surfaces. This is the area most likely to experience the most elongation as it is free to deform along the free edges under the compression of its self weight. The lowest strain can be found at the top surface towards the intersection of the two external free surfaces.

### Pore pressure evolution

The pore pressure contour plot shown in Figure 5.12 indicates that the pore pressure at the top, bottom and free side surfaces remains zero due to the enforced boundary conditions thus allowing fluid to flow out of these surfaces. A high pore pressure develops along the two symmetric cut surfaces of the floe and is concentrated at half of the floe depth. This high pore pressure is due to the floe experiencing compression causing a reduction in the pore spacing thus increasing the pore pressure. The pore pressure developed throughout the ice floe is positive indicating a reduction in the size of the pore space expelling fluid away from the pores. An increase in pressure will drive liquid brine out of the ice which occurs in a gravity drainage problem discussed in subsection 2.3.3.

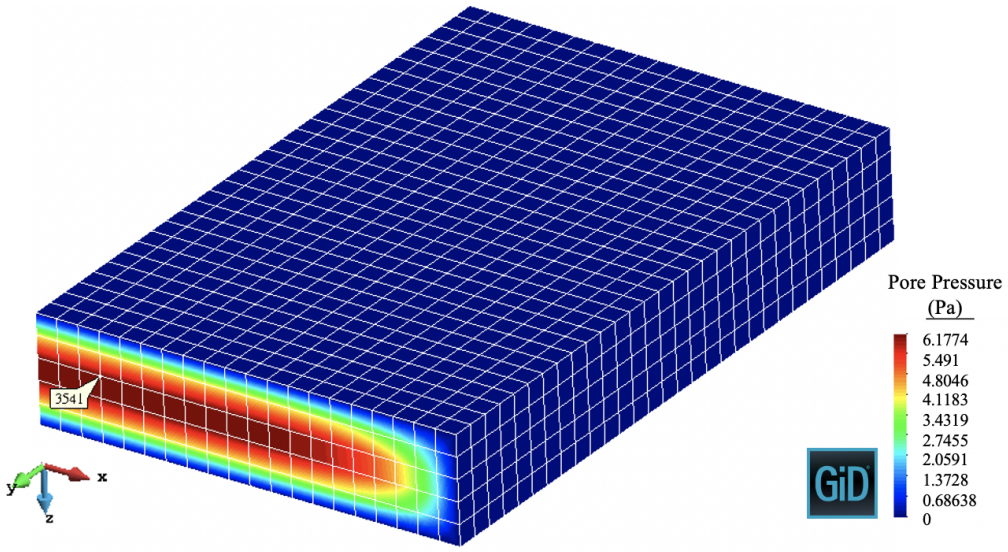


**Figure 5.12.** Pore pressure of a quarter of the ice floe under boundary conditions for problem 1, the body force/gravity drainage problem.

In Figure 5.13 describing the pore pressure evolution of node 3541 located as shown in Figure 5.12, there is an initial increase of the pore pressure coinciding with the ramping up of the body force applied to the floe. Once the body force remains constant, the stress and strain within the floe remains constant and there is a sudden decrease in pore pressure until it reaches a steady state of 6.169 Pa.

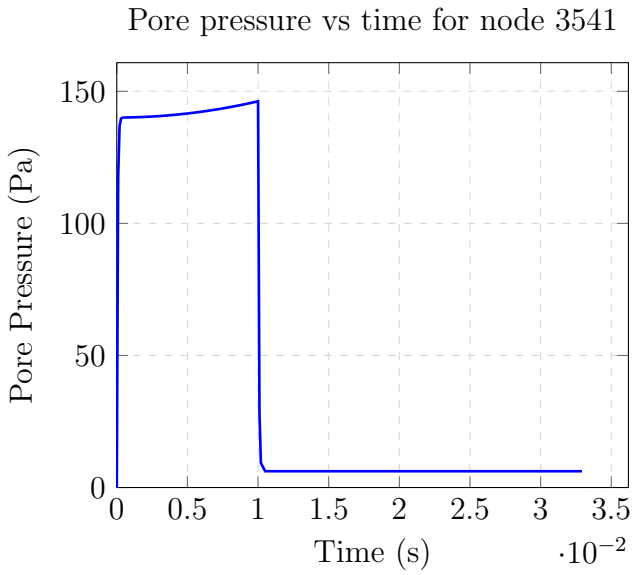


**Figure 5.13.** Pore pressure vs time for node 3541 for problem 1: the body force/gravity drainage problem.

### Seepage velocity

The amount of fluid within the internal pores of the ice floe and the movement of such fluid within the ice is directly linked to the pore pressure within the pores. The seepage velocity vector plot shown in Figure 5.14 indicates a downward flow of internal brine (positive z direction) at a constant velocity of 106.6cm/s. This positive z flow is expected due to the body force applied in the positive z direction along with the zero pore pressure boundary conditions applied to the top and bottom of the ice floe. The downward flow of liquid brine is typical for a gravity drainage problem as discussed in subsection 2.3.3. Although fluid is free to flow out of the external free surfaces due to the zero pore pressure boundary condition at these surfaces, there is no horizontal flow in the x and y direction as expected.

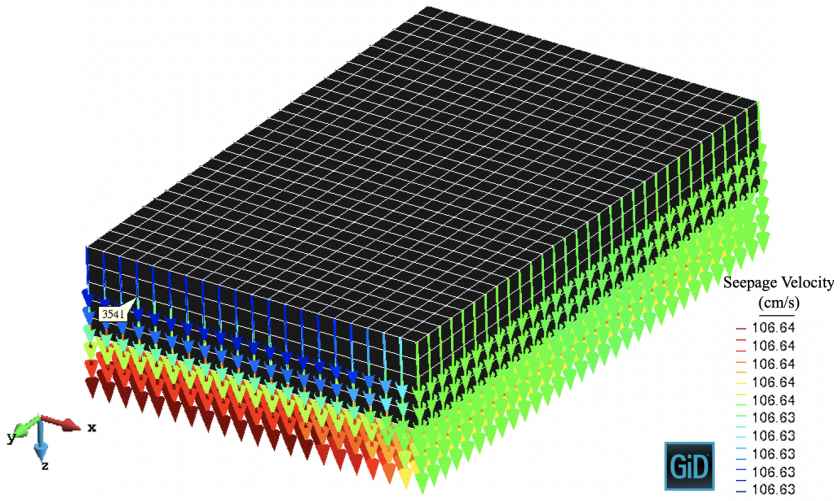


**Figure 5.14.** Seepage velocity of a quarter of the ice floe under boundary conditions for problem 1, the body force/gravity drainage problem.

In Figure 5.15 describing the seepage velocity evolution of node 3541 shown in Figure 5.12, we can see an initial spike in the seepage velocity. This is due to the application of the body force after which the body force remains constant and the seepage velocity increases slightly until it reaches a steady state of 106.64cm/s. The direction of the fluid flow in the positive z direction is due to the direction of the body force.

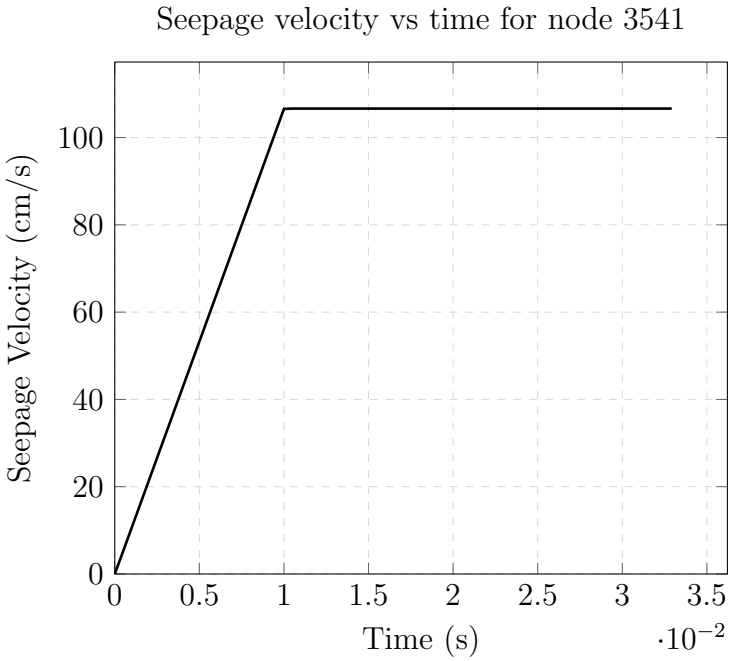


**Figure 5.15.** Seepage velocity vs time for node 3541 for problem 1: the body force/gravity drainage problem.

### 5.2.7 Problem 2: uniform flux

The ice floe undergoes deformation due to its own self weight as well as the uniform fluid surface flux applied to the top surface of the floe in this problem.

#### Stress and strain

The contour plots shown in Figure 5.16 indicate the effective stress and strain distributions in the ice floe for the uniform flux problem and are computed using the equation shown in (5.2).

The stress in the uniform flux problem is much greater than that in the gravity drainage problem as a result of the addition of the uniform surface fluid flux which induces a larger deformation. The stress along the bottom surface as well as the external free surfaces is low and there is a concentration of stress at the top of the ice floe towards the intersection of the two internal symmetric cut surfaces.

The floe experiences maximum strain at the interface of the two symmetric cut surfaces and the least amount of compression at the interface of the two free surfaces along the top surface of the ice floe.

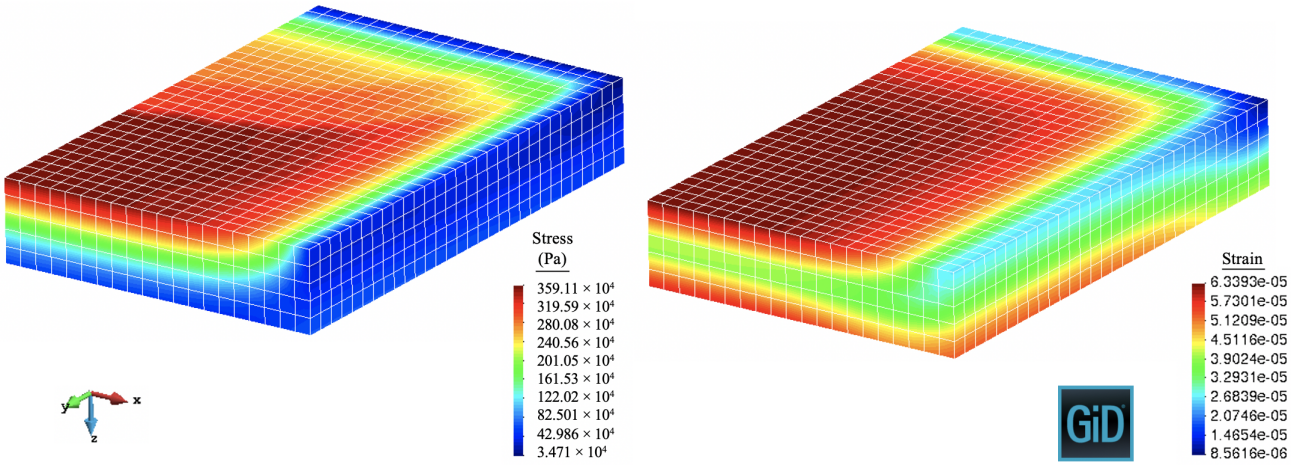


**Figure 5.16.** Effective stress (left) and strain (right) contour plots for the uniform flux problem at steady state

### Pore pressure evolution

The pore pressure contour plot shown in Figure 5.17 indicates that the pore pressure at the bottom and free side surfaces remains zero due to the enforced boundary condition. The highest pore pressure that the ice floe experiences is at the corner where the two internal symmetric surfaces meet. This too is where the highest strain is experienced within the floe.

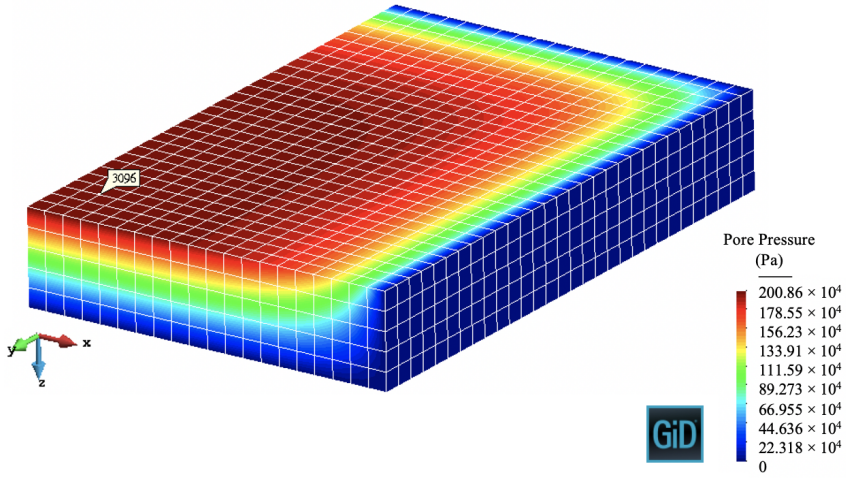


**Figure 5.17.** Pore pressure of a quarter of an ice floe under boundary conditions for problem 2, the uniform flux problem.

It is notable that there is a concentration of pressure towards the top, center of the ice floe which then decreases towards the enforced zero pore pressure boundaries at the bottom and on the free sides. The pore pressure developed throughout the floe is positive indicating that internal fluid will flow away from the pore space.

In Figure 5.18 describing the pore pressure evolution of node 3096 located as shown in Figure 5.17, there is an initial increase of the pore pressure coinciding with the ramping up of the body force and fluid surface flux applied to the floe. Once the body force and fluid surface flux reach constant values, the pore pressure continues to increase at a more gradual rate until it reaches a steady state of $2.007 \times 10^6$ Pa.

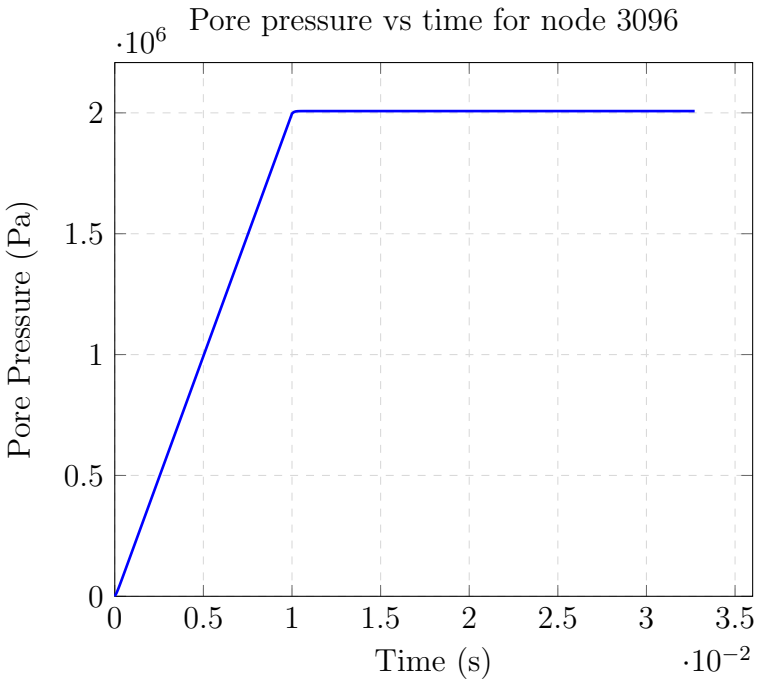


**Figure 5.18.** Pore pressure vs time for node 3096 for problem 2: the flux problem.

### Seepage velocity

As discussed in subsection 5.2.6, the amount of fluid within the internal pores of the ice floe and the movement of such fluid within the ice is directly linked to the pore pressure within the pores. The positive pore pressure that develops within the floe shown in Figure 5.2.7 suggests that the flow direction of internal brine within the ice will be away from the internal pores (drainage).

The seepage velocity vector plot shown in Figure 5.19 indicates a downward flow of internal brine (positive z direction) however, there is a horizontal (in the x and y direction) fluid flux towards the external free surfaces which is higher in the upper portion of the ice floe. The positive z flow is expected due to the body force applied in the positive z direction along with the zero pore pressure boundary condition applied to the bottom of the ice floe. The horizontal fluid flux can be explained in conjunction with the pore pressure contour plot, Figure 5.17.

The internal brine will flow towards the zero pore pressure boundary implemented on the external side surfaces of the floe. The gradient of the pore pressure shown in Figure 5.20 is highest at the top external free surfaces which experiences the highest horizontal fluid flux (see (4.50)). It is evident that the majority of fluid flow is in the vertical (positive z) direction which is expected as discussed in subsection 2.3.4 as it is dominant.

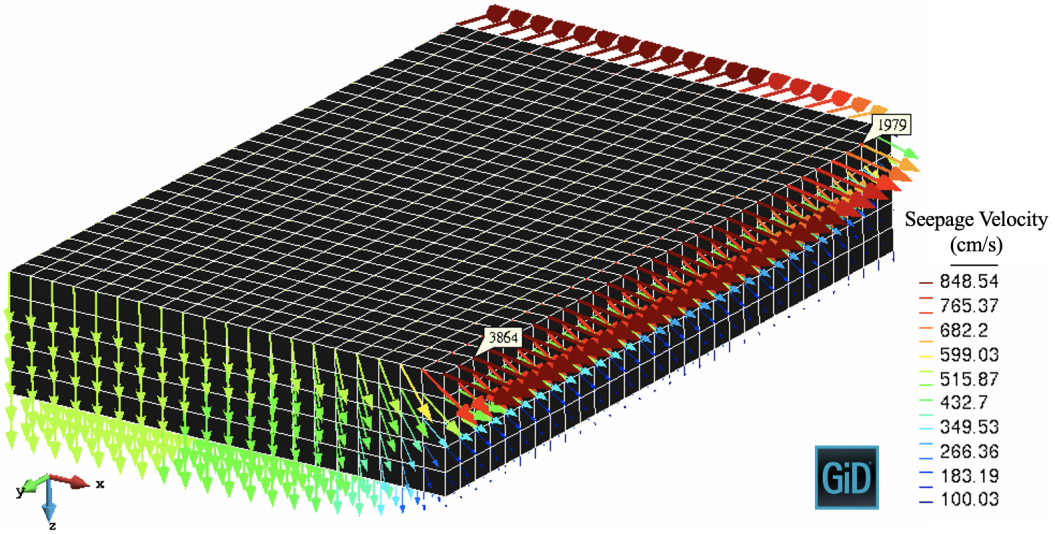


**Figure 5.19.** Seepage velocity of a quarter of an ice floe under boundary conditions for problem 2, the uniform flux problem at steady state.

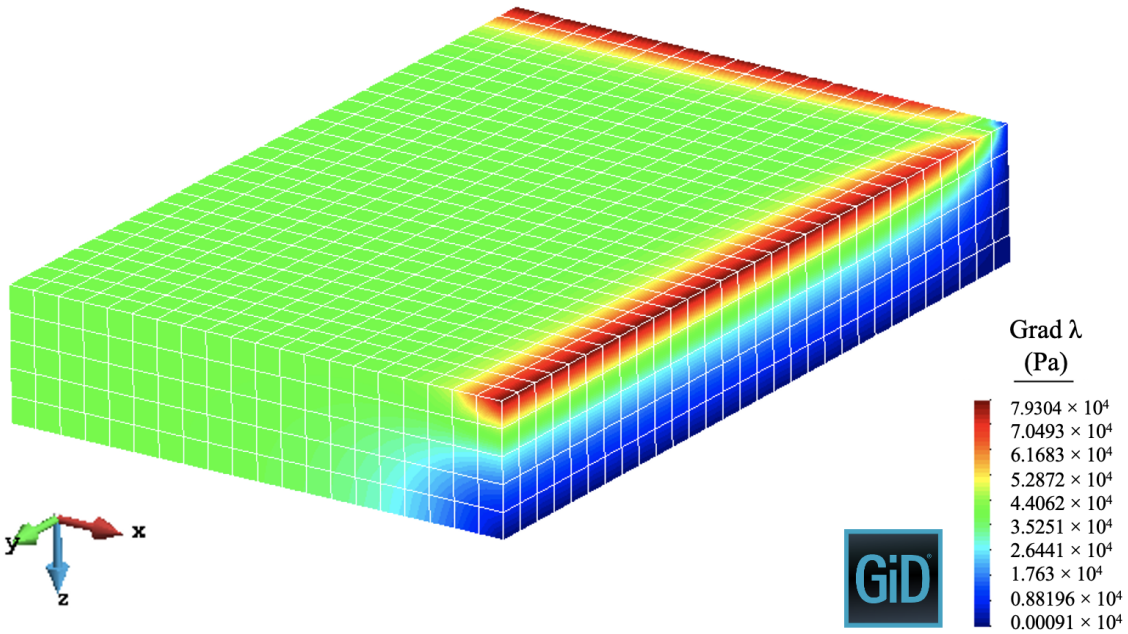


**Figure 5.20.** grad$\lambda$ of a quarter of an ice floe under boundary conditions for problem 2, the uniform flux problem at steady state.

In Figure 5.21 describing the seepage velocity evolution at nodes 1979 and 3864 located as shown in Figure 5.17, we can see an initial spike in the seepage velocity at both nodes. This is due to the application of the body force and uniform fluid surface flux after which the applied loads remains constant and the seepage velocity continues to increase at a more gradual rate until it reaches a steady state of 644.313cm/s for node 1979 and 848.531cm/s for node 3864. The seepage velocity at node 3864 located closer toward the internal symmetric cut surface is larger than that of node 1979 which is located toward the intersection of the two external free surfaces. This is due to the pore pressure gradient shown in Figure 5.20 as a higher pore pressure gradient results in a higher seepage velocity.

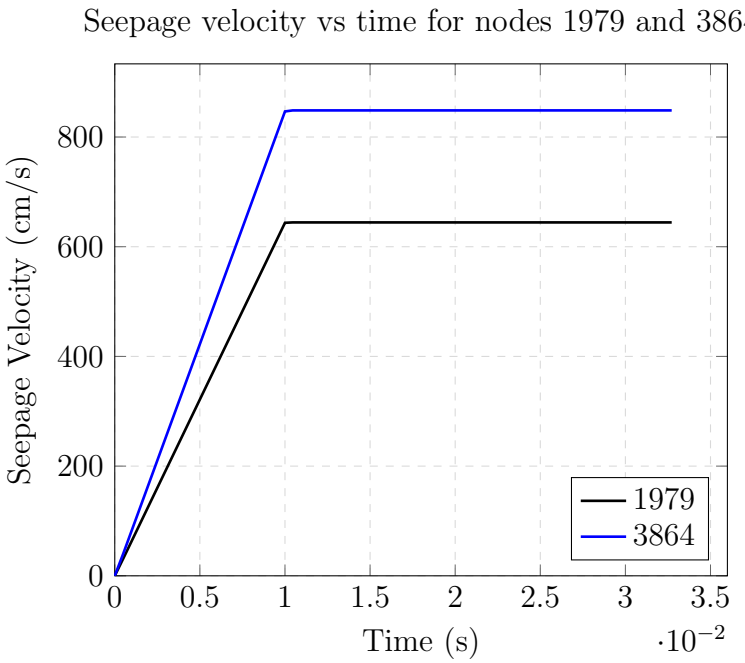


**Figure 5.21.** Seepage velocity vs time for nodes 1979 and 3864 for problem 2: the uniform flux problem.

### 5.2.8 Problem 3: non-uniform flux

The ice floe undergoes deformation due to its own self weight as well as the non-uniform fluid surface flux applied to the top surface of the floe in this problem.

#### Stress and strain

The contour plots shown in Figure 5.22 indicate the effective stress and strain distributions in the ice floe for the non-uniform flux problem and are computed using the equation shown in (5.2).

The stress in the non-uniform flux problem is much greater than that in the uniform flux problem as a result of the addition of the non-uniform surface fluid flux which induces a larger deformation as it is larger in magnitude than the uniform flux applied.

The floe experiences maximum strain at the interface of the two symmetric cut surfaces and the least amount of compression at the interface of the two free surfaces. The maximum stress that the floe experiences is located towards the symmetric cut surface in the half of the floe subjected to the higher fluid surface flux.

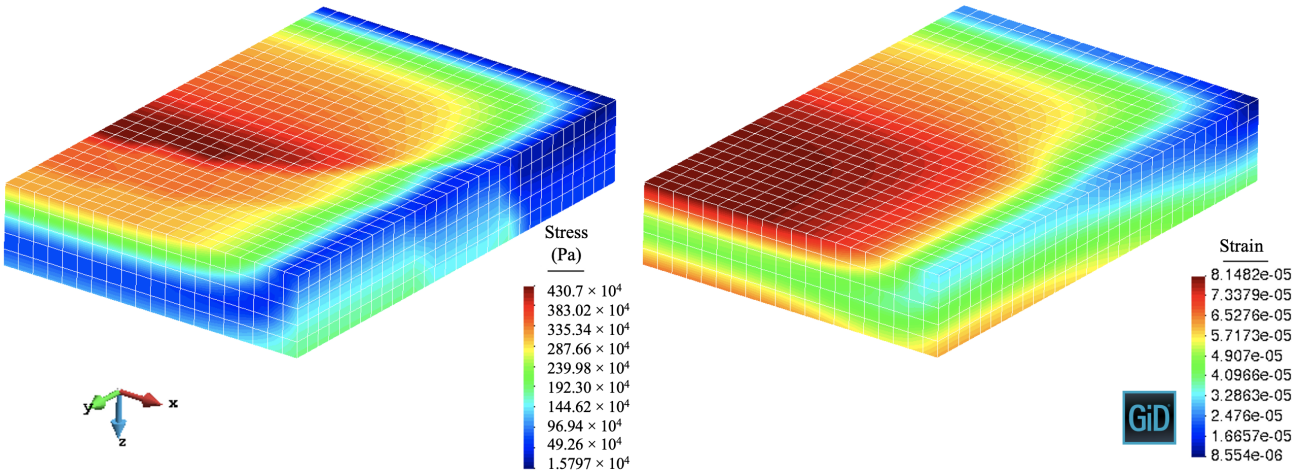


**Figure 5.22.** Effective stress (left) and strain (right) contour plots for the non uniform flux problem at steady state

### Pore pressure evolution

The pore pressure contour plot shown in Figure 5.23 indicates that the pore pressure at the bottom and free side surfaces remains zero due to the enforced boundary condition. The highest pore pressure that the ice floe experiences is at the corner where the two internal symmetric surfaces meet. This too is where the highest strain is experienced. It is notable that there is a concentration of pressure towards the top, center of the ice floe which then decreases towards the enforced zero pore pressure boundaries at the bottom and on the external free surfaces.

When comparing the pore pressure in the non-uniform flux problem to that of the uniform flux problem shown in Figure 5.17, it is clear that the half of the floe that is experiencing the higher fluid surface flue due to the non-uniform load develops a higher pore pressure. This is due to the increased deformation the high flux causes. The pore pressure developed throughout the floe is positive indicating that internal fluid will flow away from the pore space.

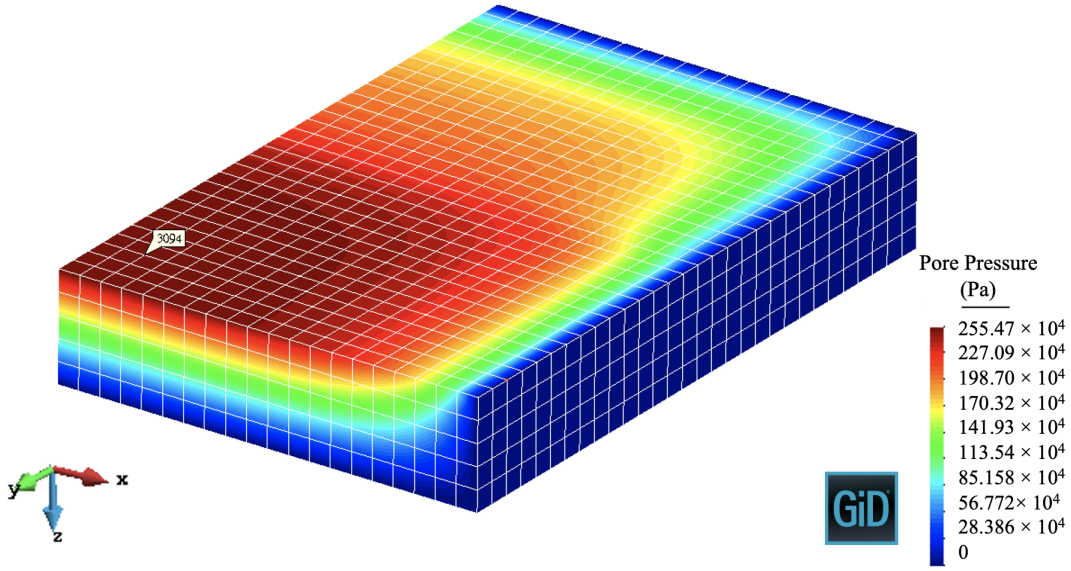


**Figure 5.23.** Pore pressure of a quarter of an ice floe under boundary conditions for problem 3, the non-uniform flux problem at steady state.

In Figure 5.24 describing the pore pressure evolution of node 3094 located as shown in Figure 5.23, there is an initial increase of the pore pressure coinciding with the ramping up of the body force and non-uniform fluid surface flux applied to the floe. Once the body force and fluid surface flux reach constant values, the pore pressure continues to increase at a more gradual rate until it reaches a steady state of $2.551 \times 10^6$ Pa.

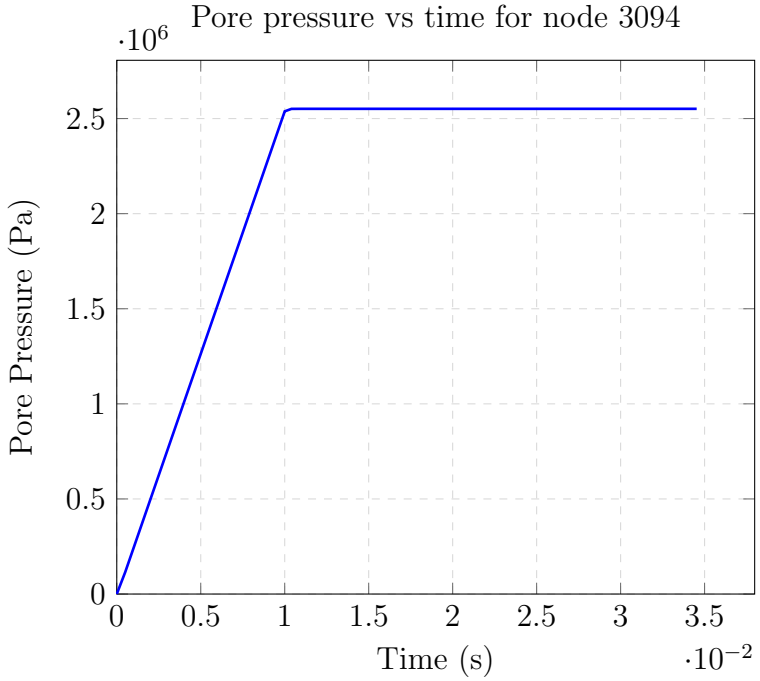


**Figure 5.24.** Pore pressure vs time for node 3094 for problem 3: the non-uniform flux problem.

### 5.2.9 Seepage velocity

The seepage velocity vector plot shown in Figure 5.25 indicates a downward flow of internal brine (positive z direction) however, the external free surfaces experience a horizontal (x and y component) fluid flux that is higher in the upper portion of the ice floe along the free surfaces. The flow in the positive z direction is expected due to the body force applied in the positive z direction along with the zero pore pressure boundary condition applied to the bottom of the ice floe. The addition of the non uniform flux also causes seepage in the y coordinate direction at the interface where the two fluxes of different magnitudes meet (at half of the width along the y coordinate axis) as shown in Figure 5.26.

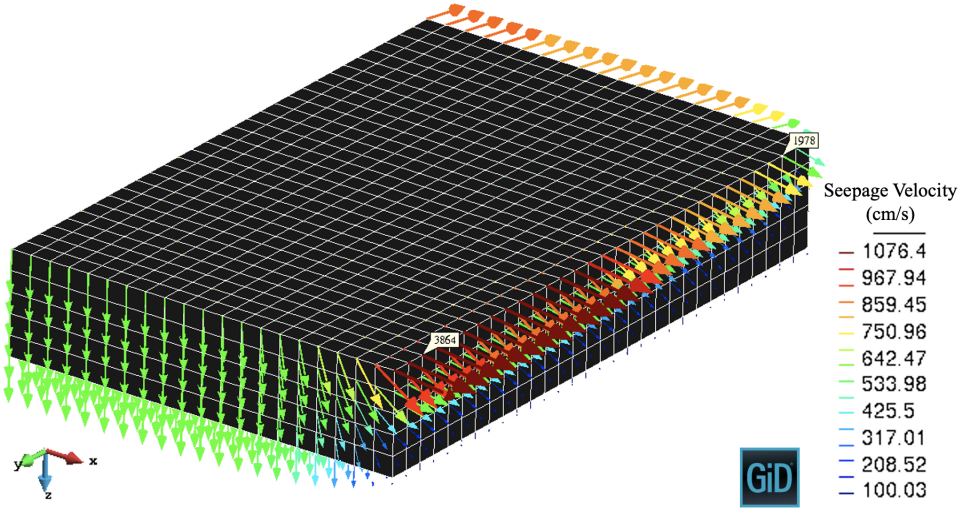


**Figure 5.25.** Seepage velocity of a quarter of an ice floe under boundary conditions for problem 3, the non-uniform flux problem at steady state.

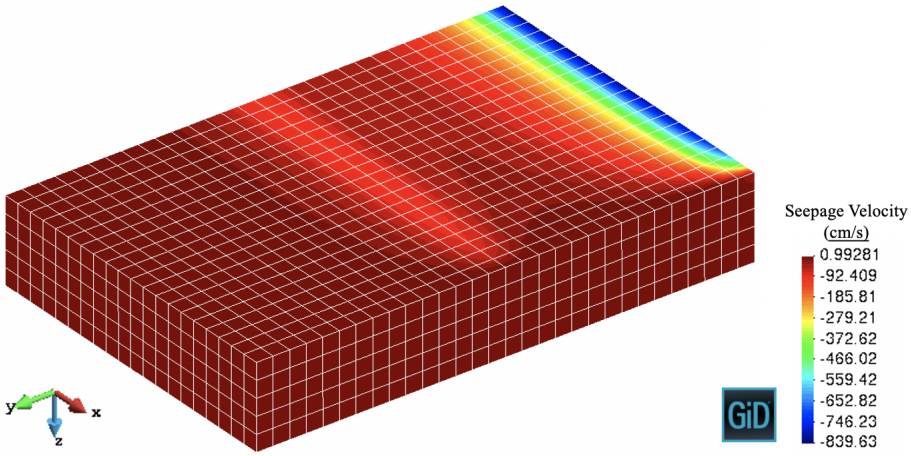


**Figure 5.26.** y component of seepage velocity of a quarter of an ice floe under boundary conditions for problem 3, the non-uniform flux problem.

The gradient of the pore pressure shown in Figure 5.27 is highest at the top, external free surface in the half of the floe that is experiencing the highest fluid surface flux. This then gradually decreases to the corner of the floe where the two external free surfaces meet. The gradient of the pore pressure in the non-uniform flux problem is larger than that in the uniform flux problem as the floe experiences a larger deformation due to the higher flux and thus a larger contraction in the pore space increasing the pressure. The area in the floe with the highest pore pressure gradient experiences the highest seepage velocity (see (4.50)). It is evident that a higher fluid surface flux which translates to larger meltponds mentioned in subsection 2.3.4 translate to a larger seepage velocity.

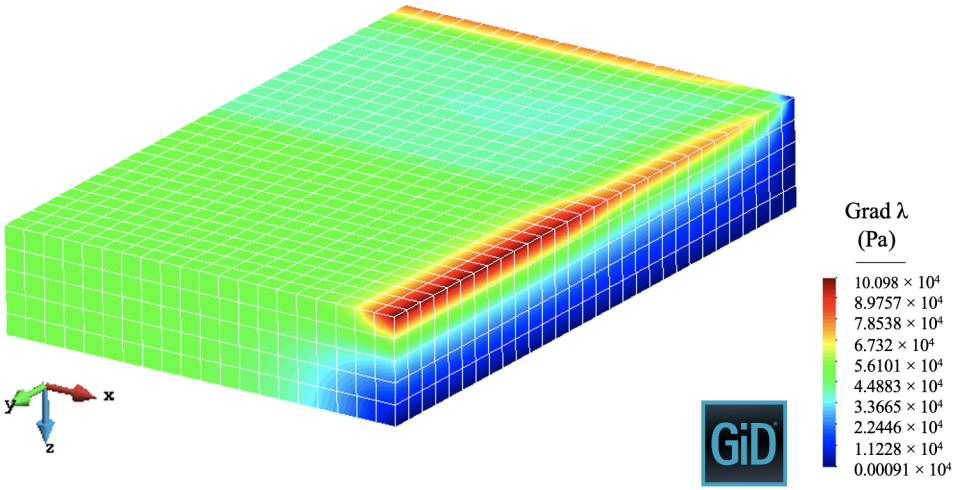


**Figure 5.27.** grad$\lambda$ of a quarter of an ice floe under boundary conditions for problem 3, the non uniform flux problem.

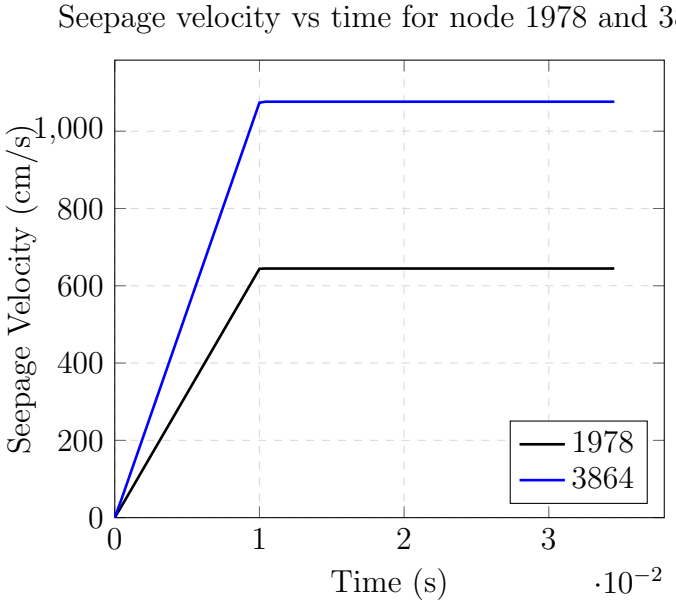


**Figure 5.28.** Seepage velocity vs time for node 1978 and 3864 for problem 3: the non-uniform flux problem.

In Figure 5.28 describing the seepage velocity evolution of nodes 1978 and 3864 located as shown in Figure 5.23, we can see an initial increase in the seepage velocity. This is due to the application of the body force and fluid surface fluxes after which the applied loads remains constant and the seepage velocity continues to increase at a more gradual rate until it reaches a steady state of 1076.340 cm/s and 644.625 cm/s for each node respectively. Node 1978 experiences a larger fluid surface flux and thus has a higher seepage velocity than node 3864.

# Chapter 6

# Conclusions and future work

The following chapter draws conclusions on the use of the biphasic TPM sea ice models and discusses future work as well as aspects of the study that could be improved and developed in the future.

## 6.1 Pixel example conclusions and future work

Experimental verification of brine movement through ice segments would be needed to verify the accuracy of models making use of image analysis and processing to obtain inputs for a biphasic TPM computational models in order to model brine transport within Antarctic sea. The technique however seems feasible due to the observation of results obtained in the pixel example in section 5.1.

The technique could be applied to other imaging techniques such as MRI introduced in Figure 2.4. The same image processing methodology can be applied to MRI image slices to obtain liquid and solid volume fractions. MRI image segments will provide a more accurate estimate as to the exact location of brine inclusions. The individual slices could then be joined together by extrapolating values between slices to obtain the full three dimensional microstructure of a sea ice sample as an input for a computational model. This will result in more accurate results of brine transport through Antarctic sea ice however will be time consuming and have a high computational time due to the high resolution of MRI images. The determination of a permeability function linking volume fractions to permeability is essential for future work intended to use this image processing and imaging analysis to determine material input parameters for computational models.

## 6.2 Sea ice models conclusions and future work

The multidimensional nature of brine transport within Antarctic sea ice was successfully described using a biphasic TPM-based continuum mechanics framework. It is evident that brine movement within sea ice occurs in more than one direction however the most significant brine movement is observed in the vertical z direction as expected [22].

An investigation into the the brine transport mechanisms known to influence the transport of brine in sea ice was done and the developed biphasic TPM continuum framework was used to assess the brine removal mechanisms discussed in section 2.3. While conclusions could be

drawn regarding the general flow direction of brine within Antarctic sea ice flows as a result of gravity drainage and flushing, these methods of brine transport could not be accurately described due to the following:

- The current implementation of the biphasic TPM continuum framework in SESKA does not account for phase changes in a porous material thus not accounting for the density gradient that occurs with the surface cooling associated with gravity drainage discussed in subsection 2.3.3. This density gradient had to be accounted for through the addition of force applied to the top surface of the ice floe as a surface traction. Additionally, the effect of super-heating (discussed in subsection 2.3.3) that occurs during gravity drainage cannot be accounted for as simulating the melting of brine requires phase change. While the biphasic TPM model does not account for sea ice thermodynamics, it has the capability to be expanded and the convective process mentioned in subsection 2.3.3 can be resolved due to the models multidimensional nature.
- The simulations described in 5.2 describe a material with the same material parameters through the entire depth of the floe. This is however no the case for a true ice floe which is composed of different layers with different material parameters which can be seen in Figure 2.7.

The biphasic TPM framework is able to capture the flow direction of brine within the sea ice floe and from this one is able to comment on the multidimensional nature of brine movement. The capturing of the multidimensional liquid brine flow differs from models by Jeffery *et al.*, [25] and Notz *et al.*, [30] discussed in subsection 2.3.4 which describe the vertical movement of brine and do not capture the horizontal component of flushing desalination. One is also able to describe gravity and flushing drainage based of assumptions and compare brine movement in these brine removal mechanisms.

In order to draw further conclusions, the TPM model can be further developed to allow for air inclusions which will describe the true structure of sea ice more accurately as a triphasic TPM model. The geometry of the ice floe could be changed to an asymmetric shape which represents a more accurate sea ice floe geometry.

# Appendix A

# Ethics Approval

Application for Approval of Ethics in Research (EIR) Projects
Faculty of Engineering and the Built Environment, University of Cape Town

## APPLICATION FORM

**Please Note:**
Any person planning to undertake research in the Faculty of Engineering and the Built Environment (EBE) at the University of Cape Town is required to complete this form before collecting or analysing data. The objective of submitting this application *prior* to embarking on research is to ensure that the highest ethical standards in research, conducted under the auspices of the EBE Faculty, are met. Please ensure that you have read, and understood the **EBE Ethics in Research Handbook** (available from the UCT EBE, Research Ethics website) prior to completing this application form: http://www.ebe.uct.ac.za/ebe/research/ethics1

| APPLICANT'S DETAILS | | |
|---|---|---|
| Name of principal researcher, student or external applicant | | Andrea Cook |
| Department | | Civil Engineering |
| Preferred email address of applicant: | | cloxand008@myuct.ac.za |
| If Student | Your Degree: e.g., MSc, PhD, etc. | MSc Civil Engineering |
| | Credit Value of Research: e.g., 60/120/180/360 etc. | 120 |
| | Name of Supervisor (if supervised): | Sebastian Skatulla |
| If this is a researchcontract, indicate the source of funding/sponsorship | | Click here to enter text. |
| Project Title | | Modelling of Brine Transport Mechanisms in Antarctic Sea Ice |

**I hereby undertake to carry out my research in such a way that:**

- there is no apparent legal objection to the nature or the method of research; and
- the research will not compromise staff or students or the other responsibilities of the University;
- the stated objective will be achieved, and the findings will have a high degree of validity;
- limitations and alternative interpretations will be considered;
- the findings could be subject to peer review and publicly available; and
- I will comply with the conventions of copyright and avoid any practice that would constitute plagiarism.

| SIGNED BY | Full name | Signature | Date |
|---|---|---|---|
| Principal Researcher/ Student/External applicant | Andrea Cook | | 09 Apr 2019 |

| APPLICATION APPROVED BY | Full name | Signature | Date |
|---|---|---|---|
| **Supervisor** (where applicable) | Sebastian Skatulla | | 12.04.2019 |
| **HOD** (or delegated nominee) Final authority for all applicants who have answered NO to all questions in Section1; and for all Undergraduateresearch (including Honours). | Dyllon Randall | | 5.09.2019 |
| **Chair : Faculty EIR Committee** For applicants other than undergraduate students who have answered YES to any of the above questions. | | | |

Page 1 of 1

**Figure A.1.** 2019 ethics approval

# List of References


[1] Stephen F Ackley. The Growth, Structure, and Properties of Sea Ice. *The Geophysics of Sea Ice*, (January 1991), 2013.

[2] Kevin R. Arrigo and David N. Thomas. Large scale importance of sea ice biology in the Southern Ocean. *Antarctic Science*, 16(4):471–486, 2004.

[3] Klaus J Bathe. *Finite Element Procedures*. Prentice Hall, Pearson Education, Inc, Massachusetts Institute of Technology, United States, 2014.

[4] D. B. Clarke and S. F. Ackley. Sea ice structure and biological activity in the Antarctic marginal ice zone. *Journal of Geophysical Research*, 89(C2):2087–2095, 1984.

[5] G F N Cox and W F Weeks. Equations for determining the gas and brine volumes in sea-ice samples. *Journal of Glaciology*, 29:306–316, 1983.

[6] Wolfgang Ehlers and J Bluhm. *Porous Media*. 2002.

[7] H Eicken. Salinity profiles of antarctic sea ice: Field data and model results. *Journal of Geophysical Research*, 97:15545–15557, 10 1992.

[8] H. Eicken. Tracer studies of pathways and rates of meltwater transport through Arctic summer sea ice. *Journal of Geophysical Research*, 107(C10):1–20, 2002.

[9] H. Eicken, C. Bock, R. Wittig, H. Miller, and H. O. Poertner. Magnetic resonance imaging of sea-ice pore fluids: Methods and thermal evolution of pore microstructure. *Cold Regions Science and Technology*, 31(3):207–225, 2000.

[10] H. Eicken, D. M. Cole, and L. H. Shapiro. Porosity-Permeability-Salinity Relationships in First-Year Arctic Sea Ice. 2(1):2004, 2004.

[11] Hajo Eicken, Bodil Bluhm, Roy Collins, Rolf Gradinger, Christian Haas, Malcolm Ingham, Andrew Mahoney, Marcel Nicolaus, and D. Perovich. *Field techniques in sea-ice research*. 01 2014.

[12] D. L. Feltham, N. Untersteiner, J. S. Wettlaufer, and M. G. Worster. Sea ice is a mushy layer. *Geophysical Research Letters*, 33(14):4–7, 2006.

[13] R J Galley, B G T Else, N X Geilfus, A A Hare, D Isleifson, D G Barber, and S Rysgaard. Imaged brine inclusions in young sea ice-shape, distribution and formation timing. *Cold Regions Science and Technology*, 111:39–48, 2015.

[14] K. Golden, Stephen Ackley, and VI Lytle. The percolation phase transition in sea ice. *Science (New York, N.Y.)*, 282:2238–41, 01 1999.

[15] A. J. Gough, A. R. Mahoney, P. J. Langhorne, M. J.M. Williams, and T. G. Haskell. Sea ice salinity and structure: A winter time series of salinity and its distribution. *Journal of Geophysical Research: Oceans*, 117(3):1–12, 2012.

[16] Anthony J Gow, Stephen F Ackley, Kurt R Buck, and Kenneth M Golden. Physical and structural characteristics of weddell sea pack ice. *Cold Regions Science and Technology*, pages 1–71, 08 1987.

[17] Anthony J Gow and Walter B Tucker. Physical and Dynamic Properties of Sea Ice in the Polar Oceans. *Oceans*, 1991.

[18] Philipp J. Griewank and Dirk Notz. Insights into brine dynamics and sea ice desalination from a 1-D model study of gravity drainage. *Journal of Geophysical Research: Oceans*, 118(7):3370–3386, 2013.

[19] Philipp J Griewanl and Dirk Notz. Insights into brine dynamics and sea ice desalination from a 1-d model study of gravity drainage. *Journal of Geophysical Research*, 118:3370–3386, 2013.

[20] Christian Haas. *Dynamics versus Thermodynamics: The Sea Ice Thickness Distribution*, chapter 3, pages 82–111. John Wiley and Sons, Ltd, 2008.

[21] G Hopkins and S Skatulla. Growth, modelling and remodelling of cardiac tissue: A multiphase approach. 2017.

[22] E. C. Hunke, D. Notz, A. K. Turner, and M. Vancoppenolle. The multiphase physics of sea ice: A review for model developers. *Cryosphere*, 5(4):989–1009, 2011.

[23] Elizabeth C Hunke, William H Lipscomb, and Adrian K Turner. Sea-ice models for climate study: retrospective and new directions. *Journal of Glaciology*, 56(200):1162–1172, 2010.

[24] Lars Ingolf Eide and Seelye Martin. The Formation of Brine Drainage Features in Young Sea Ice. *Journal of Glaciology*, 14(70):137–154, 2017.

[25] N. Jeffery, E. C. Hunke, and S. M. Elliott. Modeling the transport of passive tracers in sea ice. *Journal of Geophysical Research: Oceans*, 116(7):1–15, 2011.

[26] K. A. Jones, M. Ingham, and H. Eicken. Modeling the anisotropic brine microstructure in first-year Arctic sea ice. *Journal of Geophysical Research: Oceans*, 117(2):1–14, 2012.

[27] Gary A. Maykut and Norbert Untersteiner. Some results from a time-dependent thermodynamic model of sea ice. *Journal of Geophysical Research*, 76(6):1550–1575, 2008.

[28] C. A. Middleton, C. Thomas, D. M. Escala, J. L. Tison, and A. De Wit. Imaging the Evolution of Brine Transport in Experimentally Grown Quasi-two-dimensional Sea Ice. *Procedia IUTAM*, 15:95–100, 2015.

[29] Dirk Notz and M. Grae Worster. A one-dimensional enthalpy model of sea ice. *Annals of Glaciology*, 44:123–128, 2006.

[30] Dirk Notz and M. Grae Worster. Desalination processes of sea ice revisited. *Journal of Geophysical Research: Oceans*, 114(5):1–10, 2009.

[31] Algot K. Peterson. Observations of brine plumes below melting Arctic sea ice. *Ocean Science*, 14(1):127–138, 2018.

[32] Chris Petrich and Hajo Eicken. Overview of sea ice growth and properties. *Sea Ice: Third Edition*, pages 1–41, 2016.

[33] Chris Petrich, Jonas Karlsson, and Hajo Eicken. Porosity of growing sea ice and potential for oil entrainment. *Cold Regions Science and Technology*, 87:27–32, 2013.

[34] T. Ricken. Skriptum zur Vorlesung Multiphase Materials. 2014.

[35] Tim Ricken, Uta Dahmen, and Olaf Dirsch. A biphasic model for sinusoidal liver perfusion remodeling after outflow obstruction. *Biomechanics and modeling in mechanobiology*, 9:435–50, 08 2010.

[36] Frank Smith, Alexander Korobkin, Emilian Parau, Daniel Feltham, and Vernon Squire. Modelling of sea-ice phenomena. *Philosophical transactions. Series A, Mathematical, physical, and engineering sciences*, 44:376(2129), 2018.

[37] P. D. Taylor and D. L. Feltham. A model of melt pond evolution on sea ice. *Journal of Geophysical Research C: Oceans*, 109(12):1–19, 2004.

[38] David N Thomas. *Sea Ice Third Edition*. 2017.

[39] G. W. Timco and W. F. Weeks. A review of the engineering properties of sea ice. *Cold Regions Science and Technology*, 60(2):107–129, 2010.

[40] N. Untersteiner. Natural Desalination and Equilibrium Salinity Profile of Old Sea lee. *Physics of Snow and Ice*, 73(4), 1967.

[41] Martin Vancoppenolle, Hugues Goosse, Anne De Montety, Thierry Fichefet, Bruno Tremblay, and Jean Louis Tison. Modeling brine and nutrient dynamics in Antarctic sea ice: The case of dissolved silica. *Journal of Geophysical Research: Oceans*, 115(2):1–18, 2010.

[42] A. J. Wells, J. S. Wettlaufer, and S. A. Orszag. Brine fluxes from growing sea ice. *Geophysical Research Letters*, 38(4), 2011.